


Fall 11-17-2018

Characterization of Nanomaterials for Thermal Management of Electronics

Amit Rai

Follow this and additional works at: <https://digitalcommons.latech.edu/dissertations>

 Part of the [Nanoscience and Nanotechnology Commons](#), and the [Other Materials Science and Engineering Commons](#)

Recommended Citation

Rai, Amit, "" (2018). *Dissertation*. 16.
<https://digitalcommons.latech.edu/dissertations/16>

This Dissertation is brought to you for free and open access by the Graduate School at Louisiana Tech Digital Commons. It has been accepted for inclusion in Doctoral Dissertations by an authorized administrator of Louisiana Tech Digital Commons. For more information, please contact digitalcommons@latech.edu.

**CHARACTERIZATION OF NANOMATERIALS FOR
THERMAL MANAGEMENT OF
ELECTRONICS**

by

Amit Rai, B.E., M.S.

A Dissertation Presented in Partial Fulfillment
of the Requirements of the Degree of
Doctor of Philosophy

COLLEGE OF ENGINEERING AND SCIENCE
LOUISIANA TECH UNIVERSITY

November 2018

ABSTRACT

Recently, there has been a growing interest in flexible electronic devices as they are light, highly flexible, robust, and use less expensive substrate materials. Such devices are affected by thermal management issues that can reduce the device's performance and reliability. Therefore, this work is focused on the study of the thermal properties of nanomaterials and the methods to address such issues. The goal is to enhance the effective thermal conductivity by adding nanomaterials to the polymer matrix or by structural modification of nanomaterials. The thermal conductivity of copper nanowire/polydimethylsiloxane and copper nanowire/polyurethane composites were measured and showed more than threefold enhancement compared to the thermal conductivity values of the neat polymers. Furthermore, identical heat sources were used on the neat polymer as well as the composite samples, and the resulting thermal images were taken, which showed that the resulting hot spot was significantly less severe for the composite sample, demonstrating the potential of copper nanowire/polymer composite as a substrate for flexible electronics with better heat spreading capability.

In addition, the thermal properties of cellulose nanocrystals-poly (vinyl alcohol) composite films with different structural configurations of cellulose nanocrystals (such as isotropic and anisotropic configurations) were investigated as an alternative to commonly used petroleum-based materials for potential application in the thermal management of flexible electronic devices. Also, the in-plane thermal conductivity of the anisotropic

composite film was as high as $\sim 3.45 \text{ W m}^{-1} \text{ K}^{-1}$ in the chain direction. Moreover, the composite films showed ~ 4 - 14 fold higher in-plane thermal conductivity than most polymeric materials used as substrates for flexible electronics. A high degree of cellulose nanocrystal orientation and the inclusion of poly (vinyl alcohol) were the reasons for such improvements. In addition, thermal images showed that the cellulose nanocrystals-poly (vinyl alcohol) composite films had better heat dissipation capability compared to the neat poly (vinyl alcohol) films, indicating its potential application for flexible electronic devices.

In another study, thermal properties of nanodiamond films obtained through a solution-based directed covalent assembly were studied as a low-cost and greener alternative to the nanodiamond films grown via chemical vapor deposition method for thermal management of electronics. The results obtained showed cross-plane thermal conductivity as high as $3.50 \pm 0.54 \text{ W m}^{-1} \text{ K}^{-1}$ for nanodiamond film of $139.1 \pm 19.5 \text{ nm}$ thick. Such a low cross-plane thermal conductivity value can be attributed to higher porosity and poor interface quality compared to that of the nanodiamond films grown via chemical vapor deposition method. Hence, there is still more room for improvement for such nanodiamond films.

The above chapters were focused on the study of the thermal properties of various types of nanomaterials for thermal management of electronic devices. In the next chapter, a technique for the fabrication of a device, that is capable of performing characterization nanomaterials was presented. In this work, suspended beam microdevices for electrothermal characterization of nanomaterials were fabricated through a standard photolithography technique that is less time-consuming, less expensive and much simpler

than the methods used by other research groups in the past. The agreement of the measured in-plane thermal conductivity of the suspended central silicon nitride bare bridge with the literature validated the microdevice, setup, and the experimental procedure. Furthermore, these microdevices can be used to measure other important thermoelectric properties of nanomaterials such as the Seebeck coefficient, electrical conductivity, and thermoelectric figure of merit.

APPROVAL FOR SCHOLARLY DISSEMINATION

The author grants to the Prescott Memorial Library of Louisiana Tech University the right to reproduce, by appropriate methods, upon request, any or all portions of this Dissertation. It is understood that “proper request” consists of the agreement, on the part of the requesting party, that said reproduction is for his personal use and that subsequent reproduction will not occur without written approval of the author of this Dissertation. Further, any portions of the Dissertation used in books, papers, and other works must be appropriately referenced to this Dissertation.

Finally, the author of this Dissertation reserves the right to publish freely, in the literature, at any time, any or all portions of this Dissertation.

Author _____

Date _____

DEDICATION

To my parents, Khim Bahadur Rai and Kamala Rai, supportive brother Anup Rai, dearest sister Anita Rai, and to my loving wife Dinu Rai, without whom this would not have been possible.

TABLE OF CONTENTS

ABSTRACT.....	iii
APPROVAL FOR SCHOLARLY DISSEMINATION	vi
DEDICATION	vii
LIST OF TABLES	xi
LIST OF FIGURES	xii
ACKNOWLEDGEMENTS.....	xvi
CHAPTER 1 INTRODUCTION	1
1.1 Background and Motivation	1
1.2 Dissertation Outline	8
CHAPTER 2 ENHANCED THERMAL CONDUCTION AND INFLUENCE OF INTERFACIAL RESISTANCE WITHIN FLEXIBLE HIGH ASPECT RATIO COPPER NANOWIRE/POLYMER COMPOSITES.....	10
2.1 Introduction and Motivation	10
2.2 Research Objectives.....	13
2.3 Experimental Materials and Methods	14
2.3.1 Cu NW Synthesis.....	14
2.3.2 Cu NW Characterization.....	16
2.3.3 Cu NW/polymer composite samples preparation	18
2.3.4 Experimental Setup.....	20
2.3.5 Measurement.....	22
2.4 Results and Discussion	27
2.5 Conclusion	34

CHAPTER 3 SUPERIOR, PROCESSING-DEPENDENT THERMAL CONDUCTIVITY OF CELLULOSE NANOCRYSTAL-POLY (VINYL ALCOHOL) COMPOSITE FILMS	36
3.1 Introduction and Motivation	36
3.2 Research Objectives.....	43
3.3 Experimental Materials and Methods	44
3.3.1 Sample Preparation	44
3.3.2 Experimental Setup and Measurement	44
3.4 Results and Discussion	47
3.4.1 Effect of (CNC: PVA) composition with isotropic configuration:	47
3.4.2 Effect of anisotropy for different CNC: PVA composition:	51
3.4.3 Effective Medium Theory – Choy & Young (EMT-CY) Model applied to CNC-PVA composite thin films:	54
3.5 Conclusion	60
CHAPTER 4 THERMAL CHARACTERIZATION OF ULTRANANOCRYSTALLINE NANODIAMOND FILMS	61
4.1 Introduction and Motivation	61
4.2 Research Objectives.....	67
4.3 Experimental Materials and Methods	67
4.3.1 ND film Samples.....	67
4.3.2 3ω Method	68
4.3.3 Microdevice Fabrication	74
4.3.4 Experimental Setup.....	76
4.3.5 Measurement.....	77
4.4 Results and Discussion	80
4.5 Conclusion	85

CHAPTER 5 SUSPENDED BEAM MICRODEVICE FABRICATION THROUGH STANDARD PHOTOLITHOGRAPHY FOR THERMOELECTRIC CHARACTERIZATION OF NANOMATERIALS.....	86
5.1 Introduction and Motivation	86
5.2 Research Objectives.....	90
5.3 Experimental Materials and Methods	91
5.3.1 Microdevice Design and Fabrication	91
5.3.2 Experimental Setup.....	95
5.3.3 Measurement.....	96
5.4 Results and Discussion	103
5.5 Conclusion	104
CHAPTER 6 CONCLUSIONS AND FUTURE WORK.....	106
6.1 Conclusions.....	106
6.2 Future Work	108
APPENDIX A UNCERTAINTY ANALYSIS	110
Bibliography	112

LIST OF TABLES

Table 3-1: Thermal conductivity for different polymer/polymer nanocomposite systems.....	54
---	----

LIST OF FIGURES

<p>Figure 1-1: A brief timeline of the development of flexible electronics based on organic semiconductor materials and stretchable and flexible inorganic devices (CMOS: Complementary metal-oxide-semiconductor). Original data from Cai <i>et al.</i> [10].</p>	3
<p>Figure 2-1: The precursor solution a) before and b) after heating on a hot plate at 50 °C with magnetic stirring for 12 hours. The final Cu NW product after freeze-drying is shown in c) with a millimeter scale for reference. Reproduced with permission from Ref. [72].</p>	16
<p>Figure 2-2: FE-SEM images of the obtained Cu NWs within the polymer matrix. Reproduced with permission from Ref. [72].</p>	17
<p>Figure 2-3: EDS analysis of the Cu NW material supported on a Si chip and carbon tape. Reproduced with permission from Ref. [72].</p>	18
<p>Figure 2-4: a) Cu NW/PDMS sample at 1.5 vol.% loading. b) Cu NW/PU composite sample at 2.7 vol.% loading. c) Bending of a flexible Cu NW/PDMS composite sample. Reproduced with permission from Ref. [72].</p>	19
<p>Figure 2-5: a) Annotated illustration of the steady-state thermal conductivity measurement setup in a symmetric configuration. Not to scale. b) Photograph of the actual assembled setup with topmost layers of insulation removed for visualization. The heat exchangers used in conjunction with the liquid cooled heat sinks are external to the enclosure on the left and right (not shown). Not to scale. Reproduced with permission from Ref. [72].</p>	21
<p>Figure 2-6: Representative heat flow vs temperature gradient data obtained at varying DC heating levels as described in the text, with the resulting slopes being used for calculating κ of the samples. a) Neat PDMS data taken in a symmetric configuration. b) As synthesized 4.1 vol. % Cu NW/PDMS composite sample data along with the values measured simultaneously for its associated neat PDMS reference sample in an asymmetric configuration. Error bars are included but are obscured by the data point symbols. The errors were +/- 2 mW for Q and +/- 510 K/m for dT/dx. Reproduced with permission from Ref. [72].</p>	23

- Figure 2-7:** Plot of thermal conductivity of the Cu NW/PDMS composite and Cu NW/PU composite as a function of the volume fraction of Cu NWs. Reproduced with permission from Ref. [72]. 28
- Figure 2-8:** Thermal conductivity enhancement for the Cu NW/PDMS composite and Cu NW/PU composite as a function of the volume percent loading of Cu NWs relative to their respective neat polymers. Also plotted are reported thermal conductivity enhancement values for composites filled with carbon nanotubes [103], graphene [104], gold nanorods [38] and silver NWs [66]. Reproduced with permission from Ref. [72]. 29
- Figure 2-9:** Thermal conductivity values of CuNW/PDMS and CuNW/PU composite samples plotted along with the theoretical values of R_k and thermal conductivity values predicted by the model developed in different literature a) Xue Model b) Nan Model. Reproduced with permission from Ref. [72]. 31
- Figure 2-10:** a) A neat PU sample with shadow-evaporated Au serpentine heater and its associated temperature map at steady-state after applying a fixed Joule heating power. b) The annealed Cu NW/PU sample with 4.1% volume loading and its associated steady-state temperature map after applying the same Joule heating power as was used for the neat PU sample. Reproduced with permission from Ref. [72]. 34
- Figure 3-1:** Annotated 3D drawing of the measurement stage. Silver paint for affixing the sample not shown. 45
- Figure 3-2:** Thermal conductivity of un-sheared CNC: PVA films versus CNC content of the final film. Data shown is for 1, 5, and 10.7 initial CNC and PVA weight percent used during fabrication. The PVA molecular weight was 124-186 k. 48
- Figure 3-3:** Thermal conductivity of un-sheared CNC: PVA films versus CNC content of the final film. Data showed is for 1, 5, and 10.7 initial CNC and PVA weight percent used during fabrication. The PVA molecular weight was 89-98 k. 49
- Figure 3-4:** Effect of PVA for reducing the interfacial resistance between CNC domains. Here, point A is showed for the interfacial contact position where phonon can diffuse from one crystal to another crystal. (red arrow sign is denoted for the sum of every phonon vector projection in the chain direction of the individual crystalline domain)..... 51
- Figure 3-5:** Measured $\kappa_{in-plane}$ in the direction of shear of CNC-PVA composites with various degrees of orientation. S is Hermann's order parameter for CNC-PVA composite system. 52
- Figure 3-6:** Effect of PVA for reducing the interfacial resistance between CNCs for anisotropic composites. Here, point A is shown for the interfacial contact position where phonons can diffuse from one crystal to another crystal. (red arrow sign is

denoted for the sum of every phonon vector projection in the chain direction of the individual crystalline domain).	53
Figure 3-7: Experimental κ of anisotropic CNC-PVA composite films shown along with results from the EMT-CY model as a function of S . The weight % of CNC is not in particular order. The stars represent the extrapolated values of κ obtained from the EMT-CY model at $S \approx 1$	57
Figure 3-8: Thermal images of CNC-PVA composites a) 100% PVA sample with low κ , and b) 90:10 CNC: PVA sample with high κ during Joule heating of a serpentine metallic heater simulating flexible electronics elements. c) Line scans along the centerline of a) and b) quantify the temperature reduction associated with the high κ sample at the same Joule heating power (175 mW). Inset: Photograph of 90:10 CNC: PVA sample with a shadow-evaporated metallic heater.	59
Figure 4-1: Schematic diagram of a bulk sample with a 3ω metal line patterned on the top of it. Adapted from Ref. [214]. Not to scale.	69
Figure 4-2: Schematic diagram of a thin film sample on the top of a substrate with a 3ω metal line patterned on the top of it. Adapted from the Ref. [214]. Not to scale.	72
Figure 4-3: a) Light microscope image of a single microdevice showing the Au lines used for the measurement of $\kappa_{cross-plane}$ along with the lines used for the measurement of $\kappa_{in-plane}$ outlined in blue b) Details of the blue boxed region showing all the GRT lines. The Au lines were deposited on the top of ND films. Large square features around the periphery are the contact pads that were used for forming electrical connections to the Au lines and the legs of the chip carrier.	75
Figure 4-4: a) A microdevice inserted in a commercially available 16-pin ceramic chip carrier package. b) Packaged microdevice loaded into the cryostat.	76
Figure 4-5: Image of the 3ω experimental setup.	77
Figure 4-6: Schematic diagram of the experimental setup used for the 3ω method. Adapted from Ref. [214].	78
Figure 4-7: Measured 3ω voltage as a function of frequency for the 20 cycles UNCD sample at 350 K.	80
Figure 4-8: Measured $\kappa_{cross-plane}$ of a) Si compared with the data from [221]. b) SiO_2 compared with the data from [219].	81
Figure 4-9: Measured $\kappa_{cross-plane}$ of the UNCD samples as a function of temperature.	82
Figure 4-10: Measured thermal resistance as a function of temperature.	84

- Figure 5-1:** Illustration of a suspended beam microdevice. A single device showing the contact pads along with the suspended SiN_x beams (top). Detail of the suspended SiN_x beams showing all the Pt lines and the central bridge(bottom). Not to scale..... 92
- Figure 5-2:** A combined photomask design created via LayoutEditor showing a single microdevice with a centralized region outlined in blue (left). Detail of the blue boxed region showing all the metal lines on the suspended beam (right). Not to scale. .. 93
- Figure 5-3:** Light microscope images with the undercuts obtained by using LOR 5B. .. 94
- Figure 5-4:** Light microscope images of a) a microdevice with central nitride beam being suspended after treatment with TMAH solution as indicated by the pink colored region. b) Details of the red boxed region showing the suspended beam along with the Pt lines..... 95
- Figure 5-5:** Measured electrical resistance increase of the PRT1 and PRT2 as a function of the heating current (I_{DC}) when $T_{stage} = 360$ K. 98
- Figure 5-6:** Measured four-probe electrical resistance values for PRT1 and PRT2 at various temperatures. The lines are the linear fits to the corresponding measurement data whose slopes give dR/dT values..... 99
- Figure 5-7:** ANSYS finite element analysis of the suspended beams with the temperature contours..... 101
- Figure 5-8:** Measured total power Q_{total} plotted as a function of $(\Delta T_h + \Delta T_s)$ 101
- Figure 5-9:** Measured ΔT_s plotted as a function of $(\Delta T_h - \Delta T_s)$ 102
- Figure 5-10:** Measured κ of a 500 nm thick SiN_x suspended bridge for a range of temperatures along with the values mentioned in the literature [245]..... 104

ACKNOWLEDGEMENTS

I would like to thank my advisor, Dr. Arden L. Moore for his inspiration, support, and encouragement throughout my PhD period. It would not have been possible without his help and mentorship. I would also like to thank many collaborators from other research groups who have helped make this work possible, especially Naim Patoary and Dr. Adarsh Radadia from Louisiana Tech University as well as Reaz A. Chowdhury and Dr. Jeffrey P. Youngblood from Purdue University. I also want to thank Dr. Niel Crews, Dr. Adarsh Radadia, Dr. Leland Weiss, and Dr. Sandra Zivanovic for serving on my advisory committee.

I would like to thank my lab mates, especially Pratik KC, Abdullah Nammari, Nishan Khatri, Caroline Bell, Patrick Morgan, Evan Glynn, and others from Dr. Moore's lab for providing such a friendly and working environment.

I would like to express my thanks to Dr. Alfred Gunasekaran, Ms. Debbie Wood, Mr. Davis Bailey, Mr. Phillip Chapman, and other IfM staff members for providing training with various instruments, and for helping with various measurements.

I also wish to thank Louisiana Tech University, Louisiana Board of Regents, and National Science Foundation for their funding support.

Finally, I would like to express my deepest gratitude to my parents for their selfless love and support. Endless thanks to my wife, Dinu, for her love, support, and encouragement to make this journey possible.

CHAPTER 1

INTRODUCTION

1.1 Background and Motivation

Historically, the vast majority of electronic components have been fabricated on rigid substrates such as glass or silicon (Si); hence, they can be rigid and brittle. The fabrication of Si requires significant energy, high processing temperatures (order of ~ 1000 °C), and hazardous chemicals [1]. In addition, traditional electronics need many fabrication steps, thereby increasing complexity and cost. Recently, there has been an increase in interest towards flexible electronics, especially to fulfill the needs for the applications that need more flexibility and stretchability. Flexible electronics refer to the technology that incorporates electronic devices on flexible substrates. Compared to traditional electronics, flexible electronics are light and highly flexible, robust (not brittle), use less expensive substrate materials, and can incur low manufacturing costs with industrial-scale production capabilities (ink-jet printing, roll-to-roll processing) [2]. Due to their unique and outstanding performances, more attention has been growing in both industry as well as academia where research works have been focused on flexible solar cells, light-emitting diodes (LEDs), sensors, electronic paper [3], [4], displays [5], [6], wearable electronics [7], [8], energy harvesting, and electronic skins [9].

Figure 1-1 shows a brief timeline of the development of flexible electronics based on organic semiconductor materials and stretchable and flexible inorganic devices. There have been efforts to replace Si with organic semiconductors for flexible electronics since they are compatible with flexible substrates and conducting polymers [10]. The organic semiconductor material [11], organic field effect transistor (OFET) [12], and organic LED(OLED) [13] were first presented in 1977, 1986, and 1987, respectively. Furthermore, p-type and n-type conducting organic materials [14], [15] were synthesized for use in large-scale integrated circuits (ICs). With the rapid increase in the development of organic semiconductors, more studies have been carried out for developing integrated systems consisting of OFETs [16]–[19] in the last few years. Flexible electronics were also developed by using inorganic electronic components which was first reported by Rogers *et al.* in 2006 [20]. Recently, more interest has also been growing towards flexible inorganic electronics due to better structural configuration designs [21]–[25] and transfer printing strategies [26]–[32] leading to the development of large-scale processing.

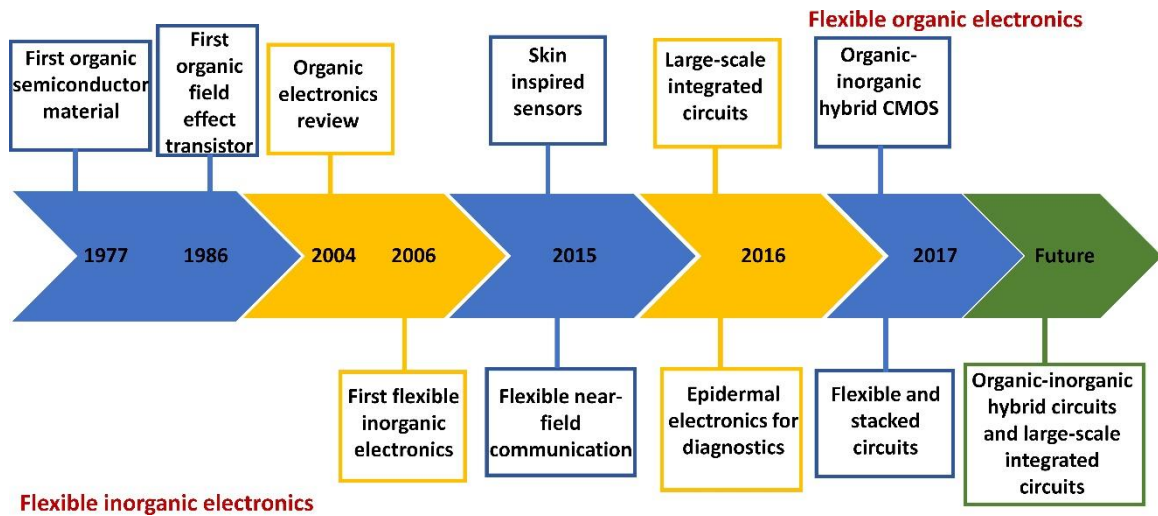


Figure 1-1: A brief timeline of the development of flexible electronics based on organic semiconductor materials and stretchable and flexible inorganic devices (CMOS: Complementary metal-oxide-semiconductor). Original data from Cai *et al.* [10].

Flexible electronics consist of active elements and substrates. Many studies are focused only on active elements that are based on nanomaterials such as nanotubes, 2D materials, and nanowires (NWs). Much less attention has been paid to developing advanced substrate materials with enhanced thermal conductivity (κ) for flexible electronics. Thus, there is still room for improvement [33]. The miniaturization of the components of electronic devices and an increase in their density has greatly enhanced the processing capability but at the cost of a high thermal load [34]–[36]. Even though such devices generate less heat individually compared to the traditional electronic devices, thermal management issues are still of great concern due to their large numbers and density [37].

Therefore, there is great need to resolve such thermal management issues in order to ensure the reliability and performance of the electronic devices [38]. Common materials used as substrates for flexible electronics include polyethylene terephthalate (PET), polyimide (PI). However, they have low κ [39], [40], high thermal expansion, and low

glass transition temperature [37]. The thermal management techniques that have been used for traditional electronics such as heat sinks, and heat pipes would not be suitable for flexible electronics. The complexity, as well as the power consumption of such devices, will further increase [41], [42], so there is need to understand the thermal transport of substrate materials to maintain the device's operation and reliability [37].

Materials that are light in weight with superior κ and processability are needed for miniaturized electronic devices for transferring the heat generated from various components. Polymer nanocomposites fulfill such requirements, hence, there has been a growing interest in the application of nanomaterial-laden polymer nanocomposites as substrates for thermal management of flexible electronics. In this case, the effective thermal energy is transported across the interface or away from the heat source by increasing the thermal conduction properties of the polymer [43]. Neat polymers have very low κ of $\sim 0.15\text{-}0.3 \text{ W m}^{-1} \text{ K}^{-1}$ [38], [44]–[46] at ambient conditions compared to traditional semiconductor substrates such as Si with $\kappa \sim 140 \text{ W m}^{-1} \text{ K}^{-1}$ [47], [48]. Use of polymer substrates with such low κ can impact the device's performance due to overheating. This has motivated researchers to use polymer-based nanocomposites as an alternative to flexible electronic substrates. Thermally conductive nanomaterials can be used as fillers with polymers to improve the effective κ of resulting nanocomposites. High aspect ratio (AR) filler materials would be suitable for this purpose to achieve a high enhancement in κ while maintaining the flexibility. Carbon nanotubes (CNTs) and graphene can be promising materials, but large tube-tube resistances and radiation losses [49] have limited their use as substrates for flexible electronics. Another option would be metallic NWs with high ARs since they have low percolation threshold, and enhancement in κ can be easily

achieved. Therefore, there is the need for further investigation to study the ability of the metallic NWs as fillers for improving the effective κ within the polymer matrix for flexible electronics.

Commonly flexible electronics use petroleum-based substrates (such as PET, PI) that are non-renewable, non-biodegradable, and sometimes toxic (for example, gallium arsenide (GaAs)) materials [50]. Such electronic devices are commonly upgraded frequently, or if discarded they cause serious environmental issues. Therefore, there is the need for substrate materials made of renewable and biodegradable materials [51]. Research works focusing on the use of biodegradable materials such as paper, silk, and synthetic polymers as substrates have been reported. These materials are flexible as well as degradable, but their performance does not meet the requirements of state-of-art electronics [50], [52], [53]. Cellulose-based materials such as cellulose nanofibrils (CNFs) and cellulose nanocrystals (CNCs) derived from woods [54], [55] are suitable candidates for eco-friendly flexible electronic substrates as they are biodegradable, highly transparent, flexible, and have desirable electrical properties [56]–[58]. Polymers such as Poly (vinyl alcohol) (PVA) can be added to CNCs in order to improve the properties (thermal, electrical, mechanical, optical) of the resulting polymer nanocomposites [59]–[61]. Further study is needed for modifying the structural configurations of crystalline domains of CNCs for enhancing the κ to resolve the thermal management issues of flexible electronic devices as greener and low-cost alternative to Si-based materials.

Thermal management is an issue for microelectromechanical system (MEMS)/electronic devices as well. Therefore, a portion of this work is focused on the study of the solution-based covalently assembled nanodiamond (ND) films for potential

use in the thermal management of MEMS/electronic devices. The need for faster and cheaper computing capabilities has motivated the researchers towards miniaturization of devices. It is evidenced by the reduction in the characteristic dimensions of electronic devices from microscale to nanoscale in only two decades. The critical dimensions of many electronic devices are on the orders of just tens of nanometers [36], [62]. Furthermore, the increase in the number of interconnects and decrease in transistor feature size results in the increase in thermal resistance of the ICs and difficulties in heat removal [63]. In modern chip architecture, the power dissipation is highly non-uniform, and hence, the power dense regions called 'hot spots' are formed with local temperatures significantly higher than the average die temperature [64] [65]–[67]. As a result, hot spots can help in determining the solutions for thermal management issues including the type of materials, heat sink, and heat spreader.

However, lack of a proper cooling system to take the heat away from the electronic devices can cause the degradation of performance to reduce the power. Therefore, there is a need for efficient heat spreading materials in the electronic devices to control the increasing power density and minimize the negative impacts of hotspots [43]. For this purpose, it is essential to investigate the thermal properties of the materials at the nanoscale for applications as heat spreaders in the MEMS/electronic devices. One better solution is to incorporate materials with high κ to take the undesired heat away from sensitive devices since κ of a heat spreader material indicates the ease of thermal transport. Most research works have been focused on the use of CVD-grown diamond thin films as heat spreaders. However, these films have issues of higher cost and integration on the substrates of interest. Therefore, there is need of diamond films that can be used as an alternative to the CVD-

grown diamond films. Thermal properties of the ND films obtained through a solution-based directed covalent assembly is studied in this work. The results from the study may create opportunities for a new class of low-cost diamond films that are compatible with a wide variety of substrates commonly used for electronics, optics, biosensors, and MEMS applications including Si, flexible polyimide, polyether ether ketone (PEEK), and transparent conductive polyester film where application of CVD diamond films have been limited.

Several nanoscale thermal transport measurement methods have been developed to study the size-dependent thermal and thermoelectric properties in nanomaterials. Such measurements include issues as large uncertainties are introduced in the κ measurements due to a radiation loss, heat loss to the thermometers, and the contact thermal resistances [68]; hence, careful design, fabrication, and analysis are needed. Different types of microfabricated devices have been used depending on the nature of the samples (nanotubes, NWs). Tighe *et al.* [69] used a microfabricated device for the measurement of thermal conductance (G) patterned, suspended GaAs nanobeams. The fabrication of such devices included multiple electron beam lithography (EBL) steps. Similarly, Shi *et al.* [70] fabricated suspended microdevices with two adjacent symmetric silicon nitride (SiN_x) membranes, each supported by five SiN_x beams for studying the thermoelectric properties of single-walled CNT bundles bridging the two membranes. A platinum resistance thermometer (PRT) coil was patterned on each membrane using EBL. Kim *et al.* [71] also used a similar microfabricated suspended device to perform thermal transport measurements of individual multi-walled CNTs in the temperature. The mentioned microfabricated devices have been successfully used for different studies, but the

fabrication steps involve steps such as EBL, LPCVD that are time complicated and time-consuming. To study the essential thermoelectric properties of nanomaterials, there is a need for similar microdevice fabrication technique that is simple and less time-consuming.

1.2 Dissertation Outline

This dissertation is divided into six chapters. In Chapter 2, high AR Copper (Cu) NWs (Cu NWs)/polymer composites are investigated for potential application in the thermal management of flexible electronic devices. First, the synthesis of high AR Cu NWs through a simple solution-based method is described. Then, the morphology of the Cu NWs is examined via field-emission scanning electron microscopy (FE-SEM) and the chemical composition is confirmed by electron dispersive spectroscopy (EDS). Preparation and measurements of the κ of Cu NW/polymer composites are also explained. Furthermore, the results obtained from the experiments are combined with the modeling results to study the effect of hydrogen annealing on the κ of Cu NW/polymer composites and ITR.

Chapter 3 presents the study of the thermal properties of the CNC-PVA composite films for potential application in the thermal management of flexible electronics as an eco-friendly alternative to the plastic-based substrate materials. The samples of CNC-PVA composite thin films with isotropic and anisotropic configurations are studied. Measurement of the in-plane κ ($\kappa_{in-plane}$) of CNC-PVA composite thin films is discussed. The results are analyzed and compared with that of the commonly used materials as substrates for flexible electronic devices. Furthermore, the application of the CNC-PVA composite thin film as a substrate for a flexible electronic device is demonstrated.

Chapter 4 describes the thermal characterization of ND films synthesized through the directed covalent assembly approach for potential thermal management applications in

MEMS/electronic devices. Microfabricated devices are used to perform the cross-plane κ ($\kappa_{cross-plane}$) measurement of ND films of different thicknesses via the 3ω method for temperatures between 125 K and 425 K. Furthermore, the results are presented to study the dependence of the thermal properties on the film thickness and ambient temperature.

In Chapter 5, details of the fabrication and testing of a suspended beam microdevice as an alternative to existing designs that use complex and time-consuming fabrication steps. The capability of the device to measure $\kappa_{in-plane}$ of a thin film material is demonstrated through a steady-state DC Joule heating approach for a temperature range of 85 K- 460 K.

Finally, Chapter 6 provides the major findings of this work as well as future recommendations.

CHAPTER 2

ENHANCED THERMAL CONDUCTION AND INFLUENCE OF INTERFACIAL RESISTANCE WITHIN FLEXIBLE HIGH ASPECT RATIO COPPER NANOWIRE/POLYMER COMPOSITES

2.1 Introduction and Motivation

This work has already been published [72]. Different types of materials are available for engineering applications. However, polymeric materials are considered to be better in terms of weight, cost, and ease of manufacturing compared to metal and ceramics. The performance of the polymers can be improved by modifying their physical properties. Different kinds of nanomaterials can be used as fillers within the polymers in order to make composites that have better physical properties (enhanced strength, better electrical or thermal conductivity) compared to the neat polymers. Therefore, polymers can also be used for applications other than their traditional uses and this has led to increased research in the field of polymer nanocomposites.

As mentioned in the introduction, thermal management of electronics is a pressing technological challenge. One means of addressing these challenges has been through polymeric composites. Polymeric composites have been commonly used as thermal interface materials (TIMs) by the electronics industry, but there can be a bottleneck on the overall thermal management of certain electronics packages due to the presence of interfacial thermal resistances. Hence, there is still more researches conducted for advanced TIMs materials based on nanomaterials [33]. Another application area of the thermally

conductive polymer nanocomposites is flexible electronics. Common materials used as substrates for flexible electronics include PET, polyimide (PI), polydimethylsiloxane (PDMS) and polyurethane (PU). The substrates of flexible electronics should be chemically stable, mechanically strong and easy to fabricate (devices can be printed directly in large amount through a roll-to-roll printing method). The above-mentioned materials meet those criteria but their neat forms have low κ of $\sim 0.15\text{-}0.3 \text{ W m}^{-1} \text{ K}^{-1}$ [38], [44]–[46] at ambient conditions compared to traditional semiconductor substrates such as Si with $\kappa \sim 140 \text{ W m}^{-1} \text{ K}^{-1}$ [47], [48]. The polymer substrate with low κ can be detrimental to the device, and it can even damage the device due to overheating [73]. Such issues have motivated researchers towards polymer matrix nanocomposites as an alternative for flexible electronic substrates since they have better κ and hence excellent thermal management capabilities.

As mentioned above, different types of candidate nanomaterials are available for enhancement of κ . Traditional fillers such as alumina and zinc oxide need higher volume fraction of about 10-15 vol. % in order to achieve the desired enhancement of κ [74]. They have spherical geometries; therefore, they need higher loading to achieve the percolation threshold and also suffer from multiple thermal resistances at interparticle boundaries [75]. Adding such a large amount of filler to the polymer can make the resulting composite more rigid [76]. Therefore, fillers that can achieve the percolation threshold at the lowest possible filler loadings are desirable so that the polymer composite can still be flexible while proving very high enhancement of κ . Filler materials with high AR are suitable for this purpose. Carbon nanotubes (CNTs) and graphene are promising materials to achieve such thermal performance and hence they have been widely studied as filler materials on the

basis of their higher intrinsic κ [77].

However, the higher thermal conductivities have been not been realized for nanotube assemblies because of the resistances at tube-tube interconnections and very high radiative thermal losses [78]. However, high aspect ratio metallic NWs are considered to be most promising because of their lower percolation threshold compared to spherical, plate, or rod-like fillers [73]. Although there are varieties of metallic NWs, much research has been focused on the high AR NWs of gold (Au) or silver (Ag) for use in flexible conductive electrodes due to their outstanding conduction properties and ability to resist surface oxidation. Regarding thermal transport, Balachander *et al.* [38] prepared Au NWs using a solution-based method with NWs having 4-7 nm diameters and lengths on the order of 1 micron for an AR range of ~150-250. They introduced those NWs to PDMS for developing nanocomposites. At low volume fraction of Au NWs (slightly more than 3 vol. % of Au NWs), the resulting composite had κ of $5 \text{ W m}^{-1} \text{ K}^{-1}$ that is a factor of 30 improvements in κ over the neat PDMS. Furthermore, this result was also a factor of four higher than the κ obtained at 4 vol. % of Au NWs with diameter ~20 nm and lower AR of only ~2.5. The authors concluded that the smaller NW diameters and higher AR were the factors responsible for higher κ . The higher ARs of the Au NWs actually enable more inter-nanowire contacts within the composite, thus forming low resistance pathways for transport than the one in which individual NWs are scattered and isolated within the matrix and the interface thermal resistance can dominate. However, the cost can be a limiting factor for the polymer composites based on Au NWs or Ag NWs outside of the lab environments. Alternatively, copper (Cu) is cheaper, abundant in nature, and has conductivity comparable to Au and Ag; hence, many studies have been focused on the high

AR copper (Cu) NW-based composites for conductive electrodes [79]–[86] and TIMs applications [77], [87]. Wang *et al.* [77] used single-crystalline Cu NWs with high (AR ~100-1000) and polyacrylate to create composites for TIMs application and measured the κ of the composites by the laser flash method. They reported their best sample as having κ of $2.46 \text{ W m}^{-1} \text{ K}^{-1}$ at very ultra-low volume fraction (~0.9% of Cu NWs) which was a ~1350 % enhancement over the plain matrix and also higher than that of the composites filled with commercial Ag NWs at 1.1 vol. %. The κ of the Cu NW-polyacrylate composites increased rapidly at just ~0.9% of Cu NWs which was said to be indicative of having achieved a percolation threshold. The results mentioned above appear very promising, but more research is still required to study the ability of the high AR Cu NWs as filler material for improving the effective κ within polymer matrix including their application for flexible electronics and TIMs. In addition, more investigation is also needed to figure out the factors that are limiting further enhancement of κ in such materials.

2.2 Research Objectives

In this work, we investigated the use of high AR Cu NWs prepared by a solution-based method, as κ -enhancing fillers for flexible polymer composites. To accomplish this goal, the following specific objectives were to be achieved through this research:

- Synthesis of high AR Cu NWs using a simple solution-based method.
- Examine the morphological and chemical characteristics of the high AR Cu NWs.
- Use those high AR Cu NWs to create Cu NW/PDMS and Cu NW/PU flexible composites at various loading levels.
- Determine the κ of the Cu NW/PDMS and Cu NW/PU flexible composites using a steady-state measurement technique.

- Investigate the effects of hydrogen annealing on composite κ and interfacial thermal resistance R_k .

The high AR Cu NWs were synthesized in large quantity using a simple solution-based method. Field-emission scanning electron microscopy (FE-SEM) was used to examine the morphology of the Cu NWs. Also, the chemical composition was examined by electron dispersive spectroscopy (EDS). Multiple Cu NW/PDMS and Cu NW/PU flexible composite samples were prepared with varying Cu NW volume fraction (f) from 0.1% to 4.1% and the κ of each sample were measured using steady-state measurement technique. A combination of experimentation and modeling was used to study the effects of hydrogen annealing on the κ of the composites and interfacial thermal resistance which is explained in detail in later sections.

2.3 Experimental Materials and Methods

2.3.1 Cu NW Synthesis

Glucose, copper chloride dihydrate ($\text{CuCl}_2 \cdot 2\text{H}_2\text{O}$), oleic acid (OA, technical grade, 90%), and oleylamine (OM, technical grade, 70%) were purchased from Sigma-Aldrich. Ethanol was obtained from Fischer Scientific and PDMS along with the cross-linker (Sylgard 184) were purchased from Dow Corning. To prepare polyurethane (PU) composites, Clear Flex® 95 was purchased from Smooth-On USA LLC. The method described by Li *et al.* [88] was modified and used for the synthesis of Cu NWs. First, 6.8 g of $\text{CuCl}_2 \cdot 2\text{H}_2\text{O}$ and 7.92 g of glucose were added to 800 mL of deionized (DI) water under magnetic stirring. In a separate beaker, 0.8 mL of OA and 90 mL OM were added to 140 mL of ethanol under magnetic stirring. OA and OM play the role of dual capping agents and glucose acts as a reducing reagent. After mixing these two solutions in a 5 L

glass jar, the resulting solution was diluted up to 4 L by adding DI water and finally left for 12 hours on a hot plate at 50 °C under magnetic stirring. As shown in **Figure 2-1**, the color of the final solution changed from blue to caesious after heating/stirring. Subsequently, the solution was transferred to a commercial electric pressure cooker and held at a gauge pressure of 80 kPa and a temperature of 118 °C for 10 hours. As a result of the reaction inside the electric pressure cooker, reddish brown Cu NW solution was obtained. From this solution, a small amount (20 mL) was centrifuged for 4 min at 5000 rpm to separate solid Cu NWs from the bulk solution. Then the solid Cu NWs were centrifuged twice in DI water to remove excess chemicals that might be present in the solution.

After this cleansing process, DI water was added to the Cu NWs and the solution was left in a freezer at -79 °C for approximately 12 hours or until completely frozen, followed by vacuum drying for 24 hours to remove DI water and isolate Cu NWs. **Figure 2-1(c)** shows the final product of this process. The use of freeze-drying to isolate the Cu NW mass and the resulting product are similar to those reported in previous works on Cu NW aerogel monoliths [89], [90]. The Cu NWs obtained by this method can be easily mixed with different types of polymers without an intermediary solution phase which could alter the chemistry of the polymer itself. In terms of yield, 150 mL of crude Cu NW solution provided approximately 300 milligrams of isolated Cu NWs.

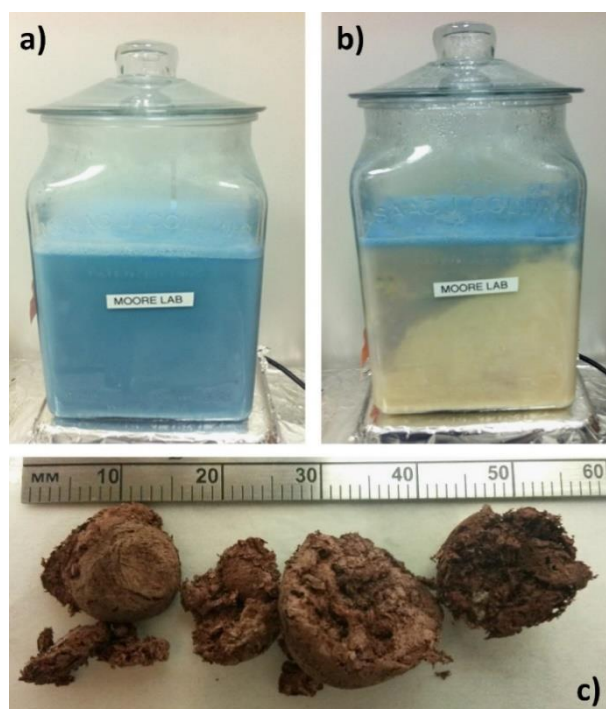


Figure 2-1: The precursor solution a) before and b) after heating on a hot plate at 50 °C with magnetic stirring for 12 hours. The final Cu NW product after freeze-drying is shown in c) with a millimeter scale for reference. Reproduced with permission from Ref. [72].

2.3.2 Cu NW Characterization

The morphologies of the Cu NWs were characterized by field-emission scanning electron microscopy (FE-SEM, Hitachi S-4800). **Figure 2-2** shows the FE-SEM images of Cu NWs within a polymer matrix at different magnifications. This measurement showed an average length of the Cu NWs to be 20 μm with an average diameter of 55 nm, resulting in AR of ~ 364 .

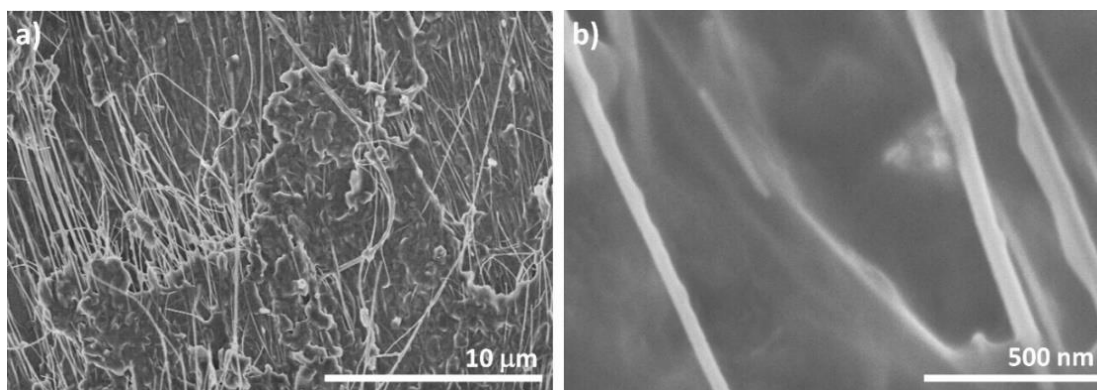


Figure 2-2: FE-SEM images of the obtained Cu NWs within the polymer matrix. Reproduced with permission from Ref. [72].

The solid obtained after freeze-drying was spread onto a Si chip to determine the chemical composition by using Electron dispersive spectroscopy (EDS, Ametek EDAX). The result is shown in **Figure 2-3**. The EDS analysis shows the sample consists of a good amount of Cu, with a very small amount of Cl that was introduced from CuCl_2 during the synthesis process. In addition, Si and carbon can also be observed, which is due to the Si substrate and carbon tape used for supporting and mounting the sample.

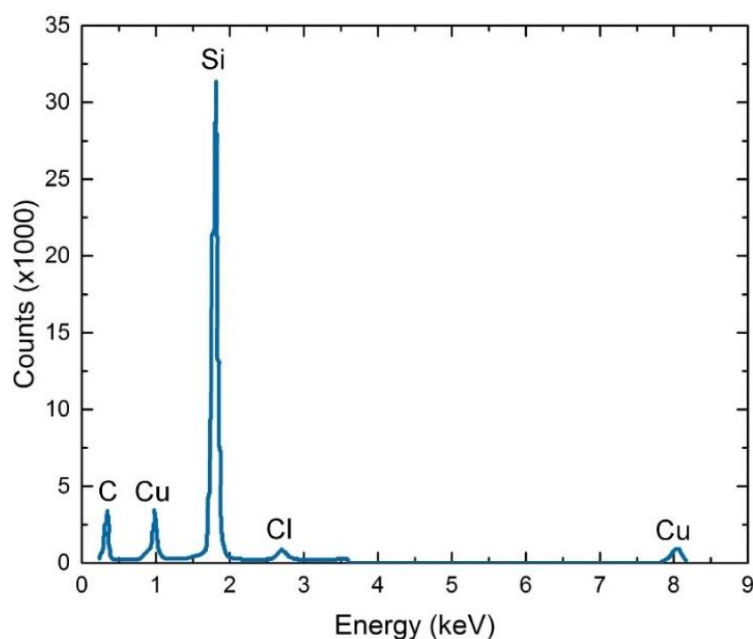


Figure 2-3: EDS analysis of the Cu NW material supported on a Si chip and carbon tape. Reproduced with permission from Ref. [72].

2.3.3 Cu NW/polymer composite samples preparation

Cu NW/PDMS composite samples were prepared by mixing the liquid PDMS with its affiliated cross-linker in a 1:10 volume ratio followed by an addition of varying amounts of freeze-dried Cu NWs. The resulting composites were poured onto a pre-cleaned glass plate that is bordered by aluminum foil. After degassing in a vacuum oven for 20 minutes, the samples were cured at 85 °C for 2 hours. We also prepared a neat PDMS sample for baseline κ measurement by degassing followed by curing under similar conditions as mentioned above. Finally, the cured samples were peeled off the glass plate and cut into 25 mm x 25 mm square samples.

To prepare Cu NW/PU composite samples, Clear Flex® 95 was used that came in two parts referred to as Part A and Part B. First, Part A and Part B were mixed at a weight ratio of 1:1.5 as mentioned by the vendor. Afterwards, varying amounts of freeze-dried Cu NWs were added and well mixed followed by degassing under vacuum for 20 minutes. The

uncured Cu NW/PU composite samples formed by the similar molding process as explained above for Cu NW/PDMS composite samples were cured at room temperature for 24 hours. For baseline κ measurement, neat PU sample was also prepared without any Cu NWs by curing at room temperature for 24 hours. Afterwards, the cured samples were peeled off the glass plate and cut into mm x 25 mm square samples. We chose PU to study the effect of the addition of Cu NWs on the κ of the technologically relevant polymer system. In addition, PU based samples can be air cured so they do not need higher temperatures as required by the PDMS samples to keep the curing times less than 24 hours. Various samples of Cu NW/PDMS and Cu NW/PU composites were prepared by varying the volume fraction (f) of Cu NWs from 0.1% to 4.1%. Cu NW volume fraction (f) was calculated by weighing the Cu NWs and neat polymer before mixing and using their respective densities. **Figure 2-4** shows the resulting Cu NW/polymer composite samples.

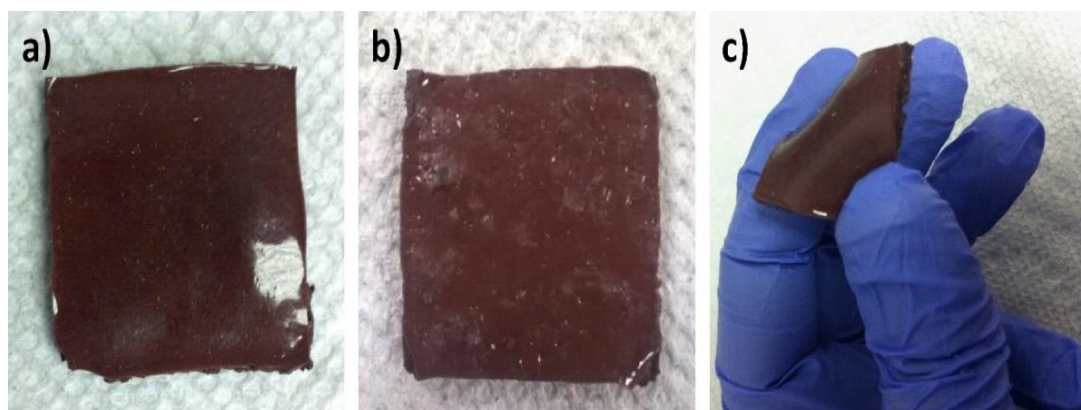


Figure 2-4: a) Cu NW/PDMS sample at 1.5 vol.% loading. b) Cu NW/PU composite sample at 2.7 vol.% loading. c) Bending of a flexible Cu NW/PDMS composite sample. Reproduced with permission from Ref. [72].

The most critical issue of Cu NWs is that Cu easily reacts with oxygen and forms surface oxides that are non-conductive in nature. This degrades the performance of the

NWs by limiting the electrical and/or thermal conduction [79], [80], [91]. Post-processing hydrogen annealing treatment was performed for selected samples in order to remove the native surface oxides and any organic compounds. The purpose of such treatment was to enhance the NW-NW and NW-polymer matrix thermal interfaces so that the effective κ of the composite would not be limited by interfacial thermal resistances. A similar approach was used by Cui *et al.* [92] as well to study the Cu NW-based transparent electrodes. For such treatment, Cu NWs were first annealed under flowing hydrogen at 360 sccm and 190 °C within a quartz tube furnace for 30 minutes and subsequently immediately mixed with PDMS or PU.

2.3.4 Experimental Setup

Figure 2-5 shows the experimental setup used to measure the κ of the neat polymers as well as the Cu NW/PDMS and Cu NW/PU composite samples containing different volume fraction of Cu NWs and annealing conditions. An assembly comprising of two thin Kapton heaters sandwiched between 2 mm thick aluminum plates was used as a central heating source as well as the hot side temperature measurement points. All components have the same 25 mm x 25 mm square cross section as the samples tested. The aluminum plates were custom machined to have grooves for providing access to thermocouples. The samples studied were placed on either side of this assembly.

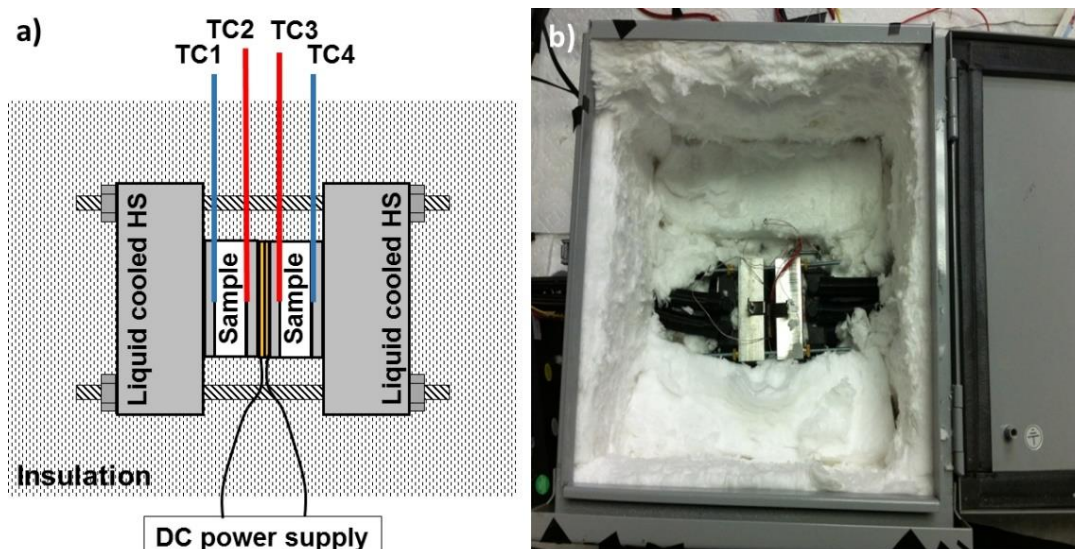


Figure 2-5: a) Annotated illustration of the steady-state thermal conductivity measurement setup in a symmetric configuration. Not to scale. b) Photograph of the actual assembled setup with topmost layers of insulation removed for visualization. The heat exchangers used in conjunction with the liquid cooled heat sinks are external to the enclosure on the left and right (not shown). Not to scale. Reproduced with permission from Ref. [72].

To measure the κ of neat polymer (PDMS or PU), 3 mm thick identical samples made of neat polymer were placed on either side in order to acquire a symmetric condition. In the case of κ measurement of Cu NW/polymer composite samples, the composite sample experimented was placed on one side of the assembly while the other side had corresponding neat polymer, thus forming an asymmetric condition. The custom machined aluminum plates with thermocouple access grooves like those used in heater assembly were placed on either end of the sample region. These aluminum plates serve as cold sides and the corresponding temperatures were measured by thermocouples that were fed through the grooves. The outer sides of the assembly consist of liquid cooled 75 mm x 75 mm aluminum blocks to maintain the cold side temperatures at ambient condition by means of a pair of external air-cooled heat exchangers.

To improve the thermal contacts, Arctic Silver[®] 5 thermal interface compound was applied at the interfaces. In addition, a set of four threaded rods were used to hold the entire assembly together by applying moderate pressure to the setup without deforming the samples. This entire setup was surrounded by several inches of low κ ($\sim 0.05 \text{ W m}^{-1} \text{ K}^{-1}$ at $200 \text{ }^\circ\text{C}$) alumina silica insulation on all sides and housed within a cubicle enclosure with access ports allowing for thermocouples, heater leads, and liquid cooling tubing to enter and leave.

2.3.5 Measurement

During an experiment, Agilent U8001A DC power supply with an output voltage of 0-30 V and a current of 0-3 A was used to supply a fixed electrical power to the heaters. Digital multimeters were used to measure the current (I) and the voltage drop (V) across the heaters. For the neat polymer samples, due to the symmetric condition, half of the total dissipated power $Q = IV/2$ flows through each sample towards its respective heat sink. The thermocouples (Type J, Omega) placed between the heater and the sample and between the sample and the aluminum plate (cold side) were used to measure the temperature drop across the samples. The measured temperatures were recorded by a computer-controlled data acquisition system. The thermocouple readings were monitored until a steady-state was reached, then the temperature gradient $\frac{dT}{dx}$ for the applied DC power was determined from the thermocouple readings and thickness of the sample assuming a linear distribution of the temperature. Temperature gradients for five different power values were obtained and the slope obtained from these data was used to calculate the thermal resistance of the sample under observation. Using this data, the slope of a linear fit

of measured heat flow through the sample Q_{sample} versus $\frac{dT}{dx}$ was obtained and used to calculate the thermal κ given by Fourier's equation:

$$\kappa = \frac{Q_{sample}}{\left(\frac{dT}{dx}\right) A} \quad \text{Eq. 2-1}$$

where A is the cross-sectional area of the sample and the value of the ratio $\frac{Q_{sample}}{\frac{dT}{dx}}$ is taken

from the slope of the obtained data points as shown in **Figure 2-6**.

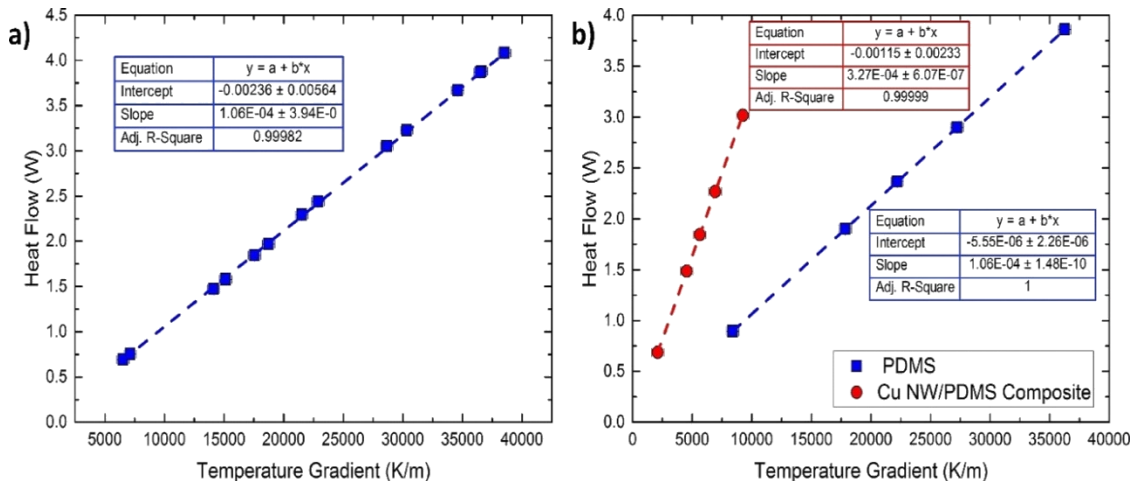


Figure 2-6: Representative heat flow vs temperature gradient data obtained at varying DC heating levels as described in the text, with the resulting slopes being used for calculating κ of the samples. a) Neat PDMS data taken in a symmetric configuration. b) As synthesized 4.1 vol. % Cu NW/PDMS composite sample data along with the values measured simultaneously for its associated neat PDMS reference sample in an asymmetric configuration. Error bars are included but are obscured by the data point symbols. The errors were ± 2 mW for Q and ± 510 K/m for $\frac{dT}{dx}$. Reproduced with permission from Ref. [72].

For neat polymers under symmetric conditions, we used $Q_{sample} = \frac{Q}{2}$ to calculate the κ with the known values of the heat flux, temperature gradient across the sample and their geometries. Also, the symmetry was verified by comparing the temperatures

measured on each of the two sides of the setup. The experimentally measured κ values of the neat PDMS and PU were compared with the literature values and presented in the Results section below. In the case of Cu NW/polymer composite samples of unknown κ , an asymmetric setup was used following the same experimental procedure. However, instead of using $Q_{sample} = \frac{Q}{2}$ as in the case of symmetric setup, first the heat flow through the neat polymer reference sample (Q_{ref}) was calculated from its known κ value, temperature gradient and geometry using Fourier's law. Then the heat flux through the composite sample of unknown κ value was obtained as the difference $Q_{sample} = Q - Q_{ref}$. This information was used along with the temperature gradients measured across the composite sample for multiple heating values in order to get the slope of Q_{sample} vs. $\frac{dT}{dx}$ and calculate the κ of the composite sample. Representative data obtained from a Cu NW/PDMS composite sample in an asymmetric setup along with its associated neat PDMS reference sample are given in **Figure 2-6 (b)**.

The standard error propagation analysis that was performed based on the modeling of steady-state heat loss through the thermocouple and the power leads, the accuracy of the thermocouples as specified by the vendors, and the digital calipers resolution, showed that the maximum uncertainties associated with this approach were +/- 2 mW for Q and +/- 510 K/m for $\frac{dT}{dx}$. Based on these uncertainties, an accuracy of +/- 0.05 W m⁻¹ K⁻¹ can be expected for the κ of the samples obtained from this experimental approach. These respective intervals were used as the basis for the uncertainty bars in the data plots that follow.

For composites filled with filler materials, the interfacial thermal resistance (ITR) (ITR) between the filler and the matrix - also known as Kapitza resistance R_k - can influence the overall thermal property of the composite [93]. The value of R_k strongly depends on the

surrounding matrix environment, as well as the processing and surface treatment of the filler material [94]–[96]. Since ITR degrades the performance of the composite, this work was also focused on minimizing the effect of such resistance by incorporating hydrogen annealing to the high AR Cu NWs. Two analytical models were implemented to quantitatively estimate R_k . These analytical models vary according to their fundamental assumptions. The values of R_k were extracted from the experimental data using the effective medium approach (EMA) as described by Nan *et al.* [93] and another model developed by Xue *et al.* [97]. These models were developed to study the effect of ITR on the thermal property of CNT composites. The model by Nan *et al.* is suitable for low loading levels as it assumes that the NWs are randomly distributed and isolated from each other. At high loading levels, NWs can touch each other forming whole or partial networks within the composite. Such condition is explained by the model by Xue *et al.* that has a broader range of applicability. The R_k values obtained by using these two models for various samples were then compared to determine the agreement or deviation from one another.

According to the model described by Nan *et al.* the effective κ of the composite is given by [93]:

$$\frac{\kappa}{\kappa_m} = \frac{3 + f(\beta_x + \beta_z)}{3 - f\beta_x} \quad \text{Eq. 2-2}$$

where κ_m is the thermal conductivity of the matrix alone and f is the volume fraction. The terms β_x and β_z are given by [93]:

$$\beta_x = 2 \frac{\kappa_{11}^c - \kappa_m}{\kappa_{11}^c + \kappa_m} \quad \text{Eq. 2-3}$$

$$\beta_z = \frac{\kappa_{33}^c}{\kappa_m} - 1 \quad \text{Eq. 2-4}$$

where κ_{11}^c and κ_{33}^c are the transverse and longitudinal equivalent thermal conductivities of a nanocomposite unit cell [93]. These values can be calculated by:

$$\kappa_{11}^c = \frac{\kappa_c}{1 + \frac{2a_k \kappa_c}{d \kappa_m}} \quad \text{Eq. 2-5}$$

$$\kappa_{33}^c = \frac{\kappa_c}{1 + \frac{2a_k \kappa_c}{L \kappa_m}} \quad \text{Eq. 2-6}$$

where d , L , and κ_c are the diameter, length, and κ of the filler NWs, respectively, and the term a_k represents a Kapitza radius defined by $a_k = R_k \kappa_m$.

Based on the FE-SEM images, the average diameter of the Cu NWs used in this calculation was 55 nm and the average length was 20 μm . The value of κ_c was carefully chosen by considering the various factors. The electrical conductivity (σ) of Cu NWs in sub-100 nm diameters at room temperature is smaller than the bulk values because of the surface scattering and grain-boundary scattering [98], [99]. Similar size effects would also change the κ of Cu NWs from the bulk values since the electrons can affect electrical and thermal conductivity. Previously, Stojanovic *et al.* developed models based on the Boltzmann Transport Equation (BTE) to study the effect of the size of metallic NWs on their electronic thermal conductivity κ_e and phonon thermal conductivity κ_{ph} at room temperature [66]. By using this study as a reference, we obtained κ_c of 139 $\text{W m}^{-1} \text{K}^{-1}$ by combining the values for κ_e and κ_{ph} for 55 nm Cu NW diameter and used this value for all the models in this work.

The approach presented by Xue *et al.* determines the effective κ of the composites by incorporating the interface thermal resistance with an average polarization theory. In

addition, the dependence of the effective κ of the composite on the filler length, the diameter and the concentration has been taken care of simultaneously. Therefore, this model is valid for describing the thermal or electrical properties of composite for any loading values of the filler including those in which the fillers may touch. According to this approach, the effective κ of the composite is given by [97]:

$$\frac{9(1-f)(\kappa - \kappa_m)}{2\kappa + \kappa_m} + f \left[\frac{\kappa - \kappa_{33}^c}{\kappa + 0.14 \frac{d(\kappa_{33}^c - \kappa)}{L}} + 4 \frac{\kappa - \kappa_{11}^c}{2\kappa + 0.5(\kappa_{11}^c - \kappa)} \right] = 0 \quad \text{Eq. 2-7}$$

where the symbols and their respective meanings follow those described above for the model by Nan *et al.*

In **Eq. 2-7**, besides the dimensions determined via the FE-SEM images, experimentally measured value for κ at various f , and the value for κ_c from the existing solution to the BTE, the only unknown variable for either model is R_k . The detail about the extraction of R_k is presented in the following section.

2.4 Results and Discussion

In order to validate the setup and procedure, neat PDMS samples were placed on either side of the heater. The κ of each neat PDMS sample was $0.17 \text{ W m}^{-1} \text{ K}^{-1}$, which was in good agreement with the values mentioned in the literature [38], [46], [100]. A similar procedure was followed for neat PU samples from which we obtained κ of $0.19 \text{ W m}^{-1} \text{ K}^{-1}$ for each PU sample. This value was also in excellent agreement with the values reported in the literature [100], [101]. After this validation, we measured the κ of the Cu NW composite samples with different volume fractions of Cu NWs and annealing conditions as explained above.

Figure 2-7 shows the κ of the Cu NW composite samples at different volume fractions. This shows that there is a gradual increase in the value of κ with an increase in the volume fraction of the Cu NWs. The values of κ for the as-synthesized samples and the annealed Cu NW/PU sample were $0.51 \text{ W m}^{-1} \text{ K}^{-1}$ and $0.62 \text{ W m}^{-1} \text{ K}^{-1}$, respectively, at the highest volume fraction of 4.1%. These indicate that there is more than a three-fold increase in κ of composites over the neat polymers.

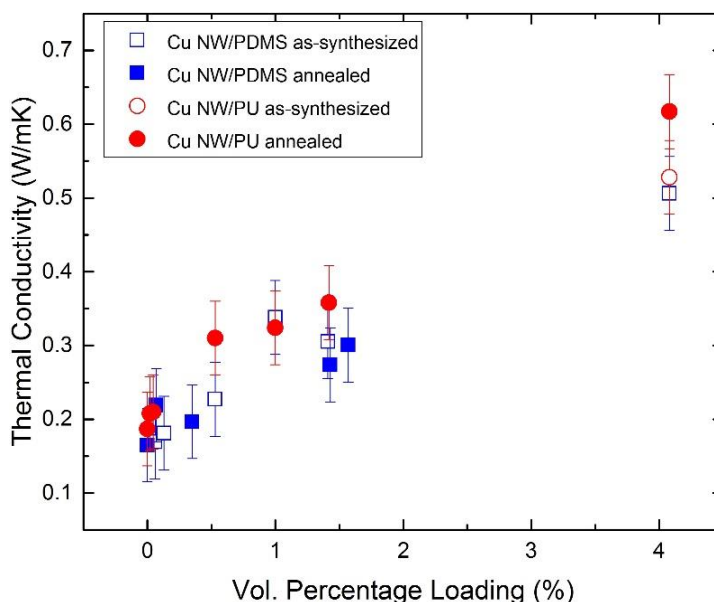


Figure 2-7: Plot of thermal conductivity of the Cu NW/PDMS composite and Cu NW/PU composite as a function of the volume fraction of Cu NWs. Reproduced with permission from Ref. [72].

Though there is a significant improvement in the composites compared to the neat polymers, the increase in the values of κ and the levels of enhancement achieved for the Cu NW/PDMS composites and the Cu NW/PU composites are still lower than several of those reported in the literature for various polymer composites. Consider, for example, at 1 vol. % the value of κ was $0.34 \text{ W m}^{-1} \text{ K}^{-1}$ for our Cu NW/PDMS composites. However, Balachander *et al.* [38] reported the value of κ for Au NW/PDMS composite to be 0.8 W

$\text{m}^{-1} \text{K}^{-1}$ even at 0.5 vol. %. On the other hand, the value of κ obtained by Munari *et al.* [102] for the Ag NW/PDMS composite was only $0.15 \text{ W m}^{-1} \text{K}^{-1}$ at a volume loading of 1%, which is lower than the κ of our Cu NW/PDMS composite. Also, the κ of the composite depends on NW loading. When the NW loading was relatively small ($f < 1.5$ %), our Cu NW composites showed enhancement in κ comparable to that of the polymer nanocomposites such as epoxies and PDMS filled with CNTs [103], graphene [104] and gold nanorods [38] as shown in **Figure 2-8**.

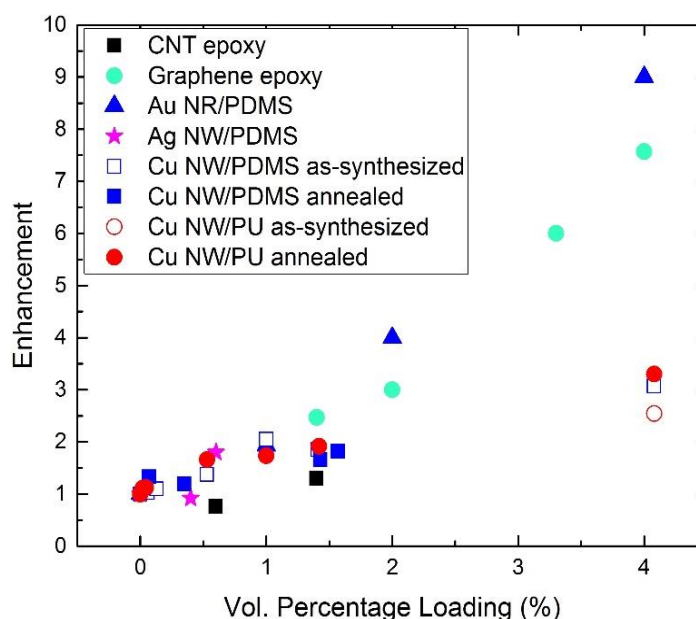


Figure 2-8: Thermal conductivity enhancement for the Cu NW/PDMS composite and Cu NW/PU composite as a function of the volume percent loading of Cu NWs relative to their respective neat polymers. Also plotted are reported thermal conductivity enhancement values for composites filled with carbon nanotubes [103], graphene [104], gold nanorods [38] and silver NWs [66]. Reproduced with permission from Ref. [72].

At higher loading levels, a deviation in the trend can be observed between the Cu NW composite samples in this work and other composite found in the literature. For Cu NW/PDMS and Cu NW/PU composites, there is a linear relationship for the loading levels

up to 4.1 vol %. However, there is a non-linear increase in κ with increasing f for many other nanocomposites that show larger κ enhancement. This behavior can be accounted to the formation of the percolative network within the material. For our Cu NW composite samples, the trend is linear, even at the highest f values. This might be due to the fact that the percolative thermal network has not yet formed.

Based on the high AR of synthesized Cu NWs and the microscopy analysis of the composite samples with high values of f , the reason for not having a percolative network is not likely related to having few NWs or having too low ARs to form at least partial percolative network. In such sub-percolation threshold condition, the overall resistance to the thermal transport through the composite is highly dominated by the bulk polymer matrix. The presence of ITR at the NW-NW and NW-polymer interfaces are assumed to be the main cause for the lack of percolative thermal network. The root cause for the presence of ITR may be attributed to the native oxide barrier layer formed on the surface of the Cu NWs. Hydrogen annealing was performed on some selected samples to remove the native oxide layer from the as-synthesized Cu NWs. This can ultimately help to improve the effective κ of the Cu NW composite samples by improving the interfacial contact between the Cu NWs. A simple electrical test was performed on the Cu NWs before and just after hydrogen annealing, to make sure that the hydrogen annealing removes the native oxide layers from the NWs and thus improves the NW-NW contacts. The electrical resistances of the Cu NWs before hydrogen annealing were very high, indicating their non-conducting nature. After annealing, the Cu NWs exhibited electrical resistances on the orders of a few kilohms, in agreement with other works in which hydrogen annealing has proven effective for removing native oxide layers and hence improving the conduction within Cu NW networks [92].

As explained above, the Cu NWs were mixed with the polymers immediately after the hydrogen annealing with the intention of minimizing re-oxidation via air exposure. Even though the hydrogen annealing prior to mixing was effective in removing the native oxide layer, results in **Figure 2-7** show that for the same f level, the difference in κ for the composites containing annealed vs. as-processed Cu NWs fell within the measurement uncertainty. This indicates that the residual oxygen present within the polymer may play an important role for re-oxidation of the Cu NW surfaces even after mixing and degassing. In addition, similar results were obtained for the PDMS (cured at elevated temperature) and PU (cured at room temperature) composites indicating that the moderate temperatures do not strongly affect the re-oxidation process.

The effective ITR (symbolized here as R_k) values were computed for the composites containing as-processed as well as hydrogen annealed Cu NWs using the models described by Nan *et al.* and Xue which are shown in **Figure 2-9**.

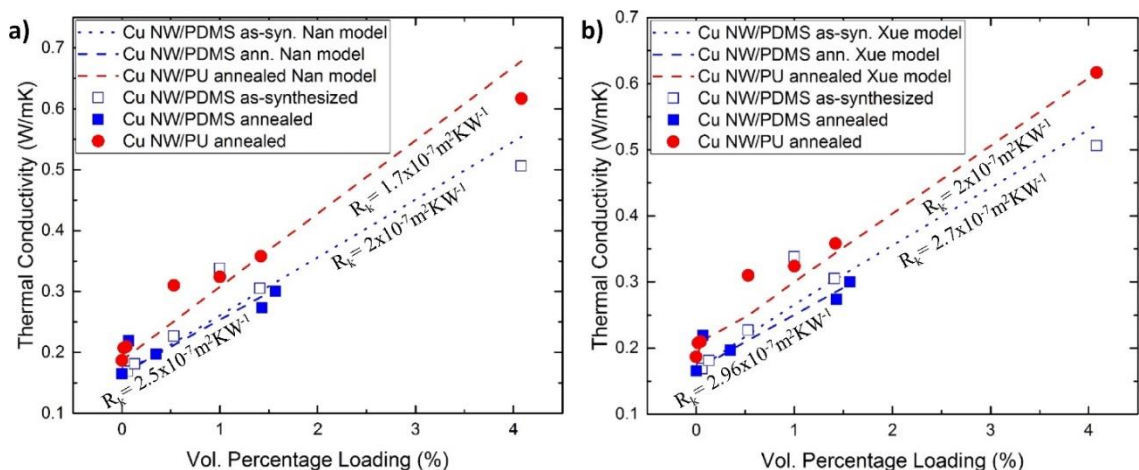


Figure 2-9: Thermal conductivity values of CuNW/PDMS and CuNW/PU composite samples plotted along with the theoretical values of R_k and thermal conductivity values predicted by the model developed in different literature a) Xue Model b) Nan Model. Reproduced with permission from Ref. [72].

The values extracted from both models fell within the range $R_k \sim 1.7 - 3.0 \times 10^{-7} \text{ m}^2 \text{ K W}^{-1}$. Therefore, both models can conceivably be used to describe the thermal transport behavior of the Cu NW composites. The upper bound of $3.0 \times 10^{-7} \text{ m}^2 \text{ K W}^{-1}$ was obtained from the annealed Cu NW/PDMS sample set analyzed using the Xue model, whereas the lower bound of $1.7 \times 10^{-7} \text{ m}^2 \text{ K W}^{-1}$ corresponds to the annealed Cu NW/PU sample set analyzed via the Nan *et al.* model. For the R_k values determined in this manner, the maximum relative uncertainty of $\sim 23\%$ was obtained by incorporating the uncertainty of each data point and its impact on the slope by which R_k was obtained. Contrarily, Balachander *et al.* [38] reported that the κ of their Au NW/PDMS composites were more than the predicted κ of a non-percolated model assuming $R_k \sim 10^{-8} - 10^{-9} \text{ m}^2 \text{ K W}^{-1}$. This implies that their composite material exceeded the percolation threshold. The better performance of the Au NW composites compared to our Cu NW composites may be attributed to the natural oxidation resistance of Au. To improve the performance of the Cu NW composite, special handlings such as composite preparation under vacuum or protective inert atmosphere until fully cured is necessary. In this case, the initial cost might be high for buying the vacuum system. In the long run, the overall cost of synthesizing a large amount of Cu NWs will be small compared to the Au NWs as Au is more expensive than Cu, so this initial high cost will be repetitive if more Au NWs are needed.

Furthermore, the price of Au often fluctuates so this will also make use of Au NWs more expensive. Another option would be the alignment of NWs in the composites along the preferred heat flow direction as reported by Barako *et al.* [87]. Dense arrays of vertically aligned Cu NWs were directly synthesized onto the substrates via templated electrodeposition technique and a sacrificial over plating layer was also used to achieve improved uniformity. The value of κ of the Cu NW composites was as high as 70 W m^{-1}

K^{-1} by aligning the Cu NWs parallel to the heat flow. However, such composites might not be acceptable for some applications due to highly anisotropic nature. For example, if the $\kappa_{in-plane}$ is very high compared to the $\kappa_{cross-plane}$, most of the heat will flow towards the neighboring electronic components which will ultimately produce more heat on such components. The values of R_k mentioned above were calculated using a nanowire thermal conductivity κ_c of $139 \text{ W m}^{-1} \text{ K}^{-1}$ based on the existing solution to BTE with diffuse scattering at the same diameter as those used in this work [66]. Models described by Nan *et al.* and Xue can be used to find the lower bound on κ_c with R_k approaching zero and figuring out what lower values of κ_c may be able to provide the results matching with the experimentally determined results of the composites. By following this approach, κ_c values in the range of $26\text{-}38 \text{ W m}^{-1} \text{ K}^{-1}$ would result in the effective κ values equal to those obtained in this work. The value of κ_c can be lower than the optimal $130 \text{ W m}^{-1} \text{ K}^{-1}$ because of the grain boundaries, point defects, or other internal imperfections within the NWs; however, a 5X reduction in nanowire κ coupled with a thermally perfect Cu NW/polymer interface represents an unlikely scenario. Therefore, it is more likely that the κ_c lies within the range of $26 - 139 \text{ W m}^{-1} \text{ K}^{-1}$ and the upper limit to R_k is $3.0 \times 10^{-7} \text{ m}^2 \text{ K W}^{-1}$, with the true combination of κ_c and R_k falling somewhere within these respective bounds.

Although there is still more room for enhancing the effective κ of the Cu NW-based flexible polymer composites, the Cu NW/PDMS and Cu NW/PU composites developed in this work still show great potential for dissipating heat from the electronics-like concentrated heat source. This is demonstrated in **Figure 2-10** that shows the thermal images taken from neat PU sample and a Cu NW/PU composite sample containing 4.1 vol% of Cu NWs, each consisting of identical serpentine Au heaters shadow-evaporated

onto their surfaces. Each sample was heated with the same amount of Joule heating and the thermal images were taken using almost identical temperature scales. From the thermal images, the maximum temperatures of the resulting hot spots were compared, which was considerably lower (~ 10 °C) for the Cu NW/PU composite sample than that of the neat PU sample. The DC heating voltages were applied to the top right and bottom left contact pads for both samples; hence, a slight asymmetry can be noticed in the images.

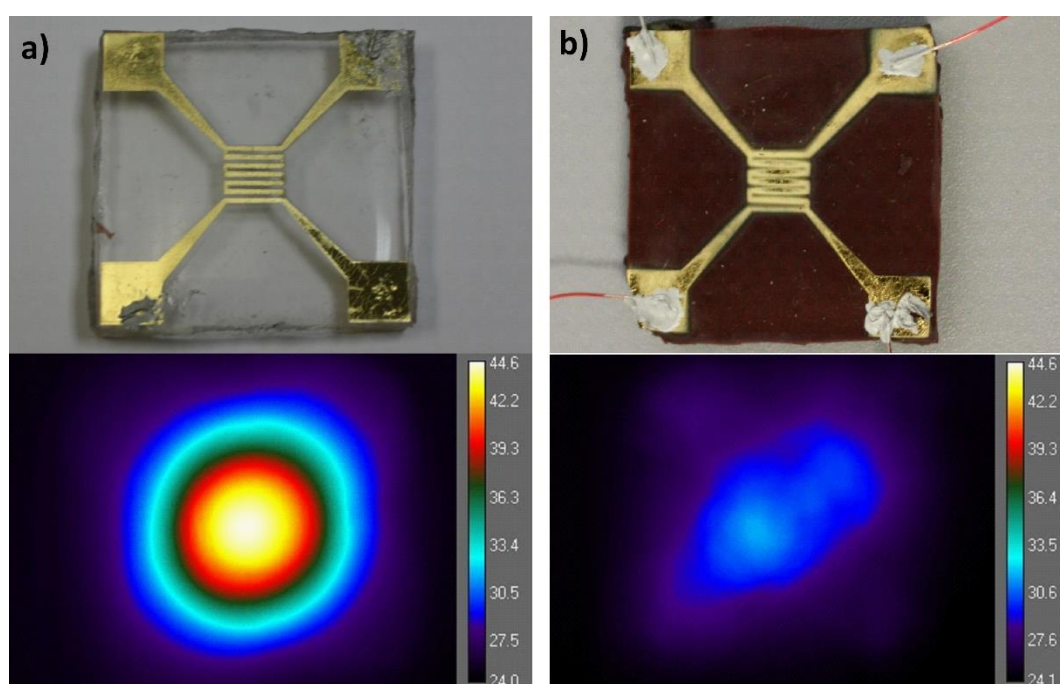


Figure 2-10: a) A neat PU sample with shadow-evaporated Au serpentine heater and its associated temperature map at steady-state after applying a fixed Joule heating power. b) The annealed Cu NW/PU sample with 4.1% volume loading and its associated steady-state temperature map after applying the same Joule heating power as was used for the neat PU sample. Reproduced with permission from Ref. [72].

2.5 Conclusion

In this work, high AR Cu NWs, synthesized through a simple solution-based method, were used to create flexible, thermally conductive Cu NW/PDMS and Cu NW/PU

nanocomposites. The effective κ of the composites containing varying amounts of Cu NWs were measured using a steady-state measurement method. An intermediate hydrogen annealing treatment was performed for selected samples with the intention of removing native surface oxides. The value of κ increased linearly with an increase in volume fraction of Cu NWs and achieved a threefold increase in κ over neat polymers at a highest loading fraction of 4.1 vol %. The factors limiting the increase in effective κ of the composites may be the surface oxides and interfacial thermal resistance as indicated by the linear relationship including the comparable results between as-processed and annealed samples. In spite of these limitations, the Cu NW composites showed superior heat spreading capability from a localized hot spot as would be experienced by a flexible electronics element than the neat polymers.

CHAPTER 3

SUPERIOR, PROCESSING-DEPENDENT THERMAL CONDUCTIVITY OF CELLULOSE NANOCRYSTAL-POLY (VINYL ALCOHOL) COMPOSITE FILMS

3.1 Introduction and Motivation

In electronic devices, the substrate is also one of the main components, and the properties of the substrate include flexibility, surface roughness, mechanical strength, optical transmittance, and maximum processing temperature. Electrically insulating polymers are widely used in traditional electronics as printed circuit boards (PCBs), device holders, or TIMs because of the ease of processability, low cost, and low density compared to other materials. However, the neat forms of such polymers have very low κ because of defects, voids, impurities, random polymer chains, or entanglements [105], [106]. There is a growing trend towards flexible electronics and away from Si-based rigid electronics. Popular materials that have been extensively used as substrates for flexible electronics include PET, PI, and polyethylene naphthalate (PEN). These are the petroleum-based materials that take a very long time for degradation.

Hence, they are expensive from a life cycles point of view. Furthermore, they are not biodegradable and hence environmentally less attractive [50]. So there is increasing interest in green flexible electronics with high-performance substrates that are naturally available, thermally stable and conductive with [107] high flexibility, transparency, and

better strength [108]. This is possible by using the materials from natural resources and hence make the technology more sustainable [107], [109]. Renewable materials such as cellulose, lignin, chitosan, gelatine, starch, polylactic acid (PLA), polyglycolic acid are abundant in nature and biodegradable, and therefore play a very important role in carbon capture and sequestration and ultimately help in the reduction of global warming. Also, they are flexible, non-petroleum based, renewable, sustainable, and have low environmental, animal/human health and safety risk [110].

Substrate materials synthesized from renewable materials, such as cellulose, can be a suitable candidate for the sustainable flexible electronics in the future. Cellulose can be obtained from various natural resources such as wood, plants, algae, tunicate, bacteria [110]. Plants are the most common sources of cellulose, with cellulose being the main skeletal component of plants. In addition to hemicelluloses and lignin, plant cell walls consist of 40-50 wt% cellulose. Cellulose represents about 1.5 trillion tons of total annual biomass production, and thus represent an almost inexhaustible resource so they are almost polymeric raw materials for fulfilling the increasing demand of eco-friendly and biodegradable products [111]. The promising properties of cellulose nanoparticles (CNs) include high AR, low density [110], flexibility, high mechanical strength, relative thermo stabilization, piezoelectricity [109], hydrophilicity, chirality, large specific surface area, biocompatibility, nontoxicity, and low cost [112]. Moreover, some cellulose nanomaterial composites have tensile strengths greater than cast iron and very low CTE. Such remarkable properties make cellulose-based materials suitable for use in emerging technologies that include but are not limited to flexible displays, templates for electronic components, supercapacitors, batteries, barrier films, antimicrobial films, transparent

films, reinforcing fillers for polymers, biomedical implants, pharmaceuticals, drug delivery, fibers and textiles, separation membranes, and many others [110].

The cell walls of plants are made of macrofibers. These macrofibers are composed of microfibrils, which in turn are comprised of nanofibrils of cellulose. The nanofibrils of cellulose have highly ordered cellulose chains (crystalline) as well as regions with disordered cellulose chains (amorphous-like) in a row [110], [113]. The crystalline part is very strong due to the strong hydrogen bond of hydroxyl groups in cellulose, but the amorphous part can be broken by strong mechanical force or special solvents. There are four polymorphs of crystalline cellulose: cellulose I, II, III and IV.

Cellulose I is the natural cellulose that is produced by several organisms (plants, algae, bacteria) and they are thermodynamically metastable. Cellulose II and III can be obtained by modifying cellulose I. Cellulose II has a more stable crystalline structure than cellulose I [114]. Nanocellulose (NC) can be extracted from the natural resources in the form of CNCs and cellulose CNFs. They can be extracted from cellulose microfibrils using various methods that include pre-treatments, disintegration or deconstruction processes: chemical pulping and bleaching, mechanical grinding, high-pressure homogenization, acid hydrolysis, enzyme treatment, and solvent treatment. CNFs have fiber-like structures with lengths on the order microns and widths of 4-20 nm. They have crystalline as well as amorphous parts [110]. They can be produced from cellulose fibrils using a variety of mechanical treatments such as homogenization, microfluidization, refining, grinding, and ball milling. They can be used as reinforcing agents in composites due to their high mechanical strengths, low cost and availability [112], [115].

CNCs, also known as cellulose whiskers or nanocrystalline cellulose, are rod-like or whisker-shaped particles obtained after acid hydrolysis of cellulose-rich natural resources. Acid hydrolysis dissolves the amorphous region, thus leaving only the crystalline regions. CNCs have a high AR with length ~50-500 nm and width ~5-20 nm. They are ~100% cellulose and highly crystalline (54-88%) [110], [116]. Other excellent properties of CNCs include: high tensile strength (~ 7.5 GPa), high axial stiffness (~ 150 GPa), low coefficient of thermal expansion (~ 1 ppm K⁻¹), thermal stability up to ~ 300 °C, low density (1.6 gm cm⁻³), high κ , and optical transparency [60], [61], [108], [117]. Research studies have shown that the addition of CNCs to a wide variety of natural and synthetic polymers can improve the properties (mechanical, optical, thermal barrier) of the resulting composites [117]–[120]. Furthermore, they have been used as transparent media in organic electronics [121], barriers in packaging applications [122], and anti-counterfeiting in security applications [123]. CNCs can also be used as coating [124], film [125], or aerogel [126]. More importantly, there is increasing interest in CNCs because they are inherently renewable and sustainable, have very low environmental, health and safety risks, and they have the potential to be processed in industrial scale at a very low cost [127]. Due to all these reasons, there has been a great deal of interest towards NC both in academic and industrial sectors.

Generally, fillers are added to the polymers for improving the properties (thermal, mechanical, optical) of the resulting composites. Enhancements are possible only by using a large amount of such fillers, which can ultimately affect the final weight and optical properties of the final composites. The use of filler materials that have at least one nanoscale dimension can be useful to resolve such issues. Moreover, popular materials

used for this purpose are petroleum-based polymeric materials [128]. Cellulosic nanomaterials can be a suitable candidate as filler materials since they can be obtained from natural resources so they are eco-friendly, renewable and sustainable [128]–[131]. To resolve the issue of thermal management of electronic devices, polymer nanocomposites containing CNCs can be used as substrates to improve the thermal properties and take the heat away from the electronic devices. A composite qualifies as fully renewable and biodegradable if the matrix and filler are produced from renewable resources [129]–[131]. CNCs are compatible only with few polymer matrices and PVA is one of them [128]. PVA is flexible, biodegradable, non-toxic [132], [133] and one of the most widely produced synthetically derived water-soluble polymers [134]. Being environment-friendly, PVA can be a good alternative to commonly used petroleum-based polymers such as polyethylene [135]. The exceptional properties of PVA include good thermal stability, optical properties, and oxygen barrier properties [136]. PVA has been incorporated with nanocellulose for a variety of applications such as polymeric membranes [137], films [138], and fibers [139]. Moreover, PVA does not adsorb on cellulose in water and it has lots of hydroxyl groups that form strong hydrogen bonds with those of cellulose in the dry state [140] while filling the “holes” in CNCs leading to low interfacial resistances and very efficient thermal transport across the interfaces. Thus, polymer nanocomposite containing CNC and PVA can be very useful for thermal management of flexible electronics [130], [131], [133].

Only a few studies have been done in the past regarding the thermal properties of cellulose-based materials for their applications as substrates for flexible electronic devices. It has previously been shown that the thermal properties of composites can be improved by the inclusion of NC. Shimazaki *et al.* [141] created a cellulose nanofiber (CNF)/epoxy resin

nanocomposite that was transparent with low CTE values and highly thermally conductive with κ value of $\sim 1.1 \text{ W m}^{-1} \text{ K}^{-1}$, which was nearly seven times higher than that of the neat epoxy matrix. The crystalline nature of the CNFs was attributed for such improvement since it provides excellent phonon pathways through the nanocomposite [141].

Bahar *et al.* [142] also reported an increase in the κ value of the polymer matrices by mixing with cellulose nanowhiskers which indicate that NCs have the potential for the κ enhancement. Uetani *et al.* [143] reported the κ of tunicate nanowhiskers (TNWs) to be as high as $\sim 2.5 \text{ W m}^{-1} \text{ K}^{-1}$ in the in-plane direction, which was about eight times greater than in the thickness direction. The fiber orientation was attributed for the anisotropy of κ . Also, the $\kappa_{in-plane}$ of the flexible NC skeleton was as high as $2.5 \text{ W m}^{-1} \text{ K}^{-1}$, which was $\sim 234\%$ thermal conductivity enhancement from the matrix acrylic resin. This value is higher than those of the plastic films currently used for flexible electronics substrates [144].

These findings suggest that NCs can be used as the substrates for thermal management of flexible electronics. In another study, Uetani *et al.* [145] investigated the bacterial cellulose (BC) nanopaper with highly oriented NCs formed by stretching the BC pellicles and reported κ of $2.1 \text{ W m}^{-1} \text{ K}^{-1}$ in the drawing direction and κ of $0.94 \text{ W m}^{-1} \text{ K}^{-1}$ in the transverse direction. The κ anisotropy of 220% suggests that heat guiding substrate materials can be produced by assembling the drawn BC pieces without the addition of any thermally conductive fillers, thus indicating substrate materials that can efficiently cool the next generation of flexible electronic devices.

Focusing on thermal transport, NCs obtained from natural resources have many advantages over the petroleum-based polymers. First, the extended-chain crystals of NCs form structures with relatively low defect density; hence, heat can propagate effectively

through lattice vibration with minimum phonon scattering [143]. On the other hand, most of the polymers have amorphous regions, voids, and chain ends that act as defects or interfaces, thus impeding the thermal conduction [146]. Second, the higher tensile modulus of polymeric superfibers can be positively correlated with the κ [147]-[149]. For example, tensile moduli of the tunicate NCs are very high (~ 150 GPa) [150]. Third, crystalline structures are deformed when ultra-drawn plastic fibers are used to form two-dimensional thin films for κ enhancement. However, a simple filtration of NC suspensions can form a “nanopaper” with strong hydrogen bonding between the NC surfaces [151]. Due to these advantages and unique processing-structure-property dynamic, it is very important to study the thermal properties of cellulose-based materials.

The structural configuration of a crystalline domain can also greatly influence the thermal, mechanical and optical properties of CNC materials [108], [116], [125], [152], [153] according to the crystal domain organization. The organization of crystalline domain can be changed by using external forces such as shearing or electromagnetic fields to align the CNCs in specific directions. Using the materials with anisotropic configuration, properties can be enhanced directionally in the orientation direction. For gas barrier applications, Kalia *et al.* [154] used anisotropic CNC nanocomposites to improve Young’s elastic modulus, yield stress, and ultimate tensile strength with better transparency. Shrestha *et al.* [155] reported very low hygroscopic strain in the axial direction for an anisotropic film that is very important for electronic packaging [61]. Diaz *et al.* [156] found highly anisotropic in-plane thermal expansion with the highest CTE of ~ 9 ppm K^{-1} in the direction parallel to CNC alignment while maintaining film transparency, but the films without CNC orientation exhibited an isotropic CTE of ~ 25 ppm K^{-1} . The thermal

expansions of CNC films were attributed to single crystal expansion and CNC-CNC interfacial motion. CNC films that are transparent with smaller CTE values are suitable for organic electronic devices, especially LEDs [141], [157]. Diaz *et al.* [108] further reported a four-fold increase in κ in the aligned direction compared to the isotropic configuration.

In order to efficiently alleviate local heating from flexible electronic devices, the development of a substrate with high $\kappa_{\text{in-plane}}$ is a great challenge. It is therefore desirable to study the relationship between κ and structural organization of CNCs which can further enable the control of heat flow through the nanomaterials and ultimately resolve the issue of thermal management of flexible electronic devices.

3.2 Research Objectives

The main objective of this chapter is to investigate thermal properties of CNC-PVA composite thin films for potential application in the thermal management of flexible electronics. To achieve this goal, the following specific objectives were to be achieved through this research:

- Determine the $\kappa_{\text{in-plane}}$ of the CNC-PVA composite thin films containing different amounts of CNC and PVA with different molecular weights of PVA, using a modified steady-state measurement technique.
- Investigate the parameters affecting the $\kappa_{\text{in-plane}}$ of each sample.
- Demonstrate the application of CNC-PVA composite thin films for flexible electronics.

The CNC-PVA composite films of varying internal structure were examined to understand how the processing affects the CNC ordering and, hence, the films' $\kappa_{\text{in-plane}}$ magnitude and directional dependence. The $\kappa_{\text{in-plane}}$ of each sample was measured using a

modified steady-state measurement technique. Structural organization of CNCs can greatly influence the thermal property. The anisotropic aligned samples were prepared with different order parameters (S). Therefore, the dependence of $\kappa_{\text{in-plane}}$ on S was also analyzed in detail. Furthermore, the effect of the addition of PVA on the effective $\kappa_{\text{in-plane}}$ of the CNC-based films and the ITR was studied through a combination of experimentation and modeling.

3.3 Experimental Materials and Methods

3.3.1 Sample Preparation

The CNC film samples were prepared by Reaz A. Chowdhury from Prof. Jeffrey P. Youngblood's group at Purdue University.

3.3.2 Experimental Setup and Measurement

The CNC film samples were fragile; hence, applying high pressure to maintain good thermal contacts at the interfaces can break the samples. Therefore, the setup mentioned in CHAPTER 2 could not be used. Therefore, a modified steady-state bridge method similar to the one employed by Benford *et al.* [158] was used to measure the $\kappa_{\text{in-plane}}$ of the free-standing tape/thin films where a highly conductive silver paint is used to maintain good contact at the interfaces. An annotated 3D illustration of the measurement stage used in this work is given in **Figure 3-1**. The stage used for the measurement consists of two identical platforms, each with a 25 mm X 7 mm X 1 mm Cu plate, backside serpentine Nichrome wire heater, PFA-insulated 0.127 mm diameter Type J thermocouple, and a 20 mm long 2 mm diameter threaded Nylon support. An adjustable stainless-steel base with a thermal mass much larger than that of the platforms was used to support the Nylon platforms. During measurements, electrical power was supplied to one of the

platforms via 15 cm long, 0.255 mm diameter insulated lead wires (2 per platform) that attach to the Nichrome heater at the copper plate for localizing Joule heating while also minimizing parasitic heat conduction along the leads. Both platforms were made identical for the sake of the thermal circuit analysis used to determine $\kappa_{\text{in-plane}}$.

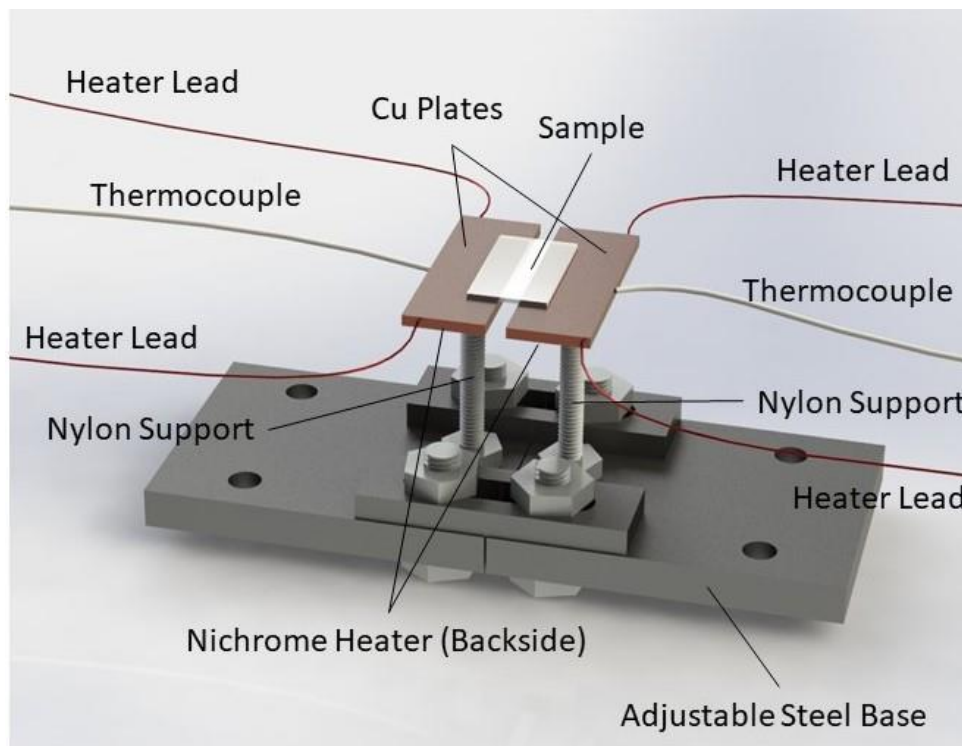


Figure 3-1: Annotated 3D drawing of the measurement stage. Silver paint for affixing the sample not shown.

The CNC film under the study was cut into rectangular sections 3-5 mm in width and up to 25 mm in length for mounting. For anisotropic films, this was done either in perpendicular or parallel to the direction of crystal alignment. In some cases, multiple samples were stacked together for increasing the signal strength relative to the background. Vacuum-compatible high conductivity silver paint (SPI Supplies) was used to affix the samples on either end to the Cu plates, which left a part of a clean film sample of known

length, width, and total thickness suspended between the two Cu plates. The whole stage setup was loaded into a chamber where a vacuum of $\sim 10^{-6}$ Torr (this was the best vacuum that could be achieved) was created via mechanically-backed turbo pump for minimizing the convective heat transfer. The leads for electrical power and thermocouples were extended across the chamber walls through a vacuum-compatible feedthrough.

Once the vacuum was stabilized, Joule heating induced to one of the Nichrome heaters via a precision DC power supply raised the temperature of the corresponding Cu platform. This caused the heat to be conducted along the suspended length of the sample and ultimately to the Cu platform on another side and hence raised its temperature as well. After measuring the Joule heating in the Nichrome heater and the temperature of each Cu platform, the $\kappa_{\text{in-plane}}$ of the film sample was determined via conduction analysis of the setup's thermal circuit as mentioned by Diaz *et al.* [108]. The steady-state temperature differences were measured at multiple Joule heating powers for each sample to minimize the measurement uncertainty. The plot of the temperature difference versus heat conducted through the sample was used to determine the sample's thermal resistance.

First, the measurement was performed without a sample present to determine the "background" G which accounts for the heat conduction through the residual air within the chamber. This was subtracted from the G value obtained with a sample present that was at least 2X of the background G for all samples. The main source of experimental error was associated with the inherent accuracy of two thermocouples ($\pm 1.1^\circ\text{C}$). Standard error propagation was used to obtain an upper limit ($\pm 19.2\%$) of measurement uncertainty which is associated with the results presented in this work.

3.4 Results and Discussion

3.4.1 Effect of (CNC: PVA) composition with isotropic configuration:

For any polymer system, the $\kappa_{\text{in-plane}}$ depends on nanofiller's percentage, AR, orientation as well as the matrix-filler interaction which also determine the free volume (as an active defect site) of polymer segments; in short, how the effect of the structure on the phonon propagation and scattering within the material [106]. **Figure 3-2** and **Figure 3-3** show the measured $\kappa_{\text{in-plane}}$ of CNC-PVA composite films of different CNC to PVA ratios having PVA of molecular weight of 124-186 k and 89-98 k, respectively. It can be observed that the $\kappa_{\text{in-plane}}$ increased with an increase in the CNC percentage compared to the neat PVA (0% CNC). The obtained values were within the expected range.

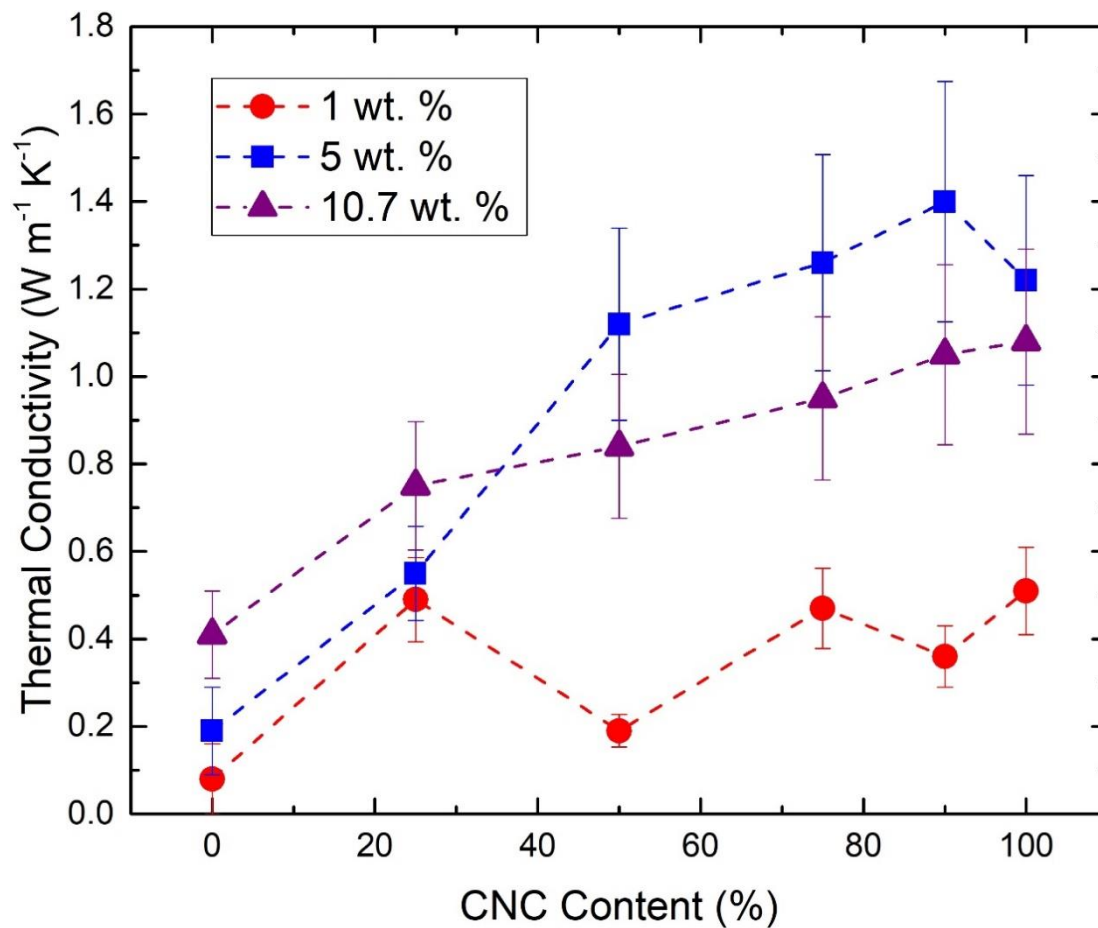


Figure 3-2: Thermal conductivity of un-sheared CNC: PVA films versus CNC content of the final film. Data shown is for 1, 5, and 10.7 initial CNC and PVA weight percent used during fabrication. The PVA molecular weight was 124-186 k.

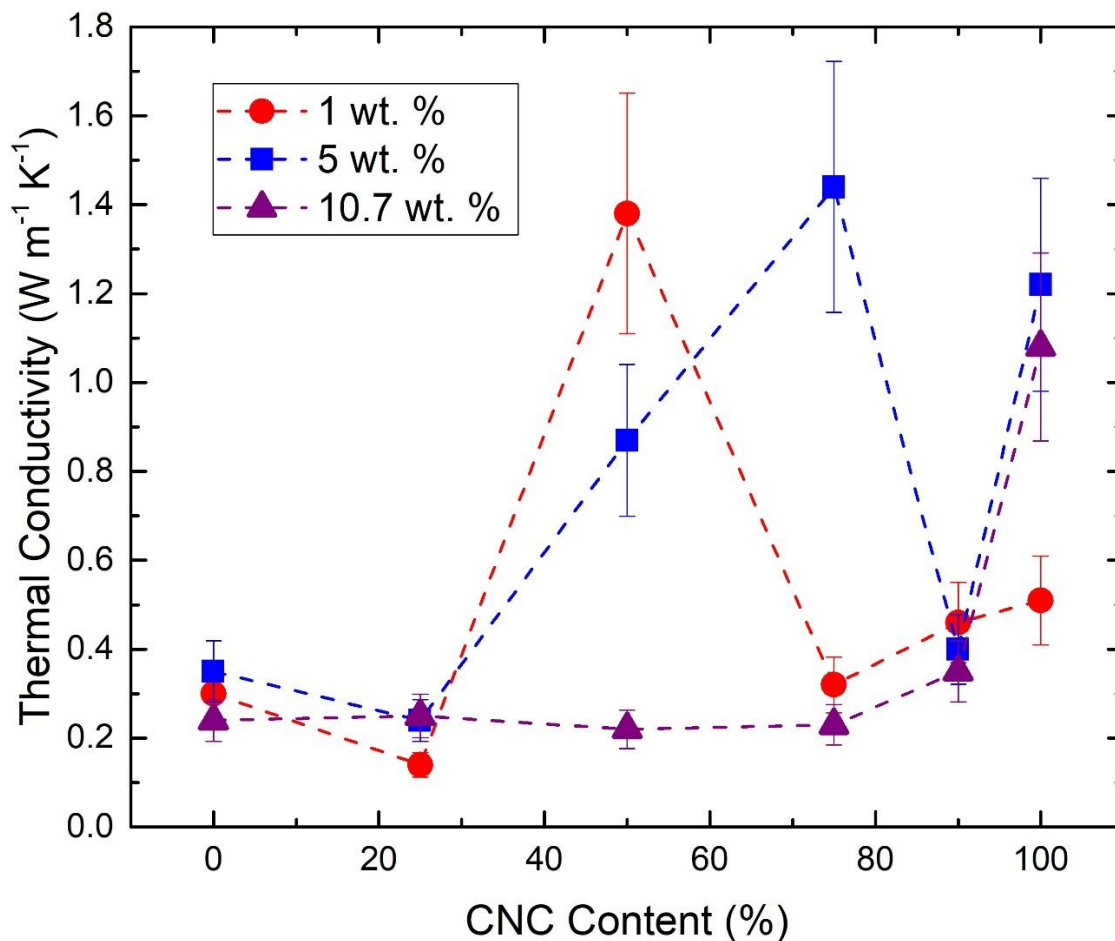


Figure 3-3: Thermal conductivity of un-sheared CNC:PVA films versus CNC content of the final film. Data showed is for 1, 5, and 10.7 initial CNC and PVA weight percent used during fabrication. The PVA molecular weight was 89-98 k.

The lower $\kappa_{\text{in-plane}}$ of the long-chain PVA may be due to the presence of entanglements with globular structures that provide more free volume, hence, more phonon scattering. Variable $\kappa_{\text{in-plane}}$ were obtained for the bulk CNC films (100% CNC), and better results were observed for initial concentrations above 1%. Never-dried CNC suspension is believed to have a chiral nematic configuration that is strongly concentration-dependent [159], [160]. The dilute CNC suspensions may have an organized chiral nematic structure compared to the suspensions with higher CNC concentration that may not have well organized chiral nematic structure because of frustrated ordering; therefore, they can

instead be highly random. However, a low $\kappa_{\text{in-plane}}$ was observed for a chiral nematic structure in this work likely due to more free volume. Also, CNCs were randomly distributed in the transverse and longitudinal direction because of the generally isotropic configuration; therefore, the results shown in **Figure 3-2** and **Figure 3-3** are associated with isotropic orientation.

The $\kappa_{\text{in-plane}}$ of CNC-PVA composites were very different than expected. The $\kappa_{\text{in-plane}}$ of pure CNC film was much higher (at least 2 to 6 folds) than the neat PVA film and was depended on the concentration. However, this binary composite system did not follow the general rule of mixtures. The CNC-PVA composite films with higher molecular weight PVA (124-186k) showed enhanced $\kappa_{\text{in-plane}}$ for PVA solid loading between 10-25 wt%. However, the results were more complex for the lower molecular weight PVA (89-98 k) which showed an increase in the $\kappa_{\text{in-plane}}$ with PVA solid loading between 25-50 wt% that was also depended on the initial solution concentration.

The experimental results suggested that more enhancement of $\kappa_{\text{in-plane}}$ can be achieved at the higher CNC loading region where PVA molecules can act as a binder or interstitial filler between the CNCs, thus reducing the effective ITR for this binary composite system compared to the pristine CNC materials as shown in **Figure 3-4**. The hydroxyl groups of PVA molecules can form strong hydrogen bonds with the CNCs resulting in low ITR. Moreover, the PVA fills the voids between the CNCs, which would otherwise be air, and form a continuous thermal network. As in percolation theory, the PVA solid loading should reach an optimum percentage to form a homogeneous network structure to provide improved $\kappa_{\text{in-plane}}$ [161]. The data indicated that the PVA loading was dependent on its molecular weight and the CNC organization.

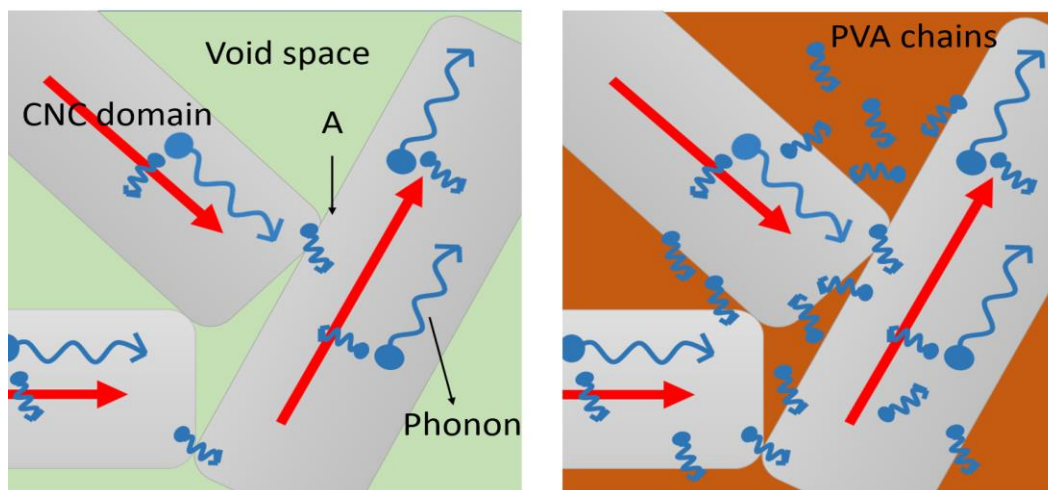


Figure 3-4: Effect of PVA for reducing the interfacial resistance between CNC domains. Here, point A is showed for the interfacial contact position where phonon can diffuse from one crystal to another crystal. (red arrow sign is denoted for the sum of every phonon vector projection in the chain direction of the individual crystalline domain).

3.4.2 Effect of anisotropy for different CNC: PVA composition:

Each CNC transmits the thermal energy differently in each (longitudinal and transverse) direction relative to its primary axis due to the anisotropy of the crystalline directions. This suggests that the $\kappa_{\text{in-plane}}$ of the bulk CNC film should depend on the CNC crystalline organization and hence be anisotropic in films with anisotropic organization/orientation. As expected, there was a significant improvement in $\kappa_{\text{in-plane}}$ for an anisotropic configuration (CNC loading higher than 50 wt%) as shown in **Figure 3-5**. Along the directions of alignment, higher $\kappa_{\text{in-plane}}$ was observed for the CNC-PVA composite films with anisotropic configurations compared to the corresponding isotropic configurations and was highly dependent on the degree of ordering (the order parameter S). Sample with an anisotropic configuration of CNC: PVA (75:25) composition demonstrated ~ 2.5 times improvement in $\kappa_{\text{in-plane}}$ along the shear direction compared to films with an isotropic configuration with the same composition. An exceptionally high

$\kappa_{\text{in-plane}}$ of $\sim 3.45 \pm 0.66 \text{ W m}^{-1} \text{ K}^{-1}$ was observed for this sample due to maximum orientation.

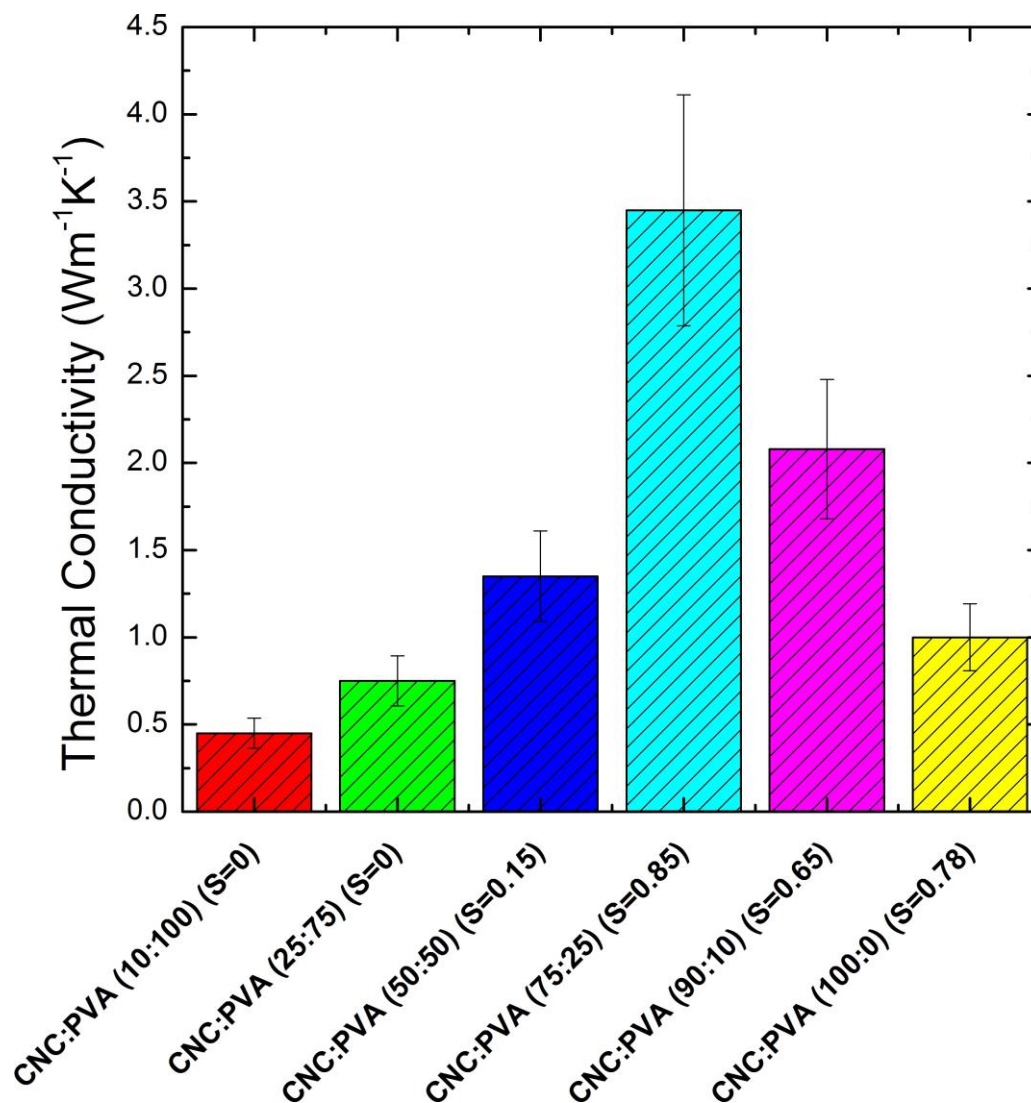


Figure 3-5: Measured $\kappa_{\text{in-plane}}$ in the direction of shear of CNC-PVA composites with various degrees of orientation. S is Hermann's order parameter for CNC-PVA composite system.

Figure 3-6 shows the CNC-PVA composite sample with individual CNCs aligned uniaxially (along the shear direction) which allows phonon propagation down the highest $\kappa_{\text{in-plane}}$ direction of the CNC. In addition, such aligning allows more interfacial contact

between the CNCs leading to higher phonons transport across the interface. Like the case of the isotropic sample, the use of PVA reduces the ITR between the two CNCs by filling the void space and forming strong hydrogen bonds with CNCs. As mentioned above, the PVA percentage should have an optimum percentage with CNC (based on percolation theory) that can act as the binder for CNC domains.

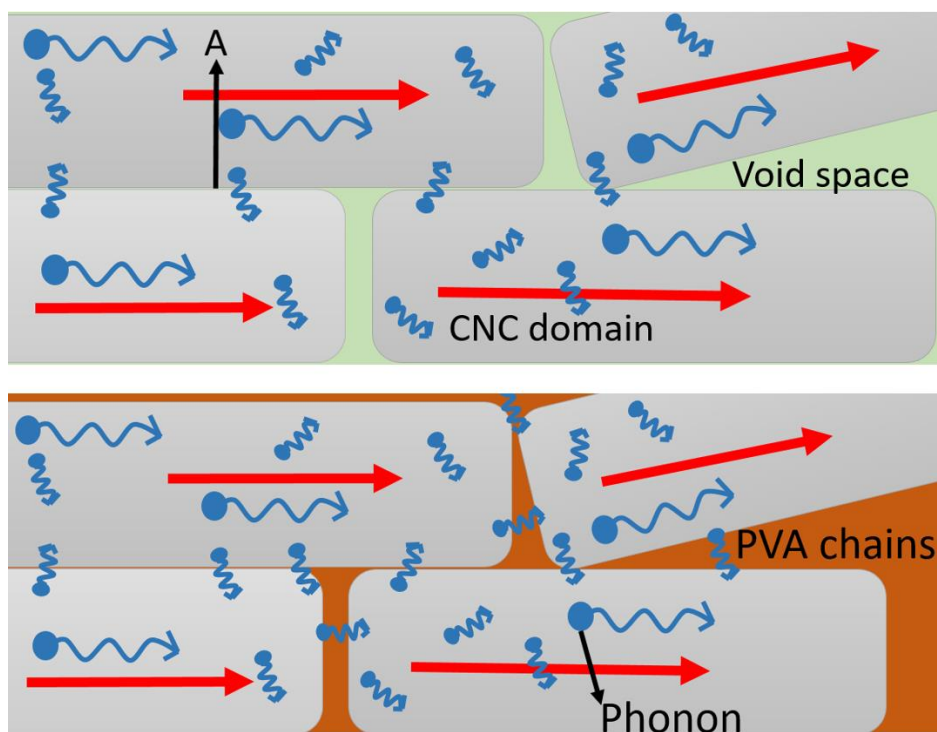


Figure 3-6: Effect of PVA for reducing the interfacial resistance between CNCs for anisotropic composites. Here, point A is shown for the interfacial contact position where phonons can diffuse from one crystal to another crystal. (red arrow sign is denoted for the sum of every phonon vector projection in the chain direction of the individual crystalline domain).

The values of κ reported in this work was much higher than the traditionally used electrically insulating polymers and associated nanocomposite systems. A comparative data with different polymer systems have been shown in **Table 3-1**.

Table 3-1: Thermal conductivity for different polymer/polymer nanocomposite systems.

Sample	Matrix (wt%)	Filler (wt%)	S	$\kappa_{in-plane}$	References
PPS-BN	PPS-(70)	BN-(30)	----- -	0.62	[162]
Epoxy-graphite	Epoxy-(76)	Graphite-(24)	----- -	1.8	[163]
Epoxy-CNF	Epoxy	CNF	----- -	0.35	[163]
HDPE-Al	HDPE-(80)	Al- (20)	----- -	0.7-1.25	[106]
Common engineering thermoplastic	Polymer as matrix	No filler	----- -	0.11-0.53	[106]
PMMA-CNT	PMMA-(96)	CNT- (4)	-----	3.4	[164]
Acrylic resin-NC	Acrylic resin	NC	-----	2.5	[144]
TNW	TNW	-----	-----	2.5	[143]
PI	PI	-----	-----	0.91	[143]
PET	PET	-----	-----	0.87	[143]
COP	COP	-----	-----	0.70	[143]
PPS	PPS	-----	-----	0.63	[143]
PA	PA	-----	-----	0.25	[143]
PES	PES	-----	-----	0.25	[143]
CNC-PVA	CNC	PVA	0	1.4 (maximum)	This work
CNC-PVA	PVA	CNC	0	0.7 (maximum)	This work
CNC-PVA	CNC	PVA	0.85-0.65	3.5 (maximum)	This work

PPS = Polyphenylene sulfide; HDPE = High-density polyethylene; PMMA= Poly (methyl methacrylate); COP = Cyclo-olefin polymer; PA = Polyamide; PES = Polyethesulfone

3.4.3 Effective Medium Theory – Choy & Young (EMT-CY) Model applied to CNC-PVA composite thin films:

For any polymer nanocomposite system, the overall thermal transport depends on the ITR between the fillers and between the filler and matrix. In addition, anisotropy plays a significant role for structured materials as is the case in this work. A variety of models

are available to describe complex nanostructured materials [165], polycrystalline structures [166], and composites [167] where the interfaces and the organization of the materials are factors that dominate the thermal properties. Choy and Young [168] developed a model with an adaptation of Maxwell's effective medium theory (EMT) [169] (denoted EMT-CY here), which has been previously applied to study the change in the κ of oriented semi-crystalline polymers [170]–[172] both along and normal to the orientation direction as a function of the orientation direction crystallinity.

The expressions derived from the EMT-CY model for the CNC-PVA nanocomposites are [168]:

$$\frac{\kappa_c - \kappa_m}{\kappa_c + 2\kappa_m} = x \left[\frac{2}{3} \left(\frac{\lambda_{\perp} - 1}{\lambda_{\perp} + 2} \right) + \frac{1}{3} \left(\frac{\lambda_{\parallel} - 1}{\lambda_{\parallel} + 2} \right) \right] \quad \text{Eq. 3-1}$$

$$\frac{\kappa_{\perp} - \kappa_m}{\kappa_{\perp} + 2\kappa_m} = x \left[\left(\frac{\lambda_{\perp} - 1}{\lambda_{\perp} + 2} \right) \left(\frac{1 + \langle \cos^2 \gamma \rangle}{2} \right) + \left(\frac{\lambda_{\parallel} - 1}{\lambda_{\parallel} + 2} \right) \frac{\langle \sin^2 \gamma \rangle}{2} \right] \quad \text{Eq. 3-2}$$

$$\frac{\kappa_{\parallel} - \kappa_m}{\kappa_{\parallel} + 2\kappa_m} = x \left[\left(\frac{\lambda_{\perp} - 1}{\lambda_{\perp} + 2} \right) \langle \sin^2 \gamma \rangle + \left(\frac{\lambda_{\parallel} - 1}{\lambda_{\parallel} + 2} \right) \langle \cos^2 \gamma \rangle \right] \quad \text{Eq. 3-3}$$

$$\lambda_{\parallel} = \frac{\kappa_{c\parallel}}{\kappa_m} \quad \text{Eq. 3-4}$$

$$\lambda_{\perp} = \frac{\kappa_{c\perp}}{\kappa_m} \quad \text{Eq. 3-5}$$

$$\mathbf{S} = \frac{3\langle \cos^2 \gamma \rangle - 1}{2} \quad \text{Eq. 3-6}$$

where x is the weight fraction of the CNC, which was approximately 0.75 for the samples under study [108], and κ_c is the κ of an isotropic film which was approximated as $1.22 \text{ W m}^{-1} \text{ K}^{-1}$ from the measurement results presented previously in this work. The effective matrix thermal conductivity κ_m is obtained by solving **Eq. 3-1**, **Eq. 3-4** and **Eq. 3-5**, simultaneously. **Eq. 3-2** and **Eq. 3-3** are used to calculate the macroscopic κ of the CNC-PVA composite films in the directions parallel (κ_{\parallel}) and perpendicular (κ_{\perp}) to the shear direction. The orientation angle of the crystals with respect to the shear direction is represented by γ , while $\kappa_{c\parallel}$ and $\kappa_{c\perp}$ represent the thermal conductivities of a single CNC in the axial and the transverse crystalline directions respectively and their corresponding values were predicted to be $\sim 5.7 \text{ W m}^{-1} \text{ K}^{-1}$ and $\sim 0.72 \text{ W m}^{-1} \text{ K}^{-1}$ by Diaz *et al.* [108].

The experimentally obtained values of $\kappa_{\text{in-plane}}$ of the anisotropic CNC-PVA composite films are shown in **Figure 3-7** along with those predicted by the EMT-CY model in the directions parallel (κ_{\parallel}) and perpendicular (κ_{\perp}) to the shear direction. The $\kappa_{\text{in-plane}}$ of an isotropic film predicted by this model was $\sim 1.27 \text{ W m}^{-1} \text{ K}^{-1}$ that was close to that of the experimental value ($\sim 1.22 \text{ W m}^{-1} \text{ K}^{-1}$). Further, the upper bound and lower bound values of κ_m predicted by the model were $\sim 1.23 \text{ W m}^{-1} \text{ K}^{-1}$ and $\sim 0.46 \text{ W m}^{-1} \text{ K}^{-1}$, respectively. The lower end of this range was comparable to the upper end of the experimentally obtained κ value of neat PVA, specifically $\sim 0.08 \text{ W m}^{-1} \text{ K}^{-1}$ to $\sim 0.41 \text{ W m}^{-1} \text{ K}^{-1}$ for initial PVA weight % of 1% to 10.7% indicating that other contributions to ITR such as CNC-CNC or CNC-matrix interfaces were relatively small in comparison. Compared to the effective κ_m value of $0.022 \text{ W m}^{-1} \text{ K}^{-1}$ obtained in the previous work on CNC-only films [108], the values of κ_m obtained in this work were significantly larger. These results suggested that the use of PVA interstitial secondary material can have a significant

positive influence on the effective κ of CNC-based films by removing the highly resistive free volume and nanoscopic voids.

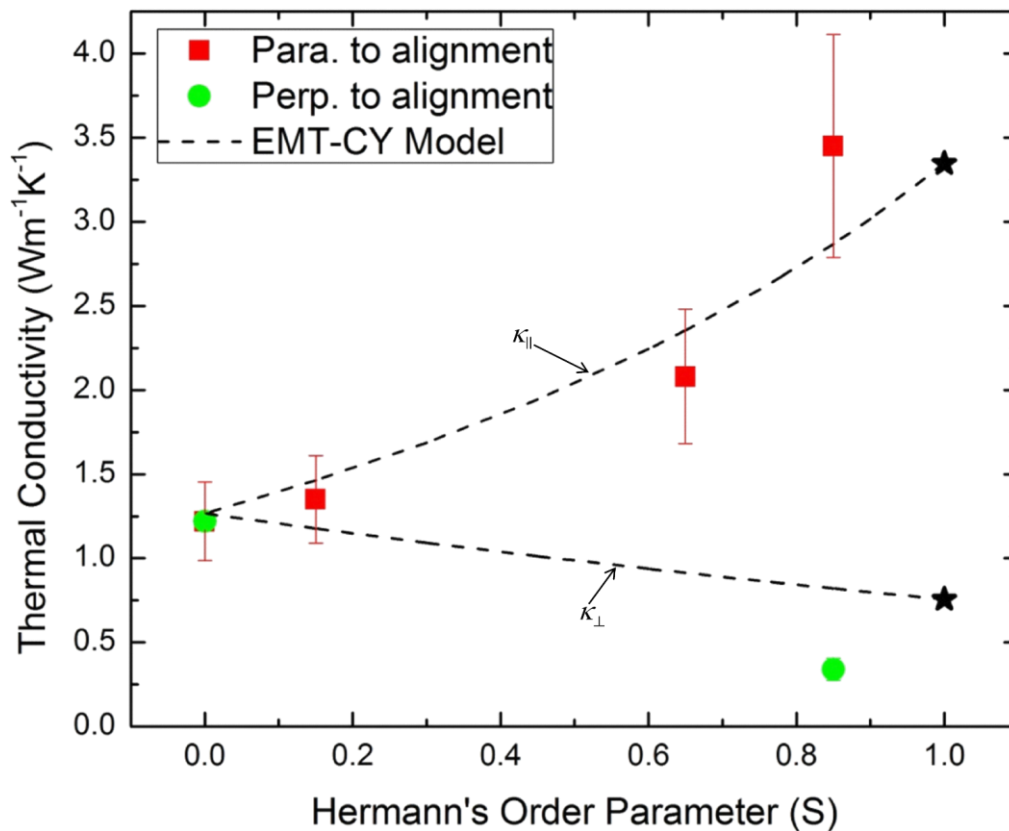


Figure 3-7: Experimental κ of anisotropic CNC-PVA composite films shown along with results from the EMT-CY model as a function of S . The weight % of CNC is not in particular order. The stars represent the extrapolated values of κ obtained from the EMT-CY model at $S \approx 1$.

As shown in **Table 3-1**, the $\kappa_{\text{in-plane}}$ of the best performing CNC-PVA composite film developed in this work was ~ 4 - 14 times higher than that of other plastic films that are currently used for transparent, flexible devices indicating the potential of the CNC-PVA composite films an application for thermal management of flexible electronic devices. Compared to other Cellulose-based materials, the results obtained here were ~ 1.4 fold higher than that of the TNW sheet developed by Uetani *et al.* [143]. However, the work

presented in this chapter was significantly different than that of Uetani *et al.* In their work, TNWs showed the best results that were significantly longer (microns) than the wood-based CNCs studied here (100 nm) [173]. As Diaz *et al.* observed, the long axis has a much higher $\kappa_{\text{in-plane}}$ than either orthogonal direction; therefore, the isotropic TNW materials should show much higher $\kappa_{\text{in-plane}}$ than the isotropic wood-based CNCs here, which is shown by the results of this work. Compared to the work by Diaz *et al.*, the TNW materials showed high effective ITR and low sound velocity which was at least partially due to small pores in the structure as stated by Uetani *et al.* Therefore, the increase in $\kappa_{\text{in-plane}}$ with a decrease in ITR would be expected because of the filling of the free volume/small pores with a strongly bonded solid material.

A strong correlation with nanocrystal width was also observed by Uetani *et al.*, with TNW showing the highest $\kappa_{\text{in-plane}}$, as it was the widest material. The isotropic random configuration of CNC or TNW would be expected to have a large percentage of crossed crystal contact-points. All the heat transport takes place through the contact-points and contact-points have less contact area than the axial contact along the width. Therefore, the effective ITR for the isotropic configurations would be expected to be higher than anisotropic axial configurations because of the higher amount of cross-points relative to parallel axial contacts and, hence, there would be less overall contact area to transport heat in the isotropic configuration. We obtained a high $\kappa_{\text{in-plane}}$ for anisotropic CNC-PVA composite films, and even a higher value would be obtained for aligned composite structures of longer materials like TNWs.

To demonstrate the potential of the CNC-PVA composite films developed through this work for dissipating a significant amount of heat from electronics-like concentrate heat

sources, thermal images were taken from a 100% PVA sample and a CNC-PVA (90:10) sample as shown in **Figure 3-8**. Same Joule heating powers (175 mW) were induced via DC power supply to the identical serpentine Au heaters that were shadow-evaporated on the surface of each of these samples. The thermal images taken with almost identical temperature scales showed significantly lower (~ 7 °C) maximum temperature of the resulting hot spot for the CNC: PVA composite sample than that of the neat PVA sample. The slight asymmetries seen in the images were due to the DC power being applied across the top left and bottom right contact pads of both samples.

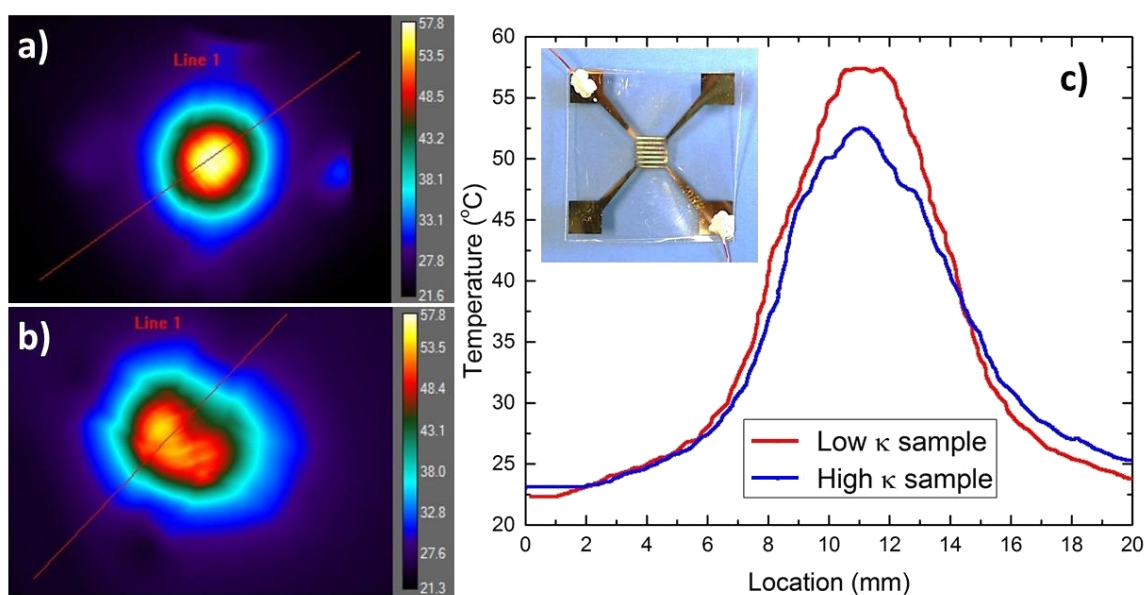


Figure 3-8: Thermal images of CNC-PVA composites a) 100% PVA sample with low κ , and b) 90:10 CNC: PVA sample with high κ during Joule heating of a serpentine metallic heater simulating flexible electronics elements. c) Line scans along the centerline of a) and b) quantify the temperature reduction associated with the high κ sample at the same Joule heating power (175 mW). Inset: Photograph of 90:10 CNC: PVA sample with a shadow-evaporated metallic heater.

3.5 Conclusion

In this work, thermal properties of the CNC-PVA composite films with isotropic and anisotropic configurations were investigated. The isotropic CNC-PVA composite films with PVA solid loading of 10-50 wt% showed significant improvement on $\kappa_{\text{in-plane}}$ than that of the one component system. Furthermore, the anisotropic CNC-PVA composite films showed $\kappa_{\text{in-plane}}$ as high as $\sim 3.45 \text{ W m}^{-1} \text{ K}^{-1}$ in the shear direction which was a ~ 2.5 fold improvement over the CNC-PVA composite films with the isotropic configuration. The reason for such improvements was due to the role of PVA as an excellent void filling agent leading to the formation of conductive paths for phonon transport with reduced interfacial resistance and the orientation of CNCs towards heat flow direction in anisotropic films. More importantly, our CNC-PVA composite films showed ~ 4 -14 fold higher $\kappa_{\text{in-plane}}$ than that of the commonly used plastic films for flexible electronic devices and also demonstrated better heat spreading capability from a localized hot spot as would be experienced by a flexible electronics element. The results obtained through this work suggest that the CNC-PVA composite films can be a good candidate for substrates for potential application in the thermal management of flexible electronics and can also be an eco-friendly and sustainable alternative to the petroleum-based polymeric materials.

CHAPTER 4

THERMAL CHARACTERIZATION OF ULTRANANOCRYSTALLINE NANODIAMOND FILMS

4.1 Introduction and Motivation

There is a need for efficient heat spreading materials in electronic devices to control the increasing power density and minimize the negative impacts of hot spots as mentioned in CHAPTER 1 of this dissertation. One better solution is to incorporate materials with high κ to take the undesired heat away from sensitive devices since κ of a heat spreader material indicates the ease of thermal transport. One of the approaches would be the use of thin films. For thin films, the κ changes according to their thickness that can vary between fractions of a nanometer to several micrometers. The κ of thin films play an essential role in determining the performance, reliability and overall design of microelectronic devices, micromachined transistors, photonic devices, and thermoelectric devices; therefore, there has been growing interest in the study of this parameter [174], [175]. There are different kinds of thin films including metallic, insulating and semiconducting. Metal thin films are commonly used in microelectronic and photonic devices. Thermal transport by electrons is dominant in metal thin films. Also, size effects on κ can be observed due to the resistance on the electron transport introduced by the scattering of electrons at the thin film boundaries [176], [177]. For non-metallic films, free electrons are not available in enough numbers to contribute significantly to thermal transport; hence, phonons are typically the

dominant contributor to thermal conduction in diamond and other electrically insulating/semiconducting materials. Dielectric thin films are used as electrical insulators, optical coatings, and thermal barriers for applications such as microelectronic and optical devices. In the case of semiconductors, the contribution of electrons for thermal transport is very small depending on the doping concentration. Si thin films exist in the forms of single crystalline, polycrystalline, and amorphous states with potential applications in silicon-on-insulator (SOI), ICs sensors, and actuators [174], [175].

A wide variety of carbon-based materials such as diamond, polycrystalline diamond (PCD), diamond-like carbon (DLC), CNTs, and single-layer graphene, have attracted great attention for potential applications in electronic devices [178]–[180]. They have a wide range of κ that vary from as low as $0.1 \text{ W m}^{-1} \text{ K}^{-1}$ in DLC [181] to as high as $5000 \text{ W m}^{-1} \text{ K}^{-1}$ in single-layer graphene [182], [183]. Thermal transport is governed by lattice vibrations in such materials, and it depends on the structural disorder, sp^2 or sp^3 content of the material, and thickness grain size of the films [184]. High-quality bulk diamond has a very high room temperature κ that exceeds the κ of other materials used for interconnects such as aluminum, copper, and silver [185].

Other unique properties include low coefficient of thermal expansion (CTE) ($1 \times 10^{-6} \text{ K}^{-1}$) [186], low density, extreme hardness, chemical inertness, high mobility of charge carriers, high electrical resistance, wide optical transparency, and biocompatibility [178], [187], [180]. Due to such exceptional properties, they have been used for wear-resistive coatings, optical windows, surface acoustic-wave devices, and field-emission flat panel displays [178], [179], [188], [189]. Despite such excellent properties, natural single-crystal diamonds are not feasible for many applications. In order to use diamonds for a variety of

applications, they are synthesized as polycrystalline ND films [190]. Most of the existing thermal conduction studies are focused on polycrystalline films instead of single-crystal diamonds due to several reasons.

First, they have higher carrier mobility. It is also very difficult to dope the single-crystal diamonds with impurities to make them semiconducting [191]. Furthermore, they can only be efficiently deposited on polished diamond substrates, whereas polycrystalline diamond films can be deposited on non-diamond substrates such as Si, thus creating opportunities for integrated Si-diamond technology for electronic devices [192]. There are different methods of synthesis of diamond films such as chemical vapor deposition (CVD), high-pressure high-temperature (HPHT), the detonation of explosives, laser ablation, and graphite etching. Among the diamond films obtained through various techniques, the polycrystalline diamond films synthesized through CVD route show superior properties in terms of κ , CTE, mechanical strength, and electrical resistivity. They are even better than other traditional electronics packaging materials [193], [194].

Moreover, such films can still inherit the exceptional properties of single-crystal diamonds such as the resistance to wear, chemical inertness, and biocompatibility. However, CVD growth methods can be costly, may not integrate well with all microfabrication processes, and still show serious performance degradation compared to single crystalline diamond in terms of thermal transport. Alternatively, thin films comprised of diamond nanoparticle aggregates may be able to achieve comparable performance to CVD films but at a fraction of the cost.

According to the size of the crystal domains, polycrystalline ND films can be categorized as ultrananocrystalline diamond (UNCD) (grain size $d < 10$ nm),

nanocrystalline diamond (NCD) ($d \sim 10\text{-}1000$ nm), microcrystalline diamond (MCD) ($d > 1$ μm). It is easier to manipulate the properties of the ND films due to their smaller size, larger surface area, and reproducible synthesis. UNCD films on Si substrate are much smoother and pinhole-free compared to faceted MCD film; hence, they are considered to be suitable for thermal management of MEMS, nanoelectromechanical system (NEMS), and microelectronics [63], [195].

The heat conduction properties of synthetic polycrystalline films are not as advantageous as those of single-crystal diamonds. The κ of single crystalline and polycrystalline thin films are significantly lower than their bulk counterparts because of the phonon and electron scatterings at the grain boundaries and interfaces [196]–[198]. The κ of high-quality single-crystal diamond is ~ 2200 $\text{W m}^{-1} \text{K}^{-1}$ [185] at 300 K. However, the thermal properties of ND films depend on various factors such as d , film thickness, lattice imperfection and impurities, and interface quality [199], [200]. Therefore, the room-temperature κ of MCD ~ 550 $\text{W m}^{-1} \text{K}^{-1}$ [63] while that of UNCD films prepared by CVD method is $\sim 8.6\text{-}16.6$ $\text{W m}^{-1} \text{K}^{-1}$, much smaller than that of Si (~ 140 $\text{W m}^{-1} \text{K}^{-1}$) [63]. For UNCD and MCD, the essential parameters such as d and grain boundaries can be controlled by varying the processing conditions to make them more thermally conductive. This indicates that they can be very important in the thermal engineering of electronics devices [199], [200]. Goyal *et al.* [201] demonstrated the application of composites of Si-synthetic diamond (Si-Di) substrates as an alternative to conventional Si for thermal management of complementary metal-oxide semiconductor (CMOS) technology. For the Si-Di composite formed by UNCD or MCD films synthesized on Si substrate, the thermal resistance is greatly reduced at temperatures close to the operating temperature (~ 380 K) of the

electronic chips [202]. This is significantly lower than the hot spot temperatures in current advanced chips, indicating improved thermal management relative to conventional practices [201].

Due to exceptional electronic, optical, mechanical, chemical, and thermal properties, polycrystalline ND films have many potential applications in electronics [192], optoelectronics [203], [204], MEMS [205], [206], and wear resistant coatings [207]. They are considered to be very suitable for heat spreader application because of a unique combination of a very high room temperature κ , a low CTE, and a low density [190]. However, in most applications, the ND films are directly grown on the substrates and further patterning steps are performed on it. This greatly prohibits its use in many applications since the common growth methods mentioned above use high temperatures (> 400 °C), vacuum or low pressures, and other specific conditions [208], [209]. This indicates that it would also be very difficult to deposit ND films on plastic substrates that cannot handle such higher temperatures, thus limiting the application of ND films for flexible electronics.

To demonstrate the solution of such issues, Kim *et al.* [210] transferred microstructures of thin films of UNCD (referred as μs -UNCD) synthesized by hot-filament CVD method to various target substrates including glass, GaAs, Si, PDMS and PET using a printing technique. The UNCD films on PDMS and PET were mechanically bendable and even stretchable, indicating potential applications for flexible devices. Therefore, they also demonstrated the application of μs -UNCD as heat spreaders for thermal management of flexible electronics. For this purpose, thin film microheaters (in serpentine patterns) of Ti/Au were formed on PET substrates and the same amount of electrical power was

applied. Then the behaviors of three different structures were compared: one with microheaters exposed to air, one with a uniform coating of a thin layer of poly(methylmethacrylate) (PMMA), and the third one with a printed platelet of μs -UNCD. The PET and PMMA layers were damaged by the generated heat, but the μs -UNCD sample exhibited very robust behavior, thus indicating its capability as a heat spreader.

Given the integration and cost challenges faced by CVD-grown diamond thin films, there is a significant opportunity for ND-based films to represent a more viable option for widescale adoption if their thermal transport performance can be shown to be competitive. Therefore, the thermal properties of ND films deposited on Si substrates through a solution-based directed covalent assembly of NDs are presented in this work. Such films can be a less expensive and greener alternative to CVD diamond films. Therefore, this may create opportunities for a new class of low-cost diamond films that are compatible with a wide variety of substrates commonly used for electronics, optics, biosensors, and MEMS where the applications of CVD diamond films have been limited.

More study needs to be done in the integration capabilities of the covalently assembled ND films, in terms of thermal properties and thickness range for MEMS applications. It is expected that the properties of ND films including porosity, κ , and mechanical robustness will greatly depend on the synthesis method. Since there has not been any previous work on the synthesis and thermal characterization of the ND films obtained through directed covalent assembly approach, it is essential to study the mechanisms and physics related to thermal transport of such films.

4.2 Research Objectives

In this work, the thermal transport characterization of ND films synthesized through the directed covalent assembly approach was experimentally investigated for potential thermal management applications in MEMS/electronic devices. To achieve this goal, the following specific objectives were to be achieved through this research:

- Study the thickness and temperature dependence of the $\kappa_{cross-plane}$ of the covalently assembled ND films.
- Correlate the observed κ values with film micro/nanostructure.

Microfabricated devices were used to measure the cross-plane κ of the covalently assembled ND films. The cross-plane κ ($\kappa_{cross-plane}$) was determined by the well-known 3ω method [211]. To study the effect of the film thickness on κ , ND films of different thicknesses were used. For each film sample, the measurements were performed between 125 K and 425 K to study the temperature-dependence of the thermal properties which is very important for understanding the dominant scattering mechanisms limiting κ in ND films.

4.3 Experimental Materials and Methods

4.3.1 ND film Samples

Multiple samples of covalently assembled ND films were supplied by Dr. Adarsh Radadia's group at Louisiana Tech University. To study the effect of the ND film thickness on the $\kappa_{cross-plane}$, the samples had approximately the same particle size ($d \sim 5-10$ nm form larger aggregates of ~ 50 nm) but different thicknesses, with each sample film being synthesized via a differing number of repeated deposition cycles performed by the Radadia group.

4.3.2 3 ω Method

The experimental method used for the measurement of $\kappa_{cross-plane}$ is described in this section. The κ measurement methods used in the previous chapters are suitable for the thicker samples (thickness on the orders greater than microns). However, the ND films studied in this work had smaller thicknesses (on the order of hundreds of nanometers). There are different techniques for the measurement of the κ of thin films. Each technique has its own advantages and limitations; therefore, the choice of a measurement technique depends on the nature of the thin film. The well-established 3 ω method is one of the popular methods for the measurement of the $\kappa_{cross-plane}$ of thin films. This method is based on AC heating approach; hence, the time required to reach equilibrium state is much lower (few minutes) than that of the conventional techniques that take a longer time (can take many hours). This method was initially developed by Cahill and coworkers to measure the κ of the bulk samples in 1989 [211], [212]. Later, Cahill *et al.* [213] extended this technique for the measurement of the $\kappa_{cross-plane}$ of thin films as small as a few nanometers.

A typical implementation of 3 ω method for a bulk sample is shown in **Figure 4-1**.

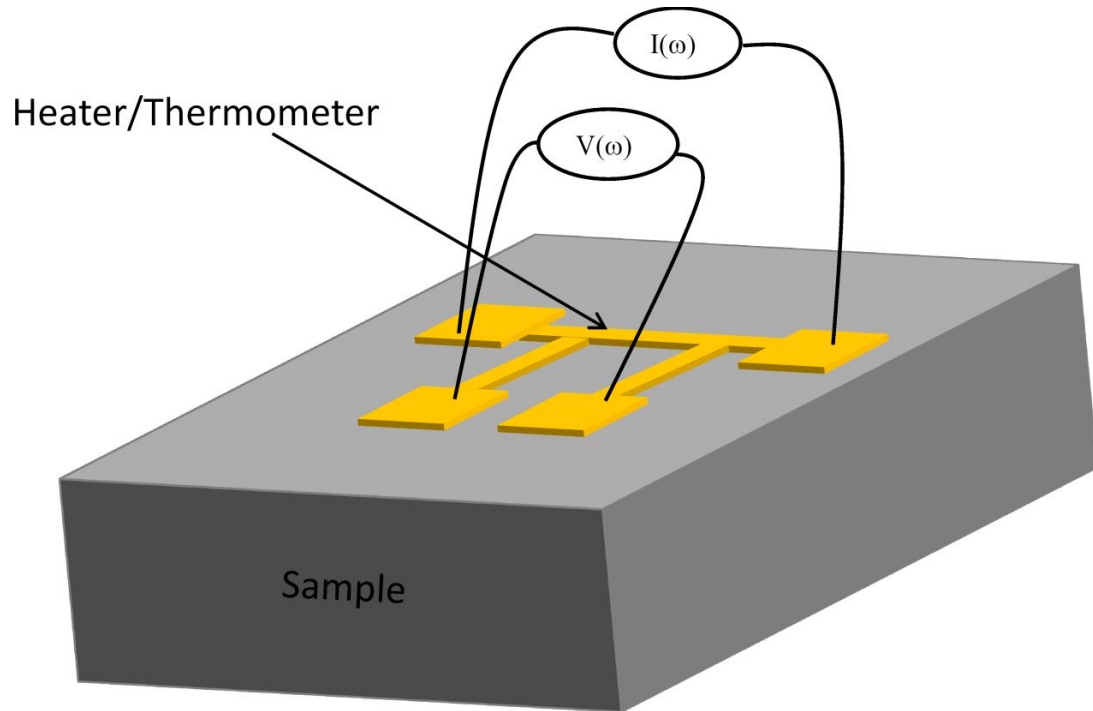


Figure 4-1: Schematic diagram of a bulk sample with a 3ω metal line patterned on the top of it. Adapted from Ref. [214]. Not to scale.

In this method, a narrow metal line is deposited onto the surface of the sample using standard photolithography techniques. This line is used both as an electrical resistance heater as well as a temperature sensor. For an electrically conductive sample, the current leakage will affect the measurement. For such cases, a thin insulating layer should be deposited on the surface of the sample before depositing the metal in order to prevent any current leakage through the sample. A driving current I with angular frequency ω applied to the metal line causes Joule heating I^2R , where R is the resistance of the metal line, at 2ω . This heating results in the temperature oscillation of the metal line at 2ω . For pure metals, the resistance increases with increasing temperature so the resistance of the metal line also oscillates at 2ω and creates a small voltage oscillation at 3ω when multiplied by the driving current at ω as given by [215]:

$$V_{3\omega} = \frac{1}{2} I_o R_o \Delta T \left(\frac{1}{R} \frac{dR}{dT} \right) \quad \text{Eq. 4-1}$$

$$\Delta T = 2R \frac{V_{3\omega}}{V_o} \left(\frac{dT}{dR} \right) \quad \text{Eq. 4-2}$$

where $V_{3\omega}$ is the 3ω component of the voltage, I_o and R_o are the dc components of the current and resistance, respectively, $V_o = I_o R_o$ is the first harmonic voltage drop across the line, ΔT is the temperature rise of the metal line, and $\frac{dR}{dT}$ is the change in resistance of the metal line with the temperature.

The exact solution for the amplitude of the temperature oscillations at a distance “ r ” from a line source of heat is given by [216]:

$$\Delta T = \frac{P}{\pi l \kappa} K_o(qr) \quad \text{Eq. 4-3}$$

where P is the amplitude of the power dissipated by the line at a frequency ω , l is the length of the line, and K_o is the zeroth-order modified Bessel function and q is the root of $K_o(qr) = 0$. The expression in **Eq. 4-2** is valid for an infinitely narrow line source of heat on the surface of a semi-infinite sample. If the width of the line is small compared to the thermal penetration depth (TPD), the line can be considered to be infinitely narrow. Also, the sample can be approximated as semi-infinite if the TPD is significantly smaller than the size of the sample. The TPD is the distance heat diffuses during one cycle of heating. It can be defined as the magnitude of the complex quantity $\frac{1}{q}$ [212]:

$$\frac{1}{q} = \left(\frac{\alpha}{i2\omega} \right)^{\frac{1}{2}} \quad \text{Eq. 4-4}$$

where α is the thermal diffusivity of the sample.

In the limit $|qr| \ll 1$, **Eq. 4-3** can be approximated as [211]:

$$\Delta T = \frac{P}{\pi l \kappa} \left(\frac{1}{2} \ln \frac{\alpha}{r^2} + \ln 2 - 0.5772 - \frac{1}{2} \ln(2\omega) - \frac{i\pi}{4} \right) \quad \text{Eq. 4-5}$$

The expression in **Eq. 4-5** has been presented in such way to show the contributions of the frequency dependent and imaginary components to the solution. If the frequency dependent component of the temperature rise of **Eq. 4-5** is used for two different heating frequencies, the κ of the sample can be determined by [211]:

$$\kappa = \frac{V_o^3 \ln \frac{\omega_2}{\omega_1}}{4\pi l R^2 (V_{3\omega,1} - V_{3\omega,2})} \left(\frac{dT}{dR} \right) \quad \text{Eq. 4-6}$$

where R is the average resistance of the metal line, $V_{3\omega,1}$ and $V_{3\omega,2}$ are the third harmonics in-phase voltage drops across the line at frequencies of ω_1 and ω_2 , respectively. The term $\left(\frac{(V_{3\omega,1} - V_{3\omega,2})}{\ln \frac{\omega_2}{\omega_1}} \right)$ represents the slope of the line connecting two points in the semi-log plot.

To get a more reliable result, data is typically taken over a range of frequencies and the slope of the best-fit line is used.

There is an important condition for the 3ω method explained above which is related to the TPD. The thickness of the sample must be larger than the TPD. The TPD depends on frequency as expressed in **Eq. 4-4**. However, there is a finite upper limit on the frequency of the metal line where the capacitance of the metal line cannot be neglected [214]. Due to this limitation, it is very difficult to accurately measure the κ of the films thinner than approximately 10-20 μm (depending on their α values) using the traditional 3ω method explained above. In order to overcome this limitation, Cahill *et al.* [213] extended the 3ω method to allow for $\kappa_{\text{cross-plane}}$ measurements on films as thin as tens of nanometers. The experimental setup for this modified technique is shown in **Figure 4-2**.

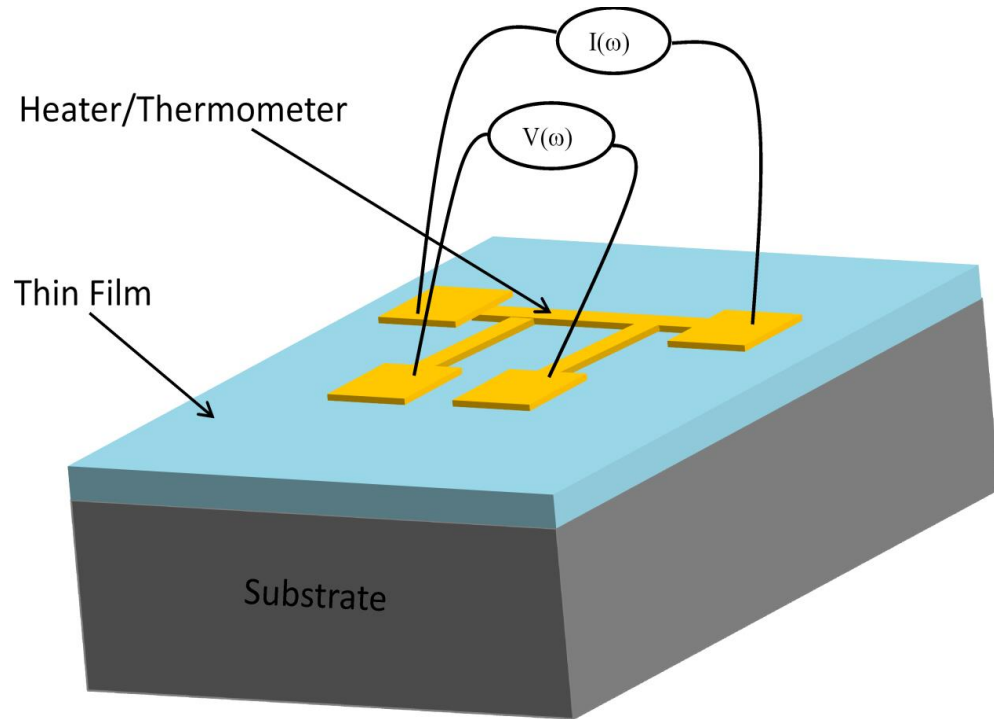


Figure 4-2: Schematic diagram of a thin film sample on the top of a substrate with a 3ω metal line patterned on the top of it. Adapted from the Ref. [214]. Not to scale.

The width of the metal line should be larger than the thickness of the film so that the heat flow through the film can be modeled as one dimensional with negligible error. Since the film present on the surface of the substrate is very thin (film thickness is much less than the TPD), it adds a frequency independent temperature rise (ΔT_{film}) to the temperature rise of the substrate ($\Delta T_{substrate}$). The measured temperature rise of the metal line ΔT_{total} is the sum of the temperature rise of the film and the temperature rise of the substrate. Hence, the temperature rise of the film can be determined by [214]:

$$\Delta T_{film} = \Delta T_{total} - \Delta T_{substrate}$$

Eq. 4-7

For an electrically insulating substrate, the value of $\Delta T_{substrate}$ can be directly obtained for a separate bare substrate by using standard 3ω method and **Eq. 4-5**. However, in the case of an electrically conducting substrate, it can be calculated using [217]:

$$\Delta T_{substrate} = \frac{P}{\pi l \kappa_{substrate}} \left(\frac{1}{2} \ln \left(\frac{\kappa_{substrate}}{C_{substrate} \left(\frac{w}{2}\right)^2} \right) + 0.923 - \frac{1}{2} \ln(2\omega) \right) \quad \text{Eq. 4-8}$$

where $C_{substrate}$ is the specific heat per unit volume of the substrate, w is the width of the metal line and $\kappa_{substrate}$ is the thermal conductivity of the substrate. After measuring the total temperature rise as well as determining the temperature rise of the substrate, the κ of the film can be determined by using [214]:

$$\kappa_{film} = \frac{Pt}{\Delta T_{film} wl} \quad \text{Eq. 4-9}$$

where t is the thickness of the film.

The κ obtained from this method includes the thermal boundary resistance between the substrate and the film as well as the thermal boundary resistance between the film and the metal line. Therefore, κ_{film} is also referred to as an “apparent” or “effective” κ . However, for many common semiconductor material combinations (Au-SiO₂, Pt-SiO₂, etc.), data exists on thermal boundary resistance which can be used to compensate. Thus, the thermal boundary resistance between the film and the substrate can be determined by measuring the sample films of varying thickness and extrapolating to the case of zero thickness. If both methods are available, a more accurate value of κ_{film} may be obtained.

4.3.3 Microdevice Fabrication

A photomask was first designed using the LayoutEditor software package for the microdevice fabrication. The microdevice design itself consists of gold (Au) lines of different widths and lengths on a single device for the measurements of both $\kappa_{cross-plane}$ and $\kappa_{in-plane}$ of the thin film sample. Although these microdevices are capable of measuring $\kappa_{in-plane}$, this is not a focal point of this work and will be investigated in follow-up efforts. The microdevices were fabricated using a standard photolithography process at Louisiana Tech University's Institute for Micromanufacturing.

First, an array of microdevices was fabricated on a 100 mm diameter SiO₂-on-Si (200 nm of SiO₂ on 500 μ m of Si substrate) wafer for determining the κ of the SiO₂ film and Si substrate to validate our experimental setup. Then, similar steps were performed on 1 cm by 1 cm Si wafer (thickness of 500 μ m) pieces containing ND films of varying thickness. To begin the fabrication process, the lift-off resist LOR 5B was spin-coated on the wafer. The use of LOR 5B supports a cleaner metal lift-off. Then, a layer of Shipley 1813 photoresist was spun on the top of the wafer followed by UV exposure through a patterned photomask and a subsequent development step in the MF-319 developer. After confirming all the desired features by observing under an optical microscope, a 10 nm-thick chromium (Cr) adhesion layer and a 200 nm-thick Au layer were sequentially deposited using DC magnetron sputtering. After this, metal lift-off was performed by soaking the wafer in Remover PG at 80 °C.

Figure 4-3 shows a final microdevice with the first three Au resistance thermometer (GRT) lines for the measurement of the $\kappa_{in-plane}$ and the fourth thermometer/heater line (GRT/H) for the measurement of the $\kappa_{cross-plane}$.

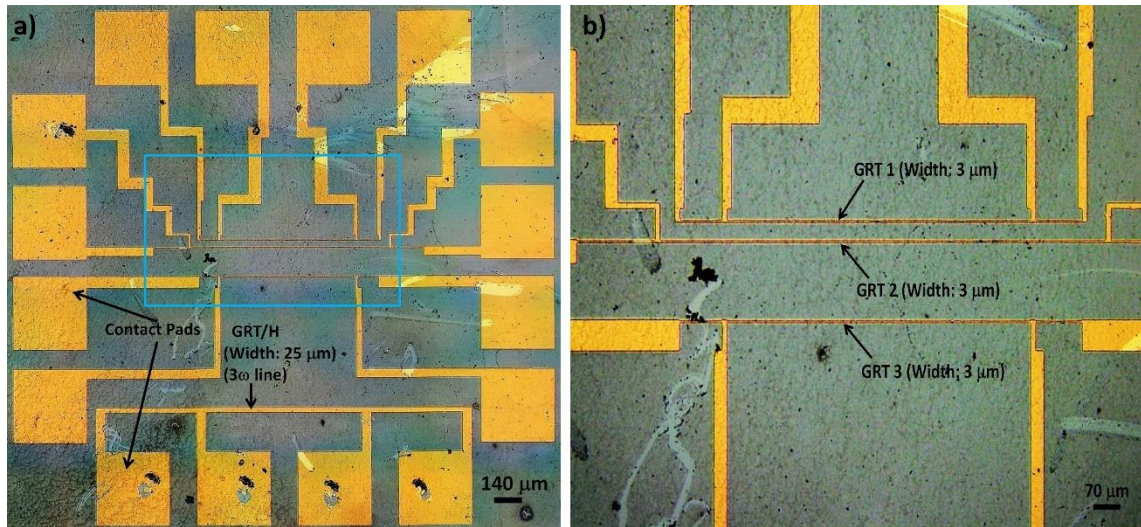


Figure 4-3: a) Light microscope image of a single microdevice showing the Au lines used for the measurement of $\kappa_{cross-plane}$ along with the lines used for the measurement of $\kappa_{in-plane}$ outlined in blue b) Details of the blue boxed region showing all the GRT lines. The Au lines were deposited on the top of ND films. Large square features around the periphery are the contact pads that were used for forming electrical connections to the Au lines and the legs of the chip carrier.

After dicing of the wafer/chip to isolate a viable individual microdevice, the individual microdevice was adhered to a commercially available 16-pin ceramic chip carrier package using silver epoxy and electrical connections to the metal lines were made through a wire-bonding technique. **Figure 4-4** shows a packaged sample before being loaded into the cryostat.

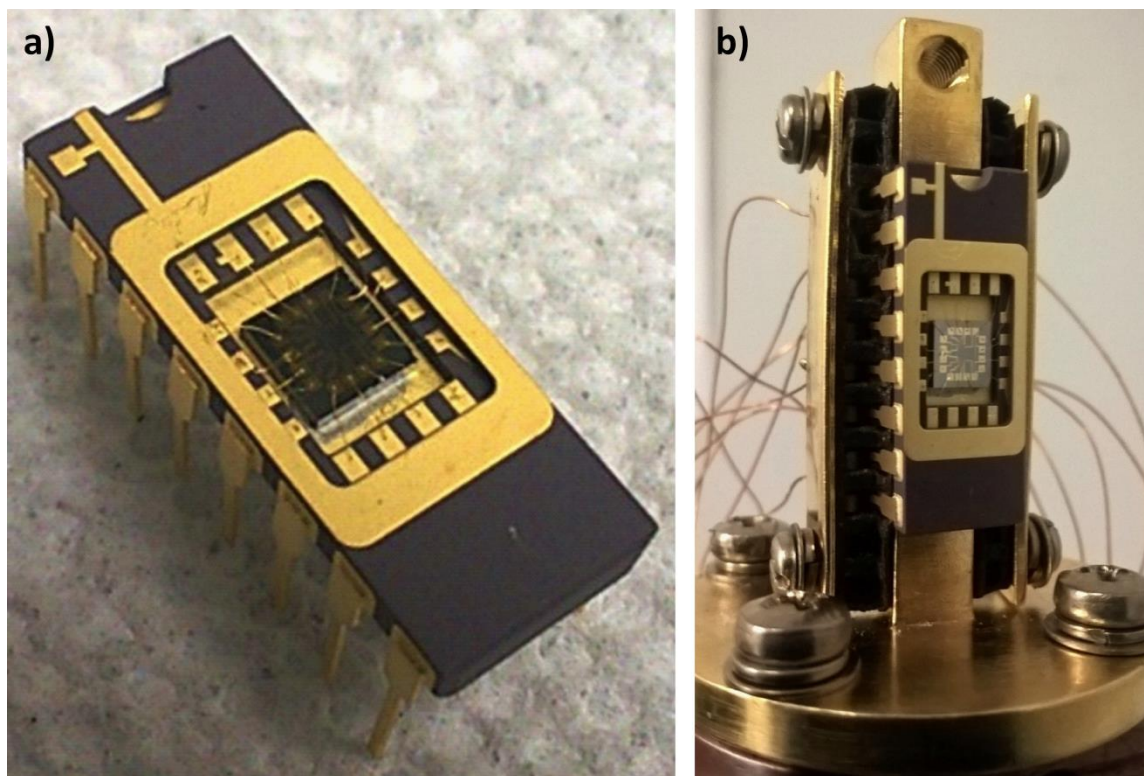


Figure 4-4: a) A microdevice inserted in a commercially available 16-pin ceramic chip carrier package. b) Packaged microdevice loaded into the cryostat.

4.3.4 Experimental Setup

The ceramic chip carrier package was loaded into a cryostat (Janis Research) with a high precision Si diode temperature sensor and closed-loop temperature control. The cryostat was maintained at a high vacuum (10^{-5} torr) via a turbomolecular pump (Leybold) in conjunction with a mechanical pump (Edwards). For minimizing the errors due to radiative heat loss from the sample, the sample space within the cryostat was radiation shielded. A LakeShore 335 temperature controller (Lake Shore Cryotronics, Inc.) was used to ensure temperature stability to within 0.01 K. The entire data collection process was executed using a computer with LabVIEW software to control the frequency of the AC signal and to record the voltage drops, the function generator (Stanford Research Systems DS360), the temperature controller, and the lock-in amplifier (Stanford Research Systems SR830). **Figure 4-4 (b)**

shows a packaged microdevice after being loaded into a cryostat. The image of the entire experimental setup used for the $\kappa_{cross-plane}$ of measurements is shown in **Figure 4-5**.

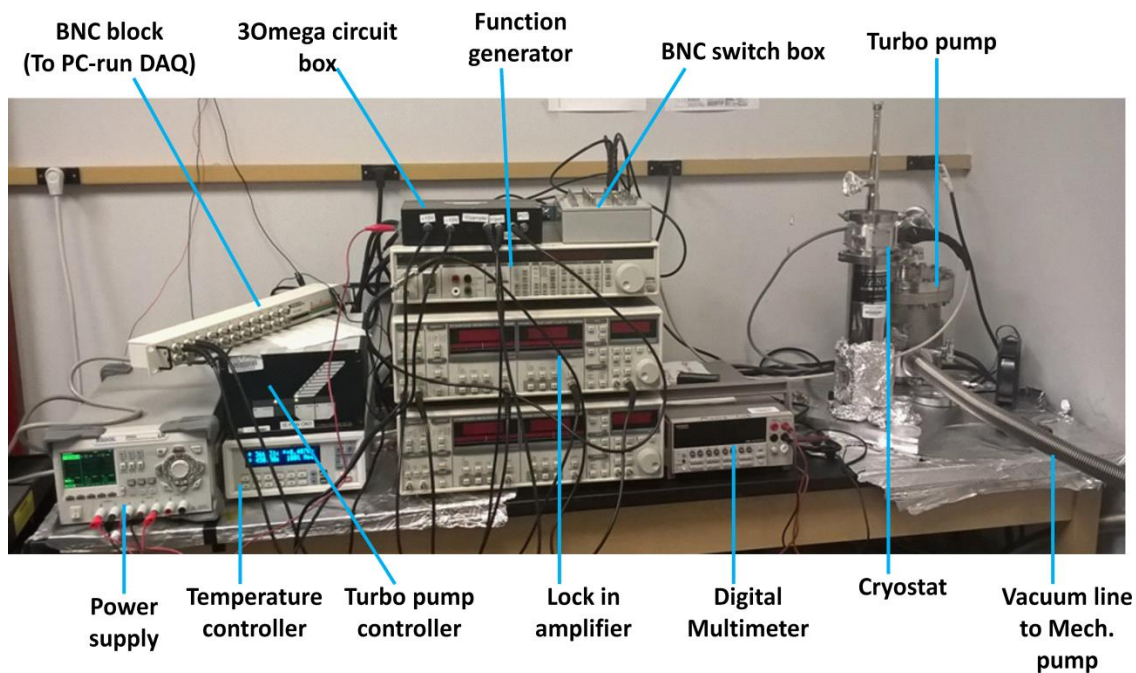


Figure 4-5: Image of the 3ω experimental setup.

4.3.5 Measurement

The $\kappa_{cross-plane}$ was measured for the ambient temperatures between 125 K and 425 K. Liquid nitrogen was used to set the temperature below 300 K. The following parameters were measured at each temperature to determine the $\kappa_{cross-plane}$ of each thin film sample: the resistance of the thermometer/heater line, and the 1ω and the 3ω voltage on the metal line as a function of frequency. **Figure 4-6** shows the schematic diagram of the experimental setup used for the measurement of the $\kappa_{cross-plane}$.

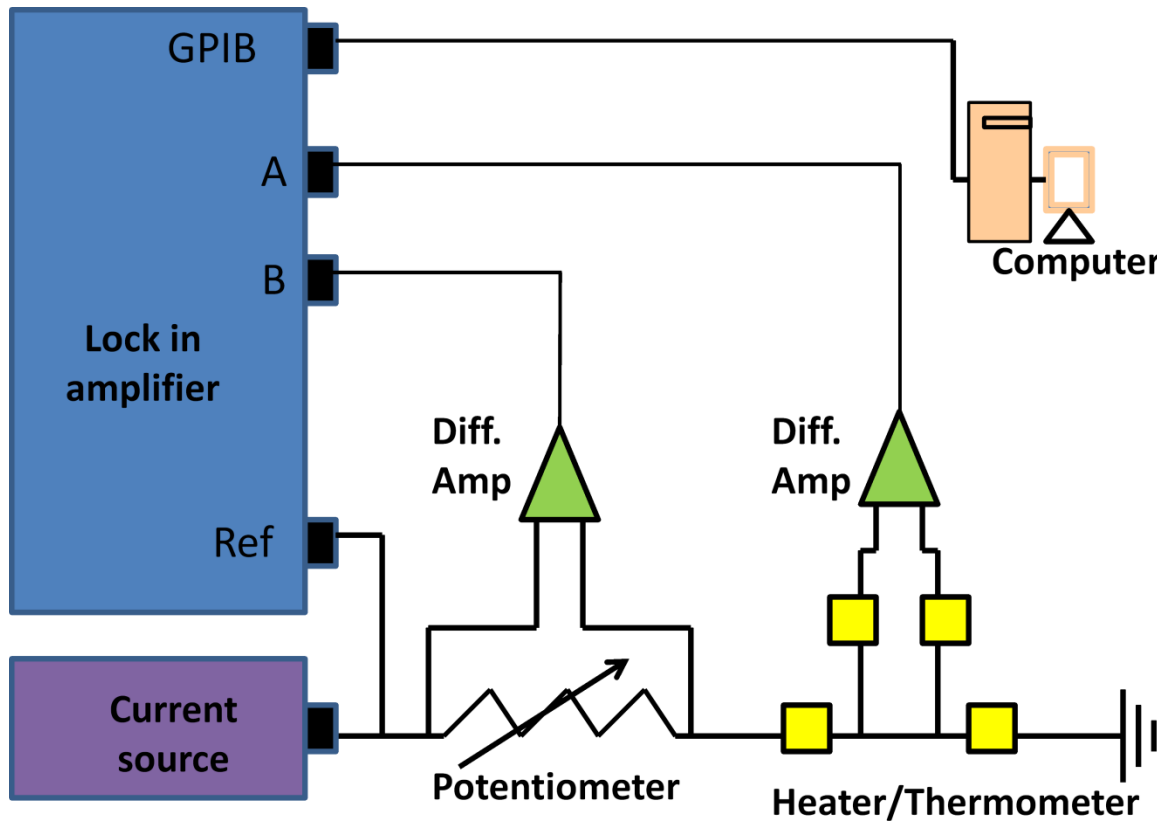


Figure 4-6: Schematic diagram of the experimental setup used for the 3ω method. Adapted from Ref. [214].

First, the four-probe electrical resistance of 3ω the metal line was measured using a small AC sensing signal $i_{ac} = 50 \mu\text{A}$ monitored via the lock-in amplifier. This resistance value was also used to find the change in resistance of the metal line with temperature, dR/dT . Then, using the ultra-low distortion function generator, a small AC current was passed through a ten-turn potentiometer which is in series with the metal line, such that the Joule heating was negligible within the metal line. The same signal was also connected to the reference input of the SR830 lock-in amplifier (Stanford Research Systems). The voltages across the metal line and the potentiometer were measured by unity gain differential amplifiers and ultimately via the inputs “A” and “B” of the SR830 lock-in

amplifier. The lock-in amplifier was connected via a GPIB (general-purpose interface bus) interface to a computer that automates the measurement process.

For measuring the 1ω voltages across the metal line, the frequency of the signal from the DS360 ultra-low distortion function generator was varied and the corresponding voltage drops were recorded via a combination of a lock-in amplifier, computer-controlled data acquisition system, and a LabVIEW program. The final parameter required for the measurement was the 3ω voltage as a function of frequency at the same frequencies used for the 1ω . Since the 1ω voltage had a magnitude on the order of 1000 times larger than the 3ω voltage, it needed to be subtracted before the 3ω voltage could be measured by the lock-in amplifier. In order to do so, the voltages across the metal line and potentiometer were measured by a Keithley 2000 digital multimeter and the voltage drop across the potentiometer was adjusted until they both were equal. Then, using the differential input (A-B) of the lock-in amplifier, the large 1ω voltages across the metal line and the potentiometer were removed, and hence, the 3ω voltages were obtained. This removes any unwanted oscillations in the line signal, leaving only the oscillations due to the temperature fluctuations on the surface of the sample [218]. The 3ω voltage at each frequency was measured by the lock-in amplifier as shown in **Figure 4-7** and recorded by the LabVIEW program.

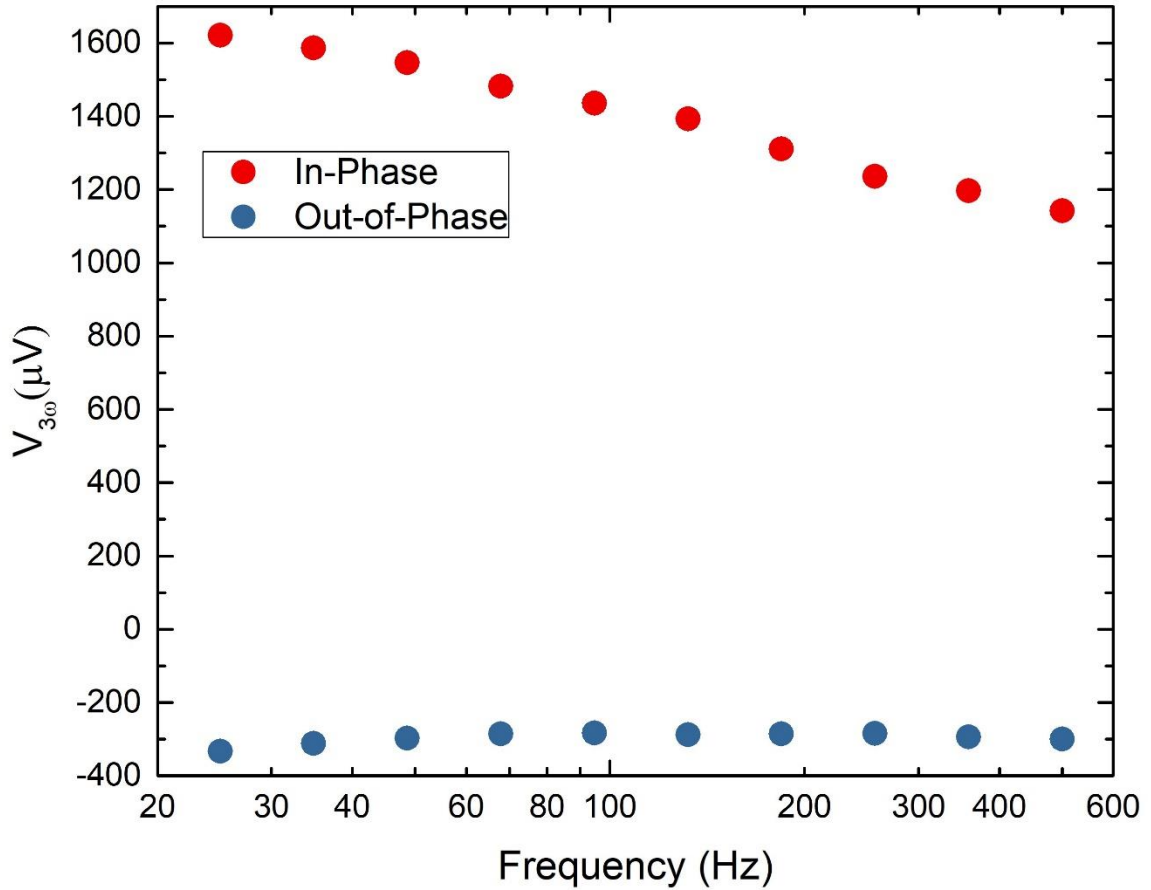


Figure 4-7: Measured 3ω voltage as a function of frequency for the 20 cycles UNCD sample at 350 K.

4.4 Results and Discussion

To validate our experimental setup and procedure, the $\kappa_{cross-plane}$ of the SiO_2 film and Si substrate were first measured. Results for both were in agreement with the values reported in the literature [47], [219], especially at higher temperatures where the defects and doping are relatively unimportant as shown in **Figure 4-8**. As expected for the semiconductor crystals near room temperature, the $\kappa_{cross-plane}$ of the Si substrate varies as $\sim 1/T$. A difference in the $\kappa_{cross-plane}$ of the Si substrate can be observed below 200 K due to differences in sample doping since defect scattering becomes prominent for Si at such

temperatures [220]. At 200 K, the difference in the value of $\kappa_{cross-plane}$ with respect to the literature value was $\sim 36\%$ and at room temperature, it was $\sim 23\%$. The $\kappa_{cross-plane}$ of a 200 nm thick SiO₂ film is shown in **Figure 4-8 (b)** along with the data from Cahill *et al.* [219]. The measured data follow the trend of the literature data with an uncertainty of $\pm 9\%$. The uncertainty was calculated by using **Eq. A-1** and the main sources of uncertainties were associated with the accuracy in the measurement of the width and the length of the 3ω line, the dR/dT data of the 3ω line, and the measured 3ω voltage data.

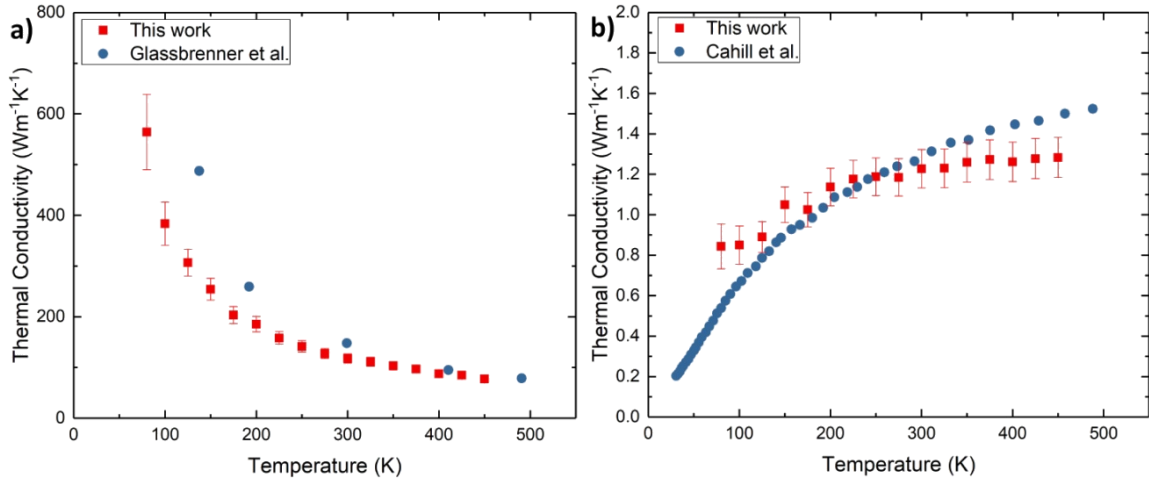


Figure 4-8: Measured $\kappa_{cross-plane}$ of a) Si compared with the data from [221]. b) SiO₂ compared with the data from [219].

Figure 4-9 shows the measured $\kappa_{cross-plane}$ of the three UNCD samples as a function of temperature. The total thickness of the UNCD films were 104.3 ± 56.2 nm, 127.9 ± 14.6 nm, and 139.1 ± 19.5 nm for the samples obtained after 10, 15, and 20 cycles of the coating of the UNCD film on the Si substrates.

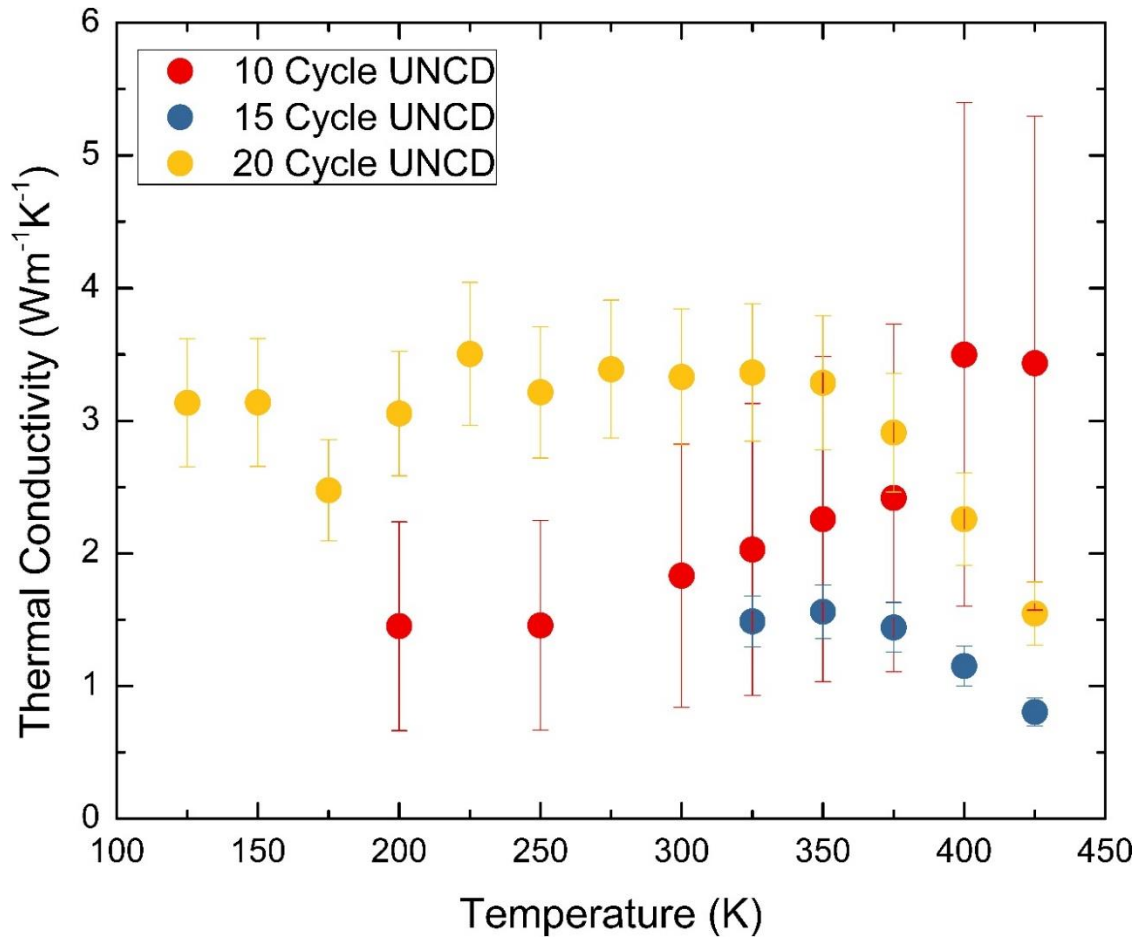


Figure 4-9: Measured $\kappa_{cross-plane}$ of the UNCD samples as a function of temperature.

The $\kappa_{cross-plane}$ of the UNCD samples increased slowly with an increase in temperature to a certain limit and then started to decrease. The $\kappa_{cross-plane}$ of the sample with 20 cycles UNCD increased slightly with the temperature with values of $3.13 \pm 0.48 \text{ W m}^{-1} \text{ K}^{-1}$ to $3.29 \pm 0.51 \text{ W m}^{-1} \text{ K}^{-1}$ from 125 K to 350 K, and then decreased rapidly with increasing temperatures. Similarly, for the sample with 15 cycles UNCD, the value of $\kappa_{cross-plane}$ changed from $1.49 \pm 0.19 \text{ W m}^{-1} \text{ K}^{-1}$ to $1.44 \pm 0.19 \text{ W m}^{-1} \text{ K}^{-1}$ between 325 K to 375 K and started to decrease significantly after that. Lower $\kappa_{cross-plane}$ values below ~ 300 K may be due to the scattering of phonons from point defects, extended defects, dislocations, and grain boundaries [222] while the dominant phonon-phonon scattering can

be attributed for the region where the values of the $\kappa_{cross-plane}$ started decreasing (at temperatures above 350 K) [185], [223], [224]. Compared to other samples, the 20 cycles UNCD sample showed higher $\kappa_{cross-plane}$ that was as high as $3.50 \pm 0.54 \text{ W m}^{-1} \text{ K}^{-1}$, which was even higher ($\sim 1.5 \text{ W m}^{-1} \text{ K}^{-1}$) than the thicker ($\sim 900 \text{ nm}$) CVD grown UNCD film reported by Angadi *et al.* [195]. It may be due to a decrease in the porosity of the film and the improved interface between the film and the Si substrate with increased deposition cycles. The values of the $\kappa_{cross-plane}$ for the 10 cycles UNCD sample had uncertainties as high as $\pm 50\%$ which can be due to high uncertainty in the film thickness since it was the thinnest sample and potentially very high porosity.

In contrast, **Figure 4-10** shows the measured thermal resistance of the three samples, that includes inter-particle thermal resistances as well as the thermal boundary resistance (TBR) at the interface between UNCD film and the Si substrate, as a function of temperature. It can be observed that the uncertainty associated with the 10 cycles UNCD sample is approximately $\pm 6.3\%$. That is very small compared to that associated with its $\kappa_{cross-plane}$ values. Similarly, the uncertainties of the 15 cycles and 20 cycles UNCD samples associated with the thermal resistances were only $\pm 6.2\%$ which were very small compared to $\pm 13\%$ and $\pm 15.4\%$ that were related to their $\kappa_{cross-plane}$ values. Thus, the uncertainty in film thickness is a major contributor to the overall uncertainty in the film's κ . It can be observed that 20 cycles UNCD sample had the lowest thermal resistance values between 125 K to 350 K which may be due to increased film quality and reduced porosity as mentioned in the study by Shamsa *et al.* [200] for DLC film in which they reported an increase in κ of DLC film with an increase in the density of the film.

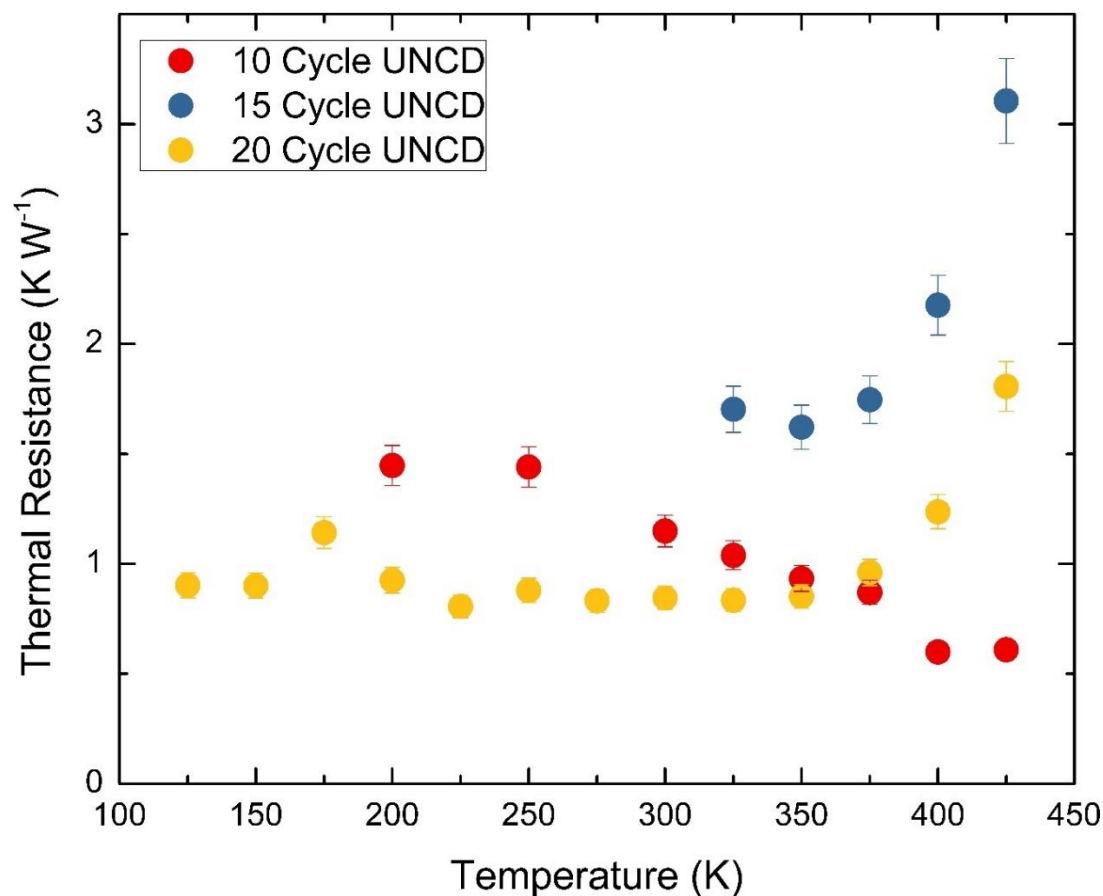


Figure 4-10: Measured thermal resistance as a function of temperature.

In the past, most of the studies had been performed on the CVD grown UNCD films thicker (thickness at least 900 nm) [225]–[227] than that of our samples, hence much higher $\kappa_{cross-plane}$ values due to change in the interface structure from porous to nonporous [195]. Therefore, the UNCD films grown by the CVD method provided better quality films with high particle density, low porosity and better interface with the substrate. However, our very thin samples that were prepared by a solution-based method resulted in high porosity with a lot of voids between the particles that trapped air. Even if the individual ND particles were thermally conductive, the presence of a high number of voids between the particles make the inter-particle resistances high and hence decrease the $\kappa_{cross-plane}$ values. Another

reason might be the presence of large voids at the interface between the UNCD film and the Si substrate [195]. As a result, TBR increases and makes the $\kappa_{cross-plane}$ even lower. The TBR at the solid-solid interface becomes important for the thermal stability of the electronic circuits, superconducting devices, and the whole package itself [227].

4.5 Conclusion

In this chapter, the thermal characterization of the covalently assembled ND films on Si substrates was performed by using the microfabricated device that was able to measure the $\kappa_{cross-plane}$ as well as the $\kappa_{in-plane}$. Only the $\kappa_{cross-plane}$ was measured in this work through the well-established 3ω method for the UNCD samples of different thicknesses. The $\kappa_{cross-plane}$ did not show significant change with temperature where the inter-particle scattering was dominant and started decreasing rapidly at higher temperatures due to phonon scattering. The sample with the largest thickness (20 cycles UNCD sample) had the $\kappa_{cross-plane}$ as high as $3.50 \pm 0.54 \text{ W m}^{-1} \text{ K}^{-1}$. The $\kappa_{cross-plane}$ values obtained in this work represented the lower bounds and were much lower than that of the CVD grown UNCD films which may be due to higher porosity and poor interface quality (higher thermal resistance). Also, the higher uncertainty in film thickness was the major contributor to the larger error bars in the measured $\kappa_{cross-plane}$ values. The results obtained in this work suggests that there is still more room for improvement through which solution-based technique can be used as an alternative to the CVD grown UNCD films for thermal management applications in MEMS/electronic devices.

CHAPTER 5

SUSPENDED BEAM MICRODEVICE FABRICATION THROUGH STANDARD PHOTOLITHOGRAPHY FOR THERMOELECTRIC CHARACTERIZATION OF NANOMATERIALS

5.1 Introduction and Motivation

Recent achievements in the field of nanotechnology have shown great potential for developing novel technologies. However, there is a need for accurate manipulation of matter as well as a precise calculation of energy transport at the micro- and nanoscales for the realization of this potential. Proper instruments and measurement techniques are essential for achieving these research goals. For example, the study of energy transport at micro or nanoscale requires devices that can measure the related parameters with minimum error and ultimately help to realize the potential of nanotechnology [165]. In the past few decades, there has been rapid growth in the study of nanoscale thermal transport. The phenomenon of thermal transport is different at nanoscale compared to its bulk counterpart, especially for the materials with characteristics length comparable to or smaller than the mean free path of the energy carriers (phonon/electron). A better understanding of such phenomena leads towards the development of devices for resolving thermal management issues [70], [228]. In some cases, Fourier's law of heat conduction or Stefan-Boltzmann law of radiative heat transfer are not sufficient to explain the thermal transport at a nanoscale range; hence, such studies require calorimeter devices with very high resolution.

The characterization of the thermal transport properties of nanomaterials is more challenging because the issues such as radiation loss, heat loss to the thermometers, and contact thermal resistances can cause large uncertainties in the κ measurements. In the past few decades, a number of measurement methods have been developed for experimental investigation of phonon transport such as the microdevices with RTs patterned on suspended beams, micro-Raman spectroscopy, time-domain thermoreflectance (TDTR), the 3ω method, the scanning thermal microscope, sources of coherent phonons, and bi-material cantilever thermal sensors [70], [229]. Tighe *et al.* [69] developed one of the first devices for direct measurement of the G of patterned, suspended GaAs nanobeams in the temperature range of 1.5 K - 6 K. Fabrication of these devices included two separate EBL steps, first, to develop the patterns of heavily doped GaAs electrical conductors (serpentine heaters and electrodes) and, second for the central thermal reservoir ($\sim 3 \mu\text{m}^2$) and four GaAs nanobeams (cross section $\sim 200 \text{ nm} \times 300 \text{ nm}$). Then a subsequent anisotropic, vertical, chemically assisted ion beam etching (CAIBE) step was performed to remove the layer of heavily doped GaAs from unwanted regions.

In order to measure the G , one of the serpentine heaters on the central membrane was heated by supplying a DC current and the temperature rise on the central membrane was monitored via a small modulated sensing current on the other serpentine RT [69]. Schwab *et al.* [230] successfully performed high-resolution calorimetric measurements to experimentally demonstrate the quantization of G at cryogenic temperatures. They fabricated a microdevice consisting of a $\sim 60 \text{ nm}$ thick SiN_x suspended central membrane with four supporting SiN_x beams. Serpentine heater and sensor were patterned with Au film (thickness $\sim 25 \text{ nm}$) on the central membrane and four niobium (Nb) leads (thickness

~ 25 nm) were patterned to provide electrical connection between the central membrane and the contact pads [230].

Shi *et al.* [70] fabricated suspended microdevices with two adjacent symmetric SiN_x membranes, each suspended by five SiN_x beams (~ 420 μm X 2 μm X 5 μm). A PRT coil (~ 30 nm thick and ~ 300 nm wide) was fabricated on each membrane using EBL. It was connected to the bonding pads on the substrate via Pt leads on the long SiN_x beams. Joule heating created on one membrane causes heat flow through the sample to another membrane that helps for measuring the G , σ , and Seebeck coefficient (S) of single-walled CNT bundles bridging the two membranes in the temperature range of 4 K - 400 K. In addition to EBL, the fabrication of this microdevice also involved low-pressure CVD (LPCVD) for depositing SiN_x and SiO₂ films and reactive ion etching (RIE) for transferring a pattern to the SiN_x film [70].

Kim *et al.* [71] also performed mesoscopic thermal transport measurements of individual multi-walled CNTs in the temperature range of 8 K-370 K by using a similar microfabricated suspended device. Similar microdevice designs were used by different research groups [231]–[235] for measuring the thermoelectric properties of a variety of the nanostructures. Furthermore, the design of the device was modified by adding two more electrodes on each membrane to measure the thermoelectric properties (Seebeck coefficient, four-probe electrical conductivity, and κ) of indium arsenide (InAs) nanofilms [236], individual chromium disilicide NWs [237], individual bismuth (Bi) NWs [238].

Raman spectroscopy has also been used to study the relation between the basal plane κ and the thickness of the few-layer graphene (FLG) [184]. Single-layer graphene (SLG) has been studied using Raman measurements [235], [239], [240], but the optical

absorbance and the κ values were lower than the initial work [182]. The Raman thermometry method has some issues such as large uncertainties in the optical absorbance and the limited temperature sensitivity that have prevented the experimental verification of the lateral size dependence of the κ of suspended graphene [240]. The measurement approaches described above consist of sample materials suspended between the isolated membranes.

Thermal transport properties of embedded or freely suspended nanomaterials are different than when they are supported on other materials due to the leakage of scattering phonons across the nanomaterial-support interface. Moreover, the phonon-interface interactions also depend on the nanomaterial sample preparation method such as thermal decomposition, CVD. Boukai *et al.* [241] performed thermoelectric measurements of Si NW arrays by using microdevice with a central suspended membrane of SiO₂ (~ 150 nm thick) which supports Si NW arrays. In addition, electrodes and serpentine heaters of Pt/Ti were also fabricated on the SiO₂ membrane using EBL and e-beam evaporation. Finally, the electrodes were connected to the large Au contact pads that were defined by photolithography. SLG is usually supported on a dielectric substrate for device application [242]. Chen *et al.* [243] observed about 10 times the suppression of the charge mobility in SLG supported on SiO₂ compared to the suspended SLG due to the scattering by substrate phonons and impurities. Microdevices with different designs have been used to study thermal transport in FLG and SLG. Seol *et al.* [242] used a microfabricated suspended device to perform thermal transport measurements on SLG supported on a ~ 300 nm thick central SiO₂ beam that was suspended by using Tetramethylammonium hydroxide (TMAH) and the Au/Cr RT lines were patterned with EBL and a metal lift-off technique.

Although the microdevices mentioned above have been successfully used by different research groups for studying the thermoelectric properties of nanomaterials, it is worth mentioning that the fabrication of such devices includes various steps that are complicated and time-consuming such as EBL, LPCVD, and such kinds of instruments might not be available with all research institutes. Therefore, there is a need for techniques for fabrication of similar microdevices using standard photolithography steps that are straightforward, simple, less time-consuming, and less expensive.

5.2 Research Objectives

The goal of this work was to develop a simple and less time-consuming technique for batch fabrication of suspended beam microdevices for thermoelectric characterization of nanomaterials. To achieve this goal, the following specific objectives were to be achieved through this research:

- Use standard photolithography technique for the batch fabrication of suspended beam microdevices.
- Perform thermal characterization of the central suspended SiN_x bridge.

The suspended beam microdevices were fabricated through a combination of standard photolithography and wet etching. The $\kappa_{in-plane}$ of the central suspended SiN_x (thickness ~ 500 nm) bridge was obtained through DC Joule heating approach for a temperature range of 85 K- 460 K. In subsequent works, a nanomaterial sample of interest can be placed on the central SiN_x bridge to determine its thermoelectric properties.

5.3 Experimental Materials and Methods

5.3.1 Microdevice Design and Fabrication

The microdevice design consists of two adjacent suspended SiN_x beams each having a length of 832 μm and width of 15 μm connected to each other via a central SiN_x bridge (10 μm long and 5 μm wide central nitride bridge). Furthermore, each suspended beam consists of a series of three Pt/Ti (titanium) lines of 2 μm wide and 40 nm thick (Pt/Ti with a thickness of 30 nm/10 nm). The outer PRTs were used for the measurement of the $\kappa_{in-plane}$ and the inner four Pt/Ti lines were used as electrodes during the measurement of the σ and the S of the sample (when present). The Pt/Ti lines were ultimately connected to the larger contact pads (400 μm X 400 μm), and finally, electrical connections were made through a wire-bonding technique. Pt was chosen due to the relatively high and extremely linear dR/dT and better adhesion with Ti.

An illustration of a single microdevice created via the SolidWorks software is shown in **Figure 5-1**.

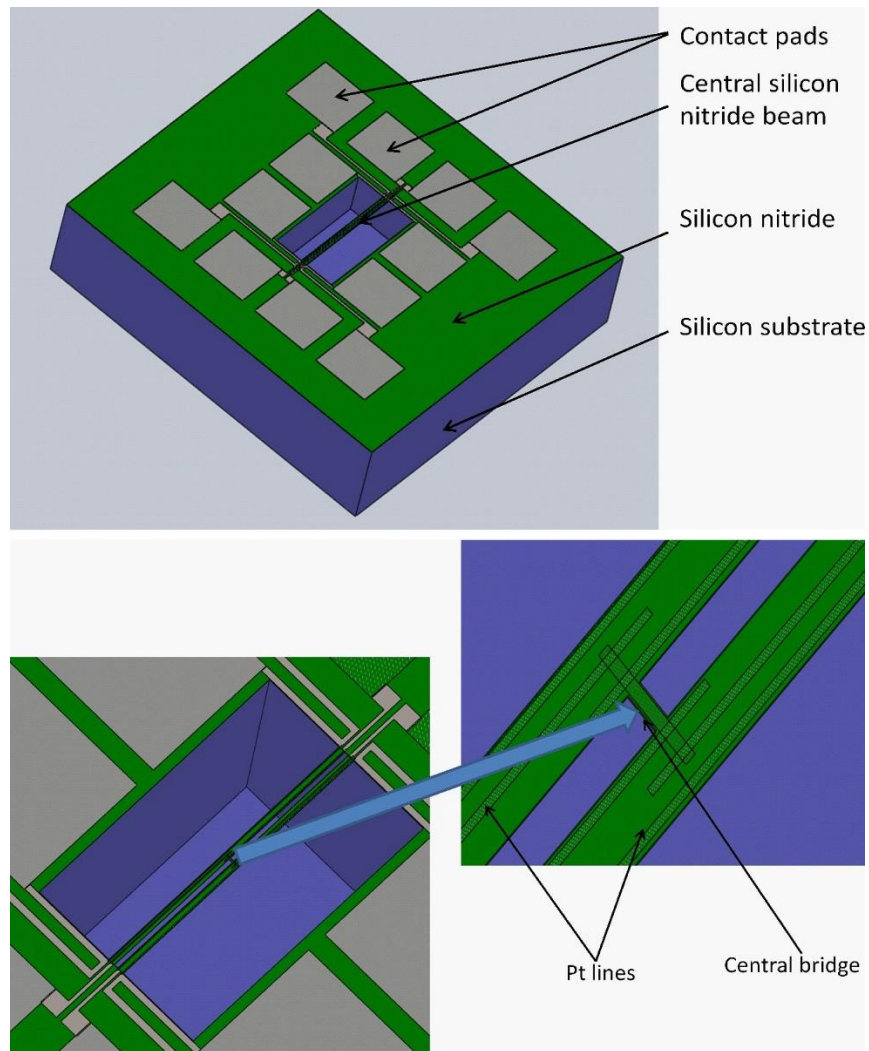


Figure 5-1: Illustration of a suspended beam microdevice. A single device showing the contact pads along with the suspended SiN_x beams (top). Detail of the suspended SiN_x beams showing all the Pt lines and the central bridge (bottom). Not to scale.

Multiple photomasks were designed via the LayoutEditor software package after finalizing the design as shown in **Figure 5-2** and were used for microdevice fabrication using the standard photolithography process at Louisiana Tech University's Institute for Micromanufacturing.

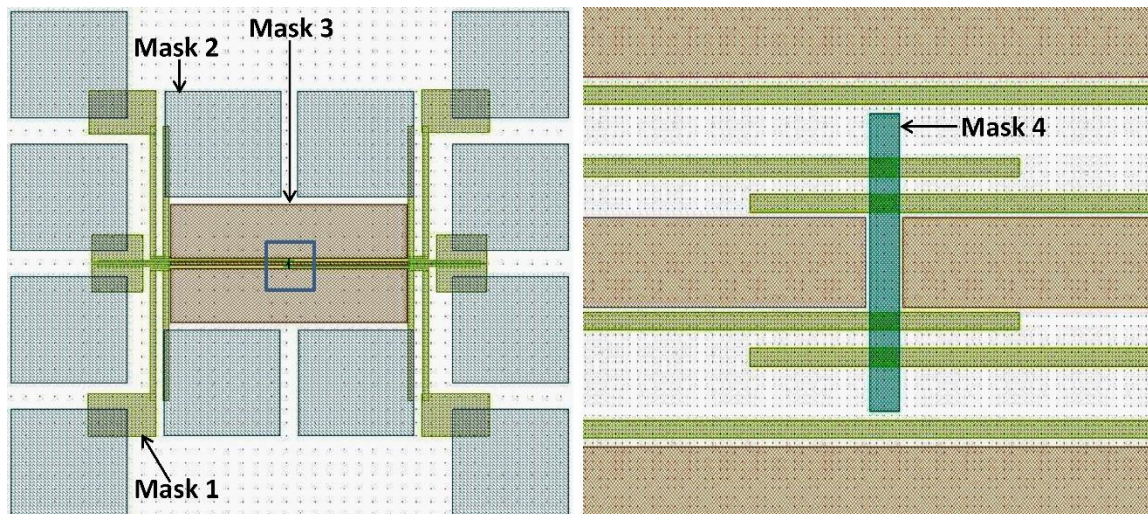


Figure 5-2: A combined photomask design created via LayoutEditor showing a single microdevice with a centralized region outlined in blue (left). Detail of the blue boxed region showing all the metal lines on the suspended beam (right). Not to scale.

To begin the fabrication of an array of suspended beam microdevices, first, a layer of LOR 5B was spin coated on a 100 mm diameter SiN_x-on-Si wafer (500 nm thick SiN_x on 500 μm thick Si wafer). Then, a layer of Shipley 1813 photoresist was spun on the soft baked layer of LOR 5B followed by UV exposure through the first mask file and a subsequent development step in the MF-319 developer for developing the patterns with smaller contact pads, the Pt/Ti lines on the central suspended beams, and the alignment marks. The width of each Pt/Ti line, as well as the minimum gap between them, are 2 microns. The metal lift-off process becomes very difficult for such smaller features. The dissolution rate of LOR 5B is faster than that of the Shipley 1813 photoresist in the MF-319 developer. Therefore, LOR 5B can create nice undercuts and enhance the metal lift-off process as shown in **Figure 5-3**. After confirming all the desired features under a light microscope, a 10 nm-thick Ti adhesion layer and a 30 nm-thick Pt layer were sequentially deposited using DC magnetron sputtering and a metal lift-off process was performed by soaking the wafer in Remover PG at 80 °C.

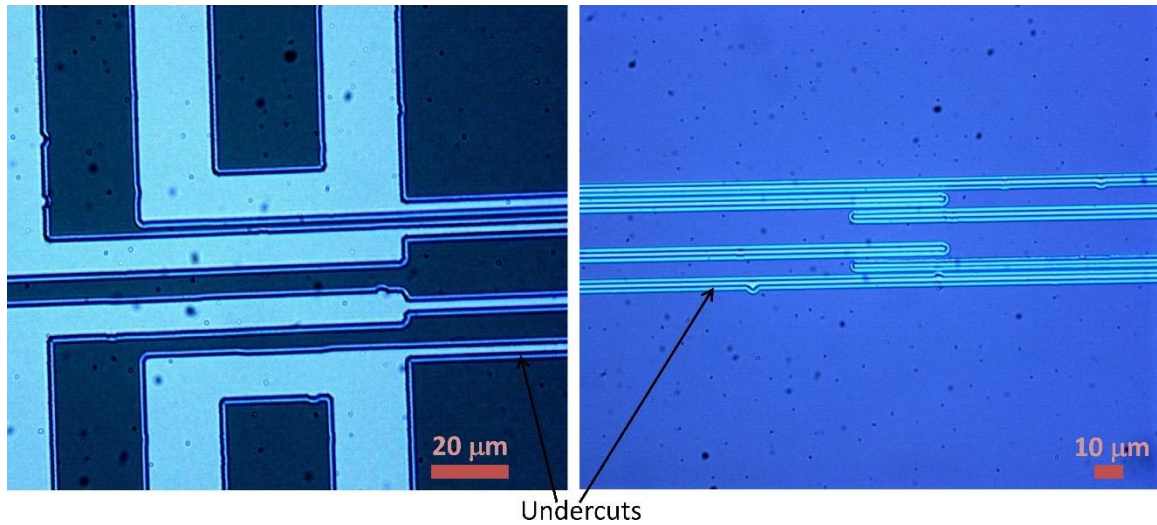


Figure 5-3: Light microscope images with the undercuts obtained by using LOR 5B.

After confirming the desired features under a light microscope, similar steps were again repeated starting with spin-coating of LOR 5B, then Shipley 1813 photoresist on the wafer from the previous step, followed by the alignment with the alignment marks with that obtained from the first mask file, and UV exposure through the second mask file using a mask aligner. A subsequent development step in the MF-319 developer followed by sputtering of Pt/Ti (30 nm/10 nm) and metal lift-off process resulted in larger contact pads. Then, a layer of Shipley 1813 photoresist was spun, and another UV exposure was performed through the third mask file for exposing the windows in SiN_x . The exposed portion of the SiN_x was subsequently removed by using RIE with sulfur hexafluoride (SF_6) gas that exposed the underlying layer of Si followed by device dicing into the individual microdevice. Individual microdevice was placed in a solution containing 5% TMAH in DI water at 110°C until the SiN_x beams had been sufficiently suspended as indicated by a pink color as shown in **Figure 5-4**. It took nearly 12 hours to obtain the two adjacent-suspended

beams. The microdevice was subsequently rinsed in DI water and then in isopropyl alcohol (IPA) as the final rinse to get rid of the DI water and dried.

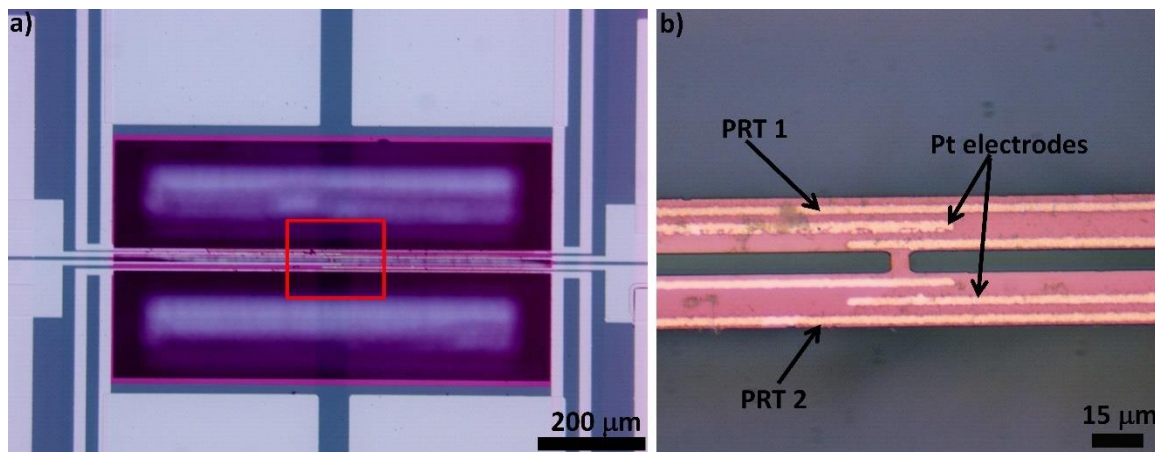


Figure 5-4: Light microscope images of a) a microdevice with central nitride beam being suspended after treatment with TMAH solution as indicated by the pink colored region. b) Details of the red boxed region showing the suspended beam along with the Pt lines.

The sample of interest (NWs, NTs or thin films) can be deposited in the rectangular region with a dimension of $4\ \mu\text{m} \times 33\ \mu\text{m}$ along the central bridge. This pattern can be developed by a standard photolithography step using the fourth mask file as indicated by the green color in **Figure 5-2**. Following dicing of the wafer/chip, the individual microdevice was adhered to a commercially available 16-pin ceramic chip carrier package using silver epoxy and a wire-bonding technique was used for electrical connections to the Pt lines.

5.3.2 Experimental Setup

The experimental setup was similar to the one mentioned in CHAPTER 4. The ceramic chip carrier package was loaded into a cryostat (Janis Research). A turbomolecular pump (Leybold) in conjunction with a mechanical pump (Edwards) was used to maintain a high vacuum (10^{-5} torr) inside the cryostat. Also, the temperature stability was maintained

within 0.01 K via a LakeShore 335 temperature controller (Lake Shore Cryotronics, Inc.). A fixed DC voltage was supplied via a DAQ module for inducing Joule heating. The entire data collection process was executed using a computer with LabVIEW software, the temperature controller, the lock-in amplifiers (Stanford Research Systems SR830), and a DAQ module.

5.3.3 Measurement

During the experiment, the temperature of the sample stage (T_{stage}) within the cryostat was maintained between 85 K to 460 K to study the effect of the ambient temperature on the κ . The ambient temperature was maintained below room temperature by using liquid nitrogen. The G of the central suspended SiN_x bridge was measured with and without the sample. Then the difference will be treated as the G of the sample alone, and that will be used to determine the $\kappa_{in-plane}$ of the sample.

In this work, we measured only the $\kappa_{in-plane}$ of the bare central suspended SiN_x bridge which is described here. Different kinds of nanomaterial samples can be placed on the central suspended bridge region for studying thermoelectric properties. As mentioned above, only the outer PRTs (PRT1 and PRT2) as shown in **Figure 5-4 (b)** were used for the measurement of $\kappa_{in-plane}$. The measurement technique is based on the four-probe thermoelectric measurement as mentioned in the Ref. [70], [233], [244]. Once the T_{stage} was stabilized to within 0.01 K, Joule heating was induced on PRT1 (heater side) by a DC current (I_{DC}) that was ramped from 0 μA to $-50 \mu\text{A}$, $-50 \mu\text{A}$ to $+50 \mu\text{A}$, and $+50 \mu\text{A}$ to 0 μA with 203 steps per ramping cycles. The beams are suspended, hence, the temperature of the PRTs quickly reached the steady-state that would take a longer time for a supported structure. Due to the Joule heating on the PRT1, a certain amount of heat flows through the

bridge towards the PRT2 (sensor side) that causes an increase in the electrical resistance of the PRT2 as well.

The electrical resistance of the PRT1 can be obtained from the I - V curve as $R_h = V/I_{DC}$. However, the R_h value becomes noisier when the value of I_{DC} approaches zero. To overcome this issue, a small sinusoidal AC current was coupled to the large DC heating current I_{DC} on the heater side. The four-probe electrical resistances of PRT1 and PRT2 were measured with a small sinusoidal current ($i_{ac} = 500$ nA) and the lock-in amplifier. The measured electrical resistance of each PRT showed a quadratic dependence on the heating current I_{DC} as shown in **Figure 5-5**. For each PRT, the value of the electrical resistance during the I_{DC} ramping up cycles was the same as that measured during the I_{DC} ramping down cycles. This verified that the delay time that was set for each measurement was enough compared to the thermal time constant of the device.

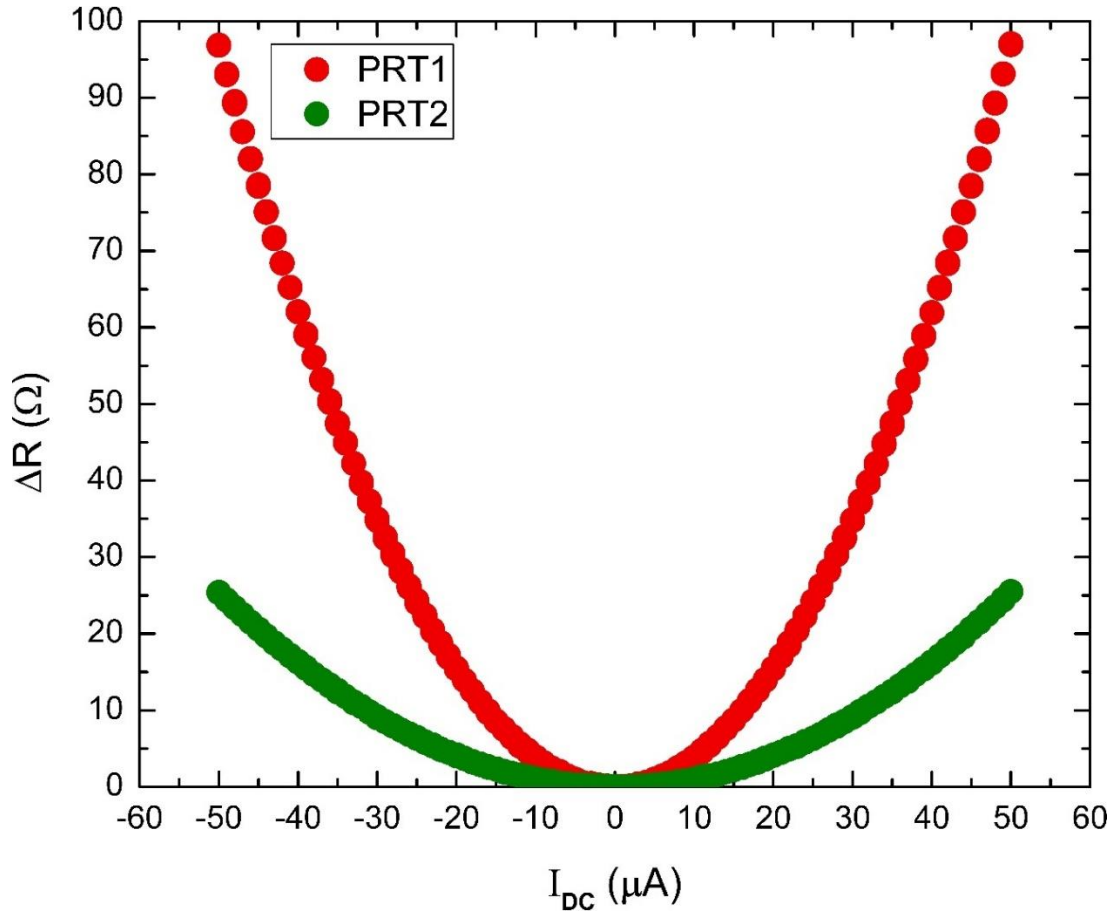


Figure 5-5: Measured electrical resistance increase of the PRT1 and PRT2 as a function of the heating current (I_{DC}) when $T_{stage} = 360$ K.

Figure 5-6 shows that the electrical resistances of the PRTs vary linearly with T_{stage} for $I_{DC} = 0$. The slope of this curve is the change in electrical resistance with temperature dR/dT and the values were $6.91435 \text{ } \Omega \text{ K}^{-1}$ and $3.78447 \text{ } \Omega \text{ K}^{-1}$ for PRT1 and PRT2, respectively. These values were used to determine the average temperature rise ($\overline{\Delta T}$) of the PRTs. The average temperature rise measured on the heater ($\overline{\Delta T}_h$) and the sensor ($\overline{\Delta T}_s$) lines can be related to the corresponding midpoint temperature rises ΔT_h and ΔT_s as mentioned by Seol *et al.* [244]:

$$\Delta T_s = 2\overline{\Delta T_s} \quad \text{Eq. 5-1}$$

$$\Delta T_h = \frac{3}{2}\overline{\Delta T_h} - \frac{1}{2}\overline{\Delta T_s} \quad \text{Eq. 5-2}$$

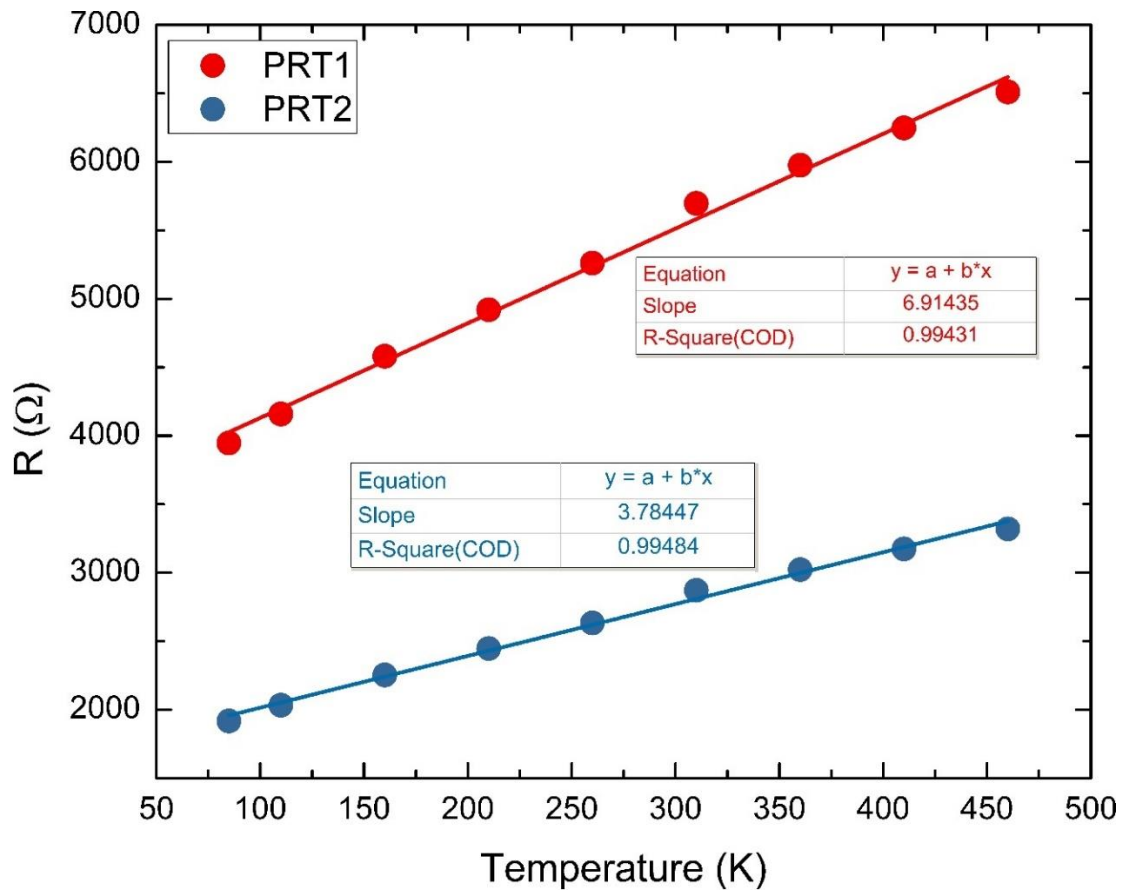


Figure 5-6: Measured four-probe electrical resistance values for PRT1 and PRT2 at various temperatures. The lines are the linear fits to the corresponding measurement data whose slopes give dR/dT values.

The thermal conductance of each beam (G_b) and the thermal conductance of the sample region (G_s) (central suspended SiN_x bridge for this case) were calculated as [70]:

$$G_b = \frac{Q_{total}}{\Delta T_h + \Delta T_s} \quad \text{Eq. 5-3}$$

$$G_s = G_b \frac{\Delta T_s}{\Delta T_h - \Delta T_s} \quad \text{Eq. 5-4}$$

where Q_{total} is the total Joule heat dissipated in the PRT1 on the heating membrane, ΔT_h and ΔT_s are the temperature rise on the PRT1 and PRT2, respectively. The value of G_b was determined from the slope of the least-square linear curve fit of Q_{total} as a function of $(\Delta T_h + \Delta T_s)$ as mentioned in **Eq. 5-3** which is also shown in **Figure 5-8**. Furthermore, the ratio G_s/G_b was determined as the linear curve fit of ΔT_s as a function of $(\Delta T_h - \Delta T_s)$ as mentioned in **Eq. 5-4** that is also shown in **Figure 5-9**. Finally, the $\kappa_{in-plane}$ of the central suspended SiN_x bridge was calculated as:

$$\kappa_{in-plane} = G_s \frac{L_s}{W \cdot t} \quad \text{Eq. 5-5}$$

where W and t are the width and thickness of the bridge. L_s is the length of the bridge (the region of the central suspended bridge covered by the sample), and its value was estimated from the ANSYS finite element analysis as shown in **Figure 5-7**.

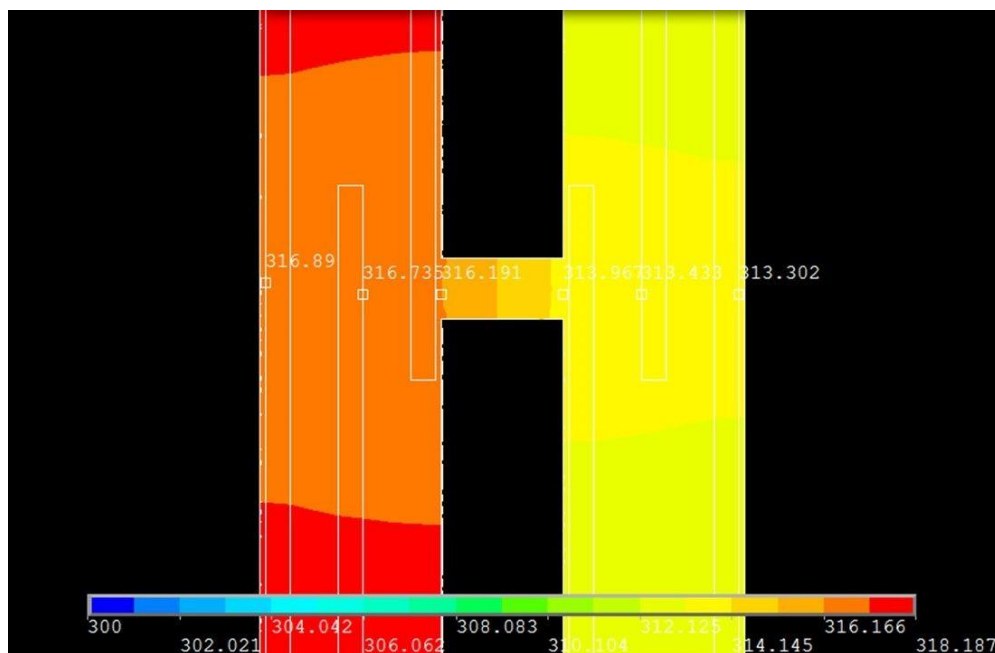


Figure 5-7: ANSYS finite element analysis of the suspended beams with the temperature contours.

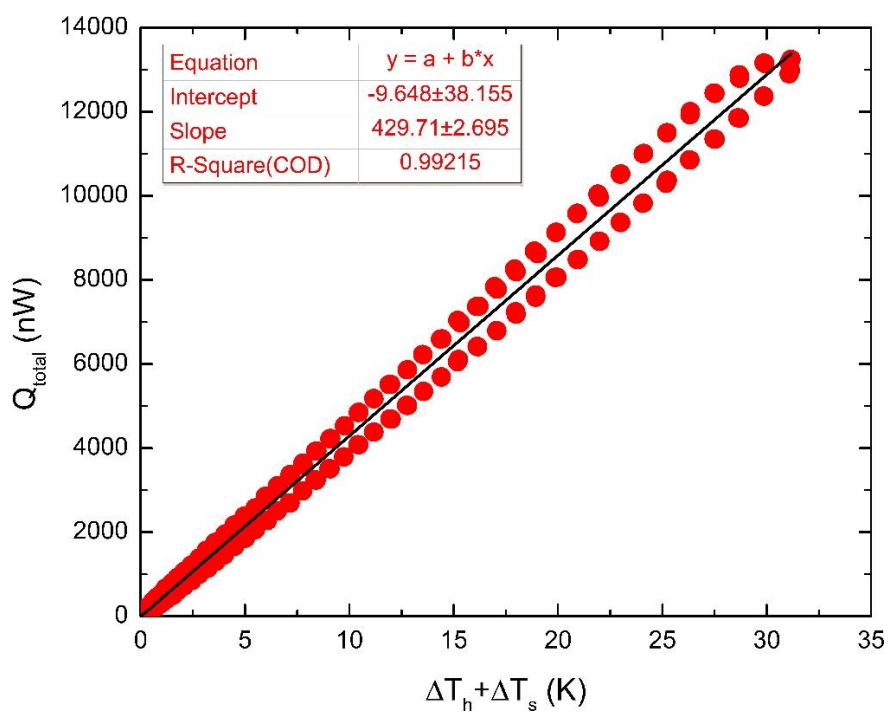


Figure 5-8: Measured total power Q_{total} plotted as a function of $(\Delta T_h + \Delta T_s)$.

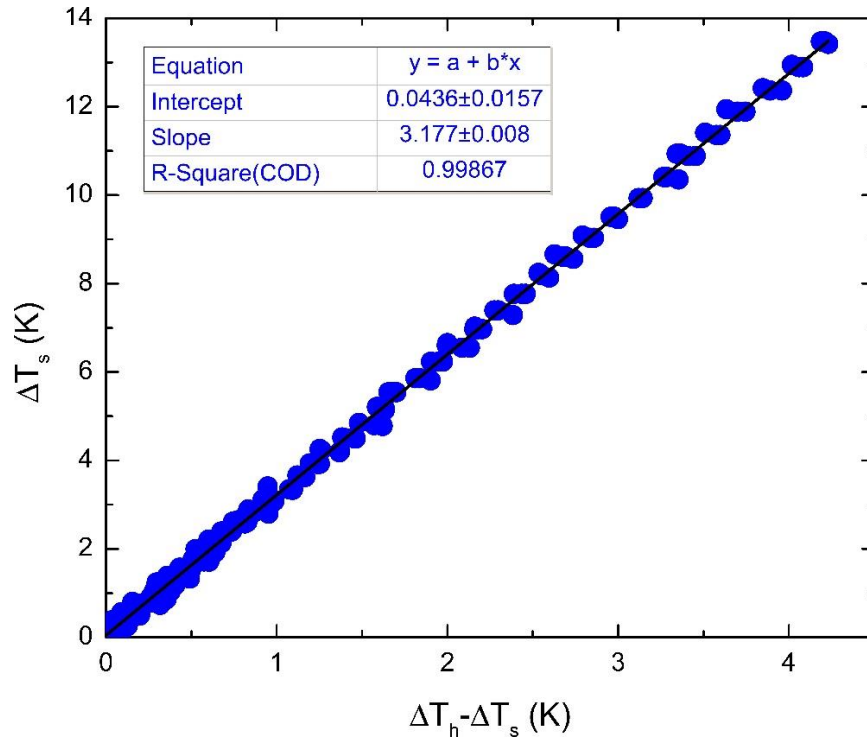


Figure 5-9: Measured ΔT_s plotted as a function of $(\Delta T_h - \Delta T_s)$.

Moreover, another important parameter of nanomaterials, S can be measured with this microdevice. For this measurement, only the four inner Pt electrodes are used. After patterning the Pt electrode on the sample deposited along the central suspended bridge, the supplied heat will flow through the sample from the heating membrane towards sensing or colder membrane. This temperature difference generates a thermoelectric voltage at two ends of the sample (V_{TE}), which is measured between one Pt electrode on the heater side and another on the sensor side. Using the equation, $V_{TE} = S (T_h - T_s)$, the value of S can be determined once the temperatures of the Pt electrodes on the heater side (T_h) and sensor side (T_s) are measured. In addition, this device can also be used to measure the σ based on the four-probe electrical resistances of the Pt electrodes. After determining the parameters

such as κ , S , and σ , another parameter known as the thermoelectric figure of merit (ZT) can also be obtained by:

$$ZT = S^2 \frac{\sigma T}{\kappa} \quad \text{Eq. 5-6}$$

where T is the absolute temperature. Higher ZT is desirable for a higher coefficient of performance (COP) of thermoelectric materials.

5.4 Results and Discussion

After successfully fabricating the suspended beam microdevices, measurement was performed on a bare microdevice to validate our device, setup, and procedure. The suspended bridge is made of SiN_x having a thickness of 500 nm, and its $\kappa_{in-plane}$ was measured for a range of temperatures from 85 K to 460 K. The result obtained was in good agreement with the values mentioned in the literature [245], which is shown in **Figure 5-10**. The room temperature value of the $\kappa_{in-plane}$ obtained in this work was $\sim 3.4 \text{ W m}^{-1} \text{ K}^{-1}$, which is within the range of $2.5 \text{ W m}^{-1} \text{ K}^{-1}$ to $4.5 \text{ W m}^{-1} \text{ K}^{-1}$ as mentioned in most of the cases [217], [246]–[248]. Jain *et al.* [247] observed the value of the $\kappa_{in-plane}$ of a 1.5 μm thick SiN to be $\sim 5 \text{ W m}^{-1} \text{ K}^{-1}$. For a SiN_x of 500 nm, Sultan *et al.* [248] observed the variation of the $\kappa_{in-plane}$ values between $3 \text{ W m}^{-1} \text{ K}^{-1}$ to $4 \text{ W m}^{-1} \text{ K}^{-1}$ for a temperature range of 77 K to 325 K. Zink *et al.* [245] also measured the $\kappa_{in-plane}$ ranging from $0.07 \text{ W m}^{-1} \text{ K}^{-1}$ to $4 \text{ W m}^{-1} \text{ K}^{-1}$ from 3 K to 300 K.

Although our data follows the trend as the temperature drops below room temperature, a deviation can be observed which may be due to the difference in the SiN_x film growth method (LPCVD or plasma-enhanced CVD) and the difference in the thickness of SiN_x film. The major sources of uncertainties were associated with the

accuracy in the measurement of the width and the length of the suspended bridge. An uncertainty of $\pm 0.102 \text{ W m}^{-1} \text{ K}^{-1}$ was obtained by using **Eq. A-1**.

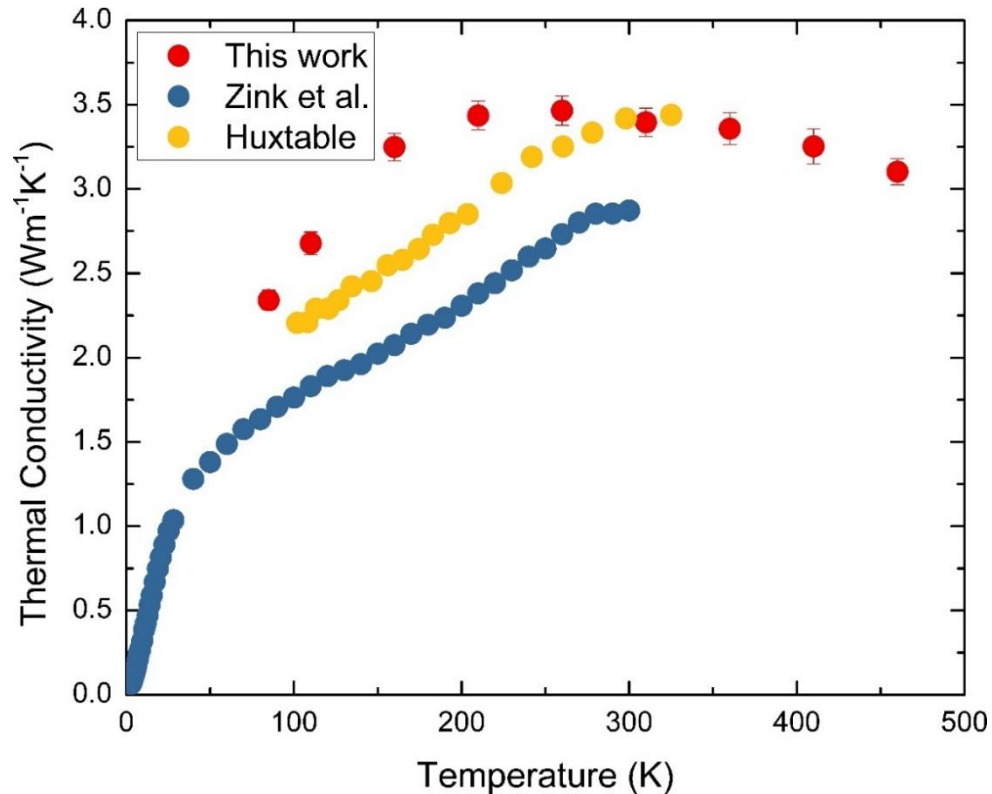


Figure 5-10: Measured κ of a 500 nm thick SiN_x suspended bridge for a range of temperatures along with the values mentioned in the literature [245].

5.5 Conclusion

In this work, a technique was developed for the batch fabrication of the suspended beam microdevices through a standard photolithography process that is very simple, less time-consuming and less expensive than the method used by other research groups in the past that involved complicated and time-consuming steps like EBL. A DC Joule heating approach was used for determining the $\kappa_{in-plane}$ of the central suspended SiN_x (thickness ~ 500 nm) bridge for a temperature range of 85 K- 460 K. The agreement of the temperature

dependent $\kappa_{in-plane}$ values of the suspended bare SiN_x bridge with the values mentioned in the literature validated the setup and the procedure. In addition to the $\kappa_{in-plane}$, other important thermoelectric properties of nanomaterials such as S , σ , ZT can also be measured concurrently from a single microdevice. This shows the multifunctional capability of the suspended beam microdevice fabricated in this work as an effective tool that can ultimately save time that would need individual microdevice otherwise.

CHAPTER 6

CONCLUSIONS AND FUTURE WORK

6.1 Conclusions

This dissertation presented the characterization of nanomaterials as well as techniques for addressing the main objective of thermal management of electronic devices. High power dissipation can affect the device's performance leading to permanent damage which is a case for flexible electronic devices as well. Such issues can be minimized by improving the κ of the substrate materials or the heat spreaders. Depending on the applications, the $\kappa_{in-plane}$ can be enhanced either by adding high AR NWs to different kinds of polymers or by arranging the fillers in anisotropic configurations in order to control the flow of heat in a specific direction. Furthermore, thin films with higher $\kappa_{cross-plane}$ can be used as heat spreaders to take the heat away.

One solution is to enhance the κ of the substrate for spreading the heat efficiently from a localized hot spot. Varying amounts of high aspect ratio Cu NWs synthesized by a solution-based method were mixed with PDMS and PU polymers to form flexible thermally conductive nanocomposites. Intermediate hydrogen annealing treatments were performed on Cu NWs for some selected samples with the intention of removing native surface oxides. The obtained results showed linearly increasing effective κ with loading fraction and a threefold increase in effective κ of the composite was observed at the highest

loading fraction of 4.1 vol. % compared to the neat polymer. Native surface oxides and interfacial thermal resistance were believed to be the factors for limiting the increase in the effective κ of the composites. Even with these limitations, the thermal images of a simulated localized hot spot, as would be experienced by a flexible electronic device, showed that the Cu NW/polymer composites had better heat spreading capability than that of the neat polymers. This suggests that the Cu NW/polymer composites have the potential for use as the substrate for flexible electronics with efficient thermal management capability.

In another work, CNC-PVA composite films with varying internal structures were created and the effect of such variations on the CNC ordering and, hence, on the magnitude and directional dependence of κ of the films were investigated. The composite film with anisotropic configuration showed a $\sim 2.5X$ enhancement in κ in comparison to the isotropic configuration. For such enhancements, CNCs orientation in the heat flow direction in the anisotropic composite films and the role of PVA in filling the voids for forming conductive paths for phonon transport can be major contributors. The κ of our CNC-PVA composite films were $\sim 4-14$ fold higher than that of the plastic films that are commonly used as substrates for flexible electronic devices. Furthermore, the composite films also showed better heat spreading from a localized hot spot as would be experienced by a flexible electronics element. These results suggest that the CNC-PVA composite films can be an eco-friendly alternative to the petroleum-based polymeric materials with thermal management capability in flexible electronic devices.

Next, thermal characterization of the solution-based covalently assembled ND film was performed as a low-cost and greener alternative to the CVD grown ND films for

potential application as heat spreaders in electronic devices. Microfabricated devices were used to measure the $\kappa_{cross-plane}$ of ND film samples of different thicknesses via 3ω method. The sample with the largest thickness showed the $\kappa_{cross-plane}$ as high as $3.50 \pm 0.54 \text{ W m}^{-1} \text{ K}^{-1}$. The $\kappa_{cross-plane}$ values obtained in this work were lower than that of the CVD grown ND films which may be due to lower thickness, higher porosity, and poor interface quality (higher thermal resistance) indicating more room for further improvement.

In the final work, a technique based on standard photolithography process was presented as a simple, low-cost, less time-consuming method for fabricating suspended beam microdevices which could be an alternative to the methods that involved complicated and time-consuming steps like EBL. A DC Joule heating approach was employed to measure the $\kappa_{in-plane}$ of the central suspended bare SiN_x (thickness $\sim 500 \text{ nm}$) bridge for a temperature range of 85 K- 460 K. The temperature dependent $\kappa_{in-plane}$ of the SiN_x was in good agreement with the values mentioned in the literature, thus validating the device, setup, and the experimental procedure. In addition to the $\kappa_{in-plane}$, other important thermoelectric properties of nanomaterials such as S , σ , ZT can also be measured concurrently from a single microdevice which indicates the multifunctional capability of the fabricated device.

6.2 Future Work

Through this work, characterization of nanomaterials, as well as techniques, were presented to address the issue of thermal management in electronic devices. The results obtained from this work showed that there is still room for the improvement. Hence, the following recommendations are suggested for future work:

- A technique is needed to align the Cu NWs in heat flow direction for improving the effective κ of the Cu NW/polymer composites.
- Improvement in the UNCD film coating method is needed so that the porosity decreases with increasing density of the ND particles, thus providing the film with uniform thickness and better κ .
- The sample with a thicker UNCD film is needed since it can provide more reliable data due to low porosity.
- For 3ω measurements, further exploration of the use of substrate materials with lower κ is needed so that the overall voltage signal will be stronger and easier to differentiate from the 1ω signal.
- Perform the $\kappa_{in-plane}$ measurement based on the DC Joule heating approach using the GRTs shown in **Figure 4-3** for ND films to determine the degree of anisotropy.
- A suitable method is required to deposit the nanomaterial samples on the central suspended bridge of the suspended microdevice to study the thermoelectric properties of such samples.

APPENDIX A
UNCERTAINTY ANALYSIS

The total relative uncertainty in each case was calculated as:

$$\text{Total Relative Uncertainty} = \sqrt{\sum_{i=1}^n \left(\frac{\Delta P}{P}\right)_i^2} \quad \text{Eq. A-1}$$

where P is the measured value, ΔP is the uncertainty in the measurement of P and i represents the number of sources of uncertainties.

BIBLIOGRAPHY

- [1] P. Saha, N. Ansari, C. L. Kitchens, W. R. Ashurst, and V. A. Davis, “Microelectromechanical Systems from Aligned Cellulose Nanocrystal Films,” *ACS Appl. Mater. Interfaces*, vol. 10, no. 28, pp. 24116–24123, Jul. 2018.
- [2] S. Yao and Y. Zhu, “Nanomaterial-Enabled Stretchable Conductors: Strategies, Materials and Devices,” *Adv. Mater.*, vol. 27, no. 9, pp. 1480–1511, Mar. 2015.
- [3] P.-C. Chang, S.-Y. Chou, and K.-K. Shieh, “Reading performance and visual fatigue when using electronic paper displays in long-duration reading tasks under various lighting conditions,” *Displays*, vol. 34, no. 3, pp. 208–214, Jul. 2013.
- [4] X. Wang, L. Wang, J. Sun, A. K. Srivastava, V. G. Chigrinov, and H. S. Kwok, “Autostereoscopic 3D pictures on optically rewritable electronic paper,” *J. Soc. Inf. Disp.*, vol. 21, no. 2, pp. 103–107, Feb. 2013.
- [5] T. N. Jackson, Yen-Yi Lin, D. J. Gundlach, and H. Klauk, “Organic thin-film transistors for organic light-emitting flat-panel display backplanes,” *IEEE J. Sel. Top. Quantum Electron.*, vol. 4, no. 1, pp. 100–104, 1998.
- [6] H. Hasegawa *et al.*, “Selective recovery of indium from the etching waste solution of the flat-panel display fabrication process,” *Microchem. J.*, vol. 110, pp. 133–139, Sep. 2013.
- [7] K. Jost *et al.*, “Knitted and screen printed carbon-fiber supercapacitors for applications in wearable electronics,” *Energy Environ. Sci.*, vol. 6, no. 9, p. 2698, Aug. 2013.
- [8] M. Stoppa, A. Chiolerio, M. Stoppa, and A. Chiolerio, “Wearable Electronics and Smart Textiles: A Critical Review,” *Sensors*, vol. 14, no. 7, pp. 11957–11992, Jul. 2014.
- [9] X. Liu, Y. Z. Long, L. Liao, X. Duan, and Z. Fan, “Large-scale integration of semiconductor nanowires for high-performance flexible electronics,” *ACS Nano*, vol. 6, no. 3, pp. 1888–1900, 2012.
- [10] S. Cai *et al.*, “Review on flexible photonics/electronics integrated devices and fabrication strategy,” *Sci. China Inf. Sci.*, vol. 61, no. 6, p. 060410, Jun. 2018.

- [11] C. K. Chiang *et al.*, “Electrical Conductivity in Doped Polyacetylene,” *Phys. Rev. Lett.*, vol. 39, no. 17, pp. 1098–1101, Oct. 1977.
- [12] A. Tsumura, H. Koezuka, and T. Ando, “Macromolecular electronic device: Field-effect transistor with a polythiophene thin film,” *Appl. Phys. Lett.*, vol. 49, no. 18, pp. 1210–1212, Nov. 1986.
- [13] C. W. Tang and S. A. VanSlyke, “Organic electroluminescent diodes,” *Appl. Phys. Lett.*, vol. 51, no. 12, pp. 913–915, Sep. 1987.
- [14] G. Horowitz, X.-Z. Peng, D. Fichou, and F. Garnier, “Role of the semiconductor/insulator interface in the characteristics of π -conjugated-oligomer-based thin-film transistors,” *Synth. Met.*, vol. 51, no. 1–3, pp. 419–424, Sep. 1992.
- [15] R. J. O. M. Hoofman, M. P. de Haas, L. D. A. Siebbeles, and J. M. Warman, “Highly mobile electrons and holes on isolated chains of the semiconducting polymer poly(phenylene vinylene),” *Nature*, vol. 392, no. 6671, pp. 54–56, Mar. 1998.
- [16] M. Uno *et al.*, “High-Speed Flexible Organic Field-Effect Transistors with a 3D Structure,” *Adv. Mater.*, vol. 23, no. 27, pp. 3047–3051, Jul. 2011.
- [17] B. Gburek and V. Wagner, “Influence of the semiconductor thickness on the charge carrier mobility in P3HT organic field-effect transistors in top-gate architecture on flexible substrates,” *Org. Electron.*, vol. 11, no. 5, pp. 814–819, May 2010.
- [18] Y. Park *et al.*, “High performance n-type organic–inorganic nanohybrid semiconductors for flexible electronic devices,” *Org. Electron.*, vol. 12, no. 2, pp. 348–352, Feb. 2011.
- [19] N. Kawasaki *et al.*, “Flexible picene thin film field-effect transistors with parylene gate dielectric and their physical properties,” *Appl. Phys. Lett.*, vol. 96, no. 11, p. 113305, Mar. 2010.
- [20] Y. Sun, W. M. Choi, H. Jiang, Y. Y. Huang, and J. A. Rogers, “Controlled buckling of semiconductor nanoribbons for stretchable electronics,” *Nat. Nanotechnol.*, vol. 1, no. 3, pp. 201–207, Dec. 2006.
- [21] J.-H. Ahn *et al.*, “Bendable integrated circuits on plastic substrates by use of printed ribbons of single-crystalline silicon,” *Appl. Phys. Lett.*, vol. 90, no. 21, p. 213501, May 2007.
- [22] D.-H. Kim *et al.*, “Materials and noncoplanar mesh designs for integrated circuits with linear elastic responses to extreme mechanical deformations,” *Proc. Natl. Acad. Sci. U. S. A.*, vol. 105, no. 48, pp. 18675–80, Dec. 2008.
- [23] H. C. Ko *et al.*, “Curvilinear Electronics Formed Using Silicon Membrane Circuits and Elastomeric Transfer Elements,” *Small*, vol. 5, no. 23, pp. 2703–2709, Dec. 2009.

- [24] D.-H. Kim, J. Xiao, J. Song, Y. Huang, and J. A. Rogers, "Stretchable, Curvilinear Electronics Based on Inorganic Materials," *Adv. Mater.*, vol. 22, no. 19, pp. 2108–2124, Jan. 2010.
- [25] Y. Ma, X. Feng, J. A. Rogers, Y. Huang, and Y. Zhang, "Design and application of 'J-shaped' stress–strain behavior in stretchable electronics: a review," *Lab Chip*, vol. 17, no. 10, pp. 1689–1704, May 2017.
- [26] M. A. Meitl *et al.*, "Transfer printing by kinetic control of adhesion to an elastomeric stamp," *Nat. Mater.*, vol. 5, no. 1, pp. 33–38, Jan. 2006.
- [27] A. J. Baca *et al.*, "Semiconductor Wires and Ribbons for High- Performance Flexible Electronics," *Angew. Chemie Int. Ed.*, vol. 47, no. 30, pp. 5524–5542, Jul. 2008.
- [28] X. Feng, M. A. Meitl, A. M. Bowen, Y. Huang, R. G. Nuzzo, and J. A. Rogers, "Competing fracture in kinetically controlled transfer printing," *Langmuir*, vol. 23, no. 25, pp. 12555–12560, 2007.
- [29] S. Kim *et al.*, "Microstructured elastomeric surfaces with reversible adhesion and examples of their use in deterministic assembly by transfer printing," *Proc. Natl. Acad. Sci. U. S. A.*, vol. 107, no. 40, pp. 17095–100, Oct. 2010.
- [30] Y. Huang *et al.*, "Direct Laser Writing-Based Programmable Transfer Printing via Bioinspired Shape Memory Reversible Adhesive," *ACS Appl. Mater. Interfaces*, vol. 8, no. 51, pp. 35628–35633, Dec. 2016.
- [31] H. Chen, X. Feng, Y. Huang, Y. Huang, and J. A. Rogers, "Experiments and viscoelastic analysis of peel test with patterned strips for applications to transfer printing," *J. Mech. Phys. Solids*, vol. 61, no. 8, pp. 1737–1752, Aug. 2013.
- [32] S. Cai *et al.*, "Surface evolution and stability transition of silicon wafer subjected to nano-diamond grinding," *AIP Adv.*, vol. 7, no. 3, p. 035221, Mar. 2017.
- [33] A. J. McNamara, Y. Joshi, and Z. M. Zhang, "Characterization of nanostructured thermal interface materials - A review," *Int. J. Therm. Sci.*, vol. 62, pp. 2–11, 2012.
- [34] L.-T. Yeh and R. C. Chu, *Thermal Management of Microelectronic Equipment*. New York: ASME Press, 2002.
- [35] G. E. Moore, "Cramming more components onto integrated circuits (Reprinted from Electronics, pg 114-117, April 19, 1965)," *Proc. Ieee*, vol. 86, no. 1, pp. 82–85, 1965.
- [36] I. Ferain, C. A. Colinge, and J. P. Colinge, "Multigate transistors as the future of classical metal-oxide-semiconductor field-effect transistors," *Nature*, vol. 479, no. 7373, pp. 310–316, 2011.

- [37] V. Vishwakarma, C. Waghela, and A. Jain, "Measurement of out-of-plane thermal conductivity of substrates for flexible electronics and displays," *Microelectron. Eng.*, vol. 142, pp. 36–39, Jul. 2015.
- [38] N. Balachander *et al.*, "Nanowire-filled polymer composites with ultrahigh thermal conductivity," *Appl. Phys. Lett.*, vol. 102, no. 9, p. 093117, Mar. 2013.
- [39] G. H. Gelinck *et al.*, "Flexible active-matrix displays and shift registers based on solution-processed organic transistors," *Nat. Mater.*, vol. 3, no. 2, pp. 106–110, Feb. 2004.
- [40] L. Zhou, A. Wanga, S.-C. Wu, J. Sun, S. Park, and T. N. Jackson, "All-organic active matrix flexible display," *Appl. Phys. Lett.*, vol. 88, no. 8, p. 083502, Feb. 2006.
- [41] M. Zirkl *et al.*, "Low-Voltage Organic Thin-Film Transistors with High-k Nanocomposite Gate Dielectrics for Flexible Electronics and Optothermal Sensors," *Adv. Mater.*, vol. 19, no. 17, pp. 2241–2245, Sep. 2007.
- [42] K.-T. Cheng and T.-C. Huang, "Design for Low Power and Reliable Flexible Electronics: Self-Tunable Cell-Library Design," *J. Disp. Technol. Vol. 5, Issue 6*, pp. 206–215, vol. 5, no. 6, pp. 206–215, Jun. 2009.
- [43] A. L. Moore and L. Shi, "Emerging challenges and materials for thermal management of electronics," *Materials Today*, vol. 17, no. 4, pp. 163–174, 2014.
- [44] P. E. Slade and L. T. Jenkins, *Techniques and methods of polymer evaluation: Thermal Characterization Techniques*. NY: Marcel Dekker, Inc, 1970.
- [45] D. L. Rule, D. R. Smith, and L. L. Sparks, "Thermal conductivity of a polyimide film between 4.2 and 300K, with and without alumina particles as filler," *Film*, no. August, p. 66, 1990.
- [46] P. Yi, R. a Awang, W. S. T. Rowe, K. Kalantar-zadeh, and K. Khoshmanesh, "PDMS nanocomposites for heat transfer enhancement in microfluidic platforms.," *Lab Chip*, vol. 14, no. 17, pp. 3419–26, 2014.
- [47] C. J. Glassbrenner and G. A. Slack, "Thermal conductivity of silicon and germanium from 3K to the melting point," *Phys. Rev.*, vol. 134, no. 4A, pp. A1058–A1069, 1964.
- [48] H. R. Shanks, P. D. Maycock, P. H. Sidles, and G. C. Danielson, "Thermal conductivity of silicon from 300 to 1400 K," *Phys. Rev.*, vol. 130, no. 5, pp. 1743–1748, 1963.
- [49] A. E. Aliev, M. H. Lima, E. M. Silverman, and R. H. Baughman, "Thermal conductivity of multi-walled carbon nanotube sheets: radiation losses and quenching of phonon modes," *Nanotechnology*, vol. 21, no. 3, p. 035709, Jan. 2010.

- [50] Y. Zhou *et al.*, “Recyclable organic solar cells on cellulose nanocrystal substrates,” *Sci. Rep.*, vol. 3, p. 1536, 2013.
- [51] Y. H. Jung *et al.*, “High-performance green flexible electronics based on biodegradable cellulose nanofibril paper,” *Nat. Commun.*, vol. 6, no. 1, p. 7170, Dec. 2015.
- [52] F. Eder, H. Klauk, M. Halik, U. Zschieschang, G. Schmid, and C. Dehm, “Organic electronics on paper,” *Appl. Phys. Lett.*, vol. 84, no. 14, pp. 2673–2675, Apr. 2004.
- [53] Y.-H. Kim, D.-G. Moon, and J.-I. Han, “Organic TFT Array on a Paper Substrate,” *IEEE Electron Device Lett.*, vol. 25, no. 10, pp. 702–704, Oct. 2004.
- [54] H. Zhu, Z. Fang, C. Preston, Y. Li, and L. Hu, “Transparent paper: fabrications, properties, and device applications,” *Energy Environ. Sci.*, vol. 7, no. 1, pp. 269–287, Dec. 2014.
- [55] M. Nogi and H. Yano, “Transparent Nanocomposites Based on Cellulose Produced by Bacteria Offer Potential Innovation in the Electronics Device Industry,” *Adv. Mater.*, vol. 20, no. 10, pp. 1849–1852, May 2008.
- [56] H. Zhu *et al.*, “Biodegradable transparent substrates for flexible organic-light-emitting diodes,” *Energy Environ. Sci.*, vol. 6, no. 7, p. 2105, Jun. 2013.
- [57] H. Zhu *et al.*, “Highly Thermally Conductive Papers with Percolative Layered Boron Nitride Nanosheets,” *ACS Nano*, vol. 8, no. 4, pp. 3606–3613, Apr. 2014.
- [58] K. Gao *et al.*, “Cellulose nanofiber–graphene all solid-state flexible supercapacitors,” *J. Mater. Chem. A*, vol. 1, no. 1, pp. 63–67, Nov. 2013.
- [59] G. Siqueira, J. Bras, and A. Dufresne, “Cellulosic bionanocomposites: A review of preparation, properties and applications,” *Polymers*, vol. 2, no. 4, pp. 728–765, 2010.
- [60] A. Isogai, “Wood nanocelluloses: Fundamentals and applications as new bio-based nanomaterials,” *Journal of Wood Science*, vol. 59, no. 6, pp. 449–459, 2013.
- [61] R. A. Chowdhury, C. Clarkson, and J. Youngblood, “Continuous roll-to-roll fabrication of transparent cellulose nanocrystal (CNC) coatings with controlled anisotropy,” *Cellulose*, vol. 25, no. 3, pp. 1769–1781, 2018.
- [62] Itrs, “International Technology Roadmap for Semiconductors, Executive Summary,” *Itrs*, 2011.
- [63] M. Shamsa, S. Ghosh, I. Calizo, V. Ralchenko, A. Popovich, and A. A. Balandin, “Thermal conductivity of nitrogenated ultrananocrystalline diamond films on silicon,” *J. Appl. Phys.*, vol. 103, no. 8, 2008.

- [64] E. Pop and K. E. Goodson, "Thermal Phenomena in Nanoscale Transistors," *J. Electron. Packag.*, vol. 128, no. 2, p. 102, 2006.
- [65] R. Mahajan, C. P. Chiu, and G. Chrysler, "Cooling a microprocessor chip," *Proc. IEEE*, vol. 94, no. 8, pp. 1476–1485, 2006.
- [66] N. Stojanovic, D. H. S. Maithripala, J. M. Berg, and M. Holtz, "Thermal conductivity in metallic nanostructures at high temperature : Electrons , phonons , and the Wiedemann-Franz law," *Phys. Rev. B*, vol. 82, no. 7, pp. 1–9, 2010.
- [67] H. F. Hamann *et al.*, "Hotspot-limited microprocessors: Direct temperature and power distribution measurements," *IEEE J. Solid-State Circuits*, vol. 42, no. 1, pp. 56–64, 2007.
- [68] L. Shi *et al.*, "Measuring Thermal and Thermoelectric Properties of One-Dimensional Nanostructures Using a Microfabricated Device," *J. Heat Transfer*, 2003.
- [69] T. S. Tighe, J. M. Worlock, and M. L. Roukes, "Direct thermal conductance measurements on suspended monocrystalline nanostructures," *Appl. Phys. Lett.*, vol. 70, no. 20, pp. 2687–2689, 1997.
- [70] L. Shi *et al.*, "Measuring Thermal and Thermoelectric Properties of One-Dimensional Nanostructures Using a Microfabricated Device," *J. Heat Transfer*, vol. 125, no. October, p. 881, 2003.
- [71] P. Kim, L. Shi, A. Majumdar, and P. L. McEuen, "Thermal transport measurements of individual multiwalled nanotubes," *Phys. Rev. Lett.*, vol. 87, no. 21, p. 215502, 2001.
- [72] A. Rai and A. L. Moore, "Enhanced thermal conduction and influence of interfacial resistance within flexible high aspect ratio copper nanowire/polymer composites," *Compos. Sci. Technol.*, vol. 144, pp. 70–78, May 2017.
- [73] P. Lee *et al.*, "Highly Stretchable and Highly Conductive Metal Electrode by Very Long Metal Nanowire Percolation Network," *Adv. Mater.*, vol. 24, no. 25, pp. 3326–3332, Jul. 2012.
- [74] L. C. Sim, S. R. Ramanan, H. Ismail, K. N. Seetharamu, and T. J. Goh, "Thermal characterization of Al₂O₃ and ZnO reinforced silicone rubber as thermal pads for heat dissipation purposes," *Thermochim. Acta*, vol. 430, no. 1–2, pp. 155–165, 2005.
- [75] K. Pashayi, H. R. Fard, F. Lai, S. Iruvanti, J. Plawsky, and T. Borca-Tasciuc, "High thermal conductivity epoxy-silver composites based on self-constructed nanostructured metallic networks," in *Journal of Applied Physics*, 2012, vol. 111, no. 10.
- [76] S. Nikkeshi, M. Kudo, and T. Masuko, "Dynamic viscoelastic properties and

- thermal properties of Ni powder-epoxy resin composites,” *J. Appl. Polym. Sci.*, vol. 69, no. 13, pp. 2593–2598, 1998.
- [77] S. Wang, Y. Cheng, R. Wang, J. Sun, and L. Gao, “Highly thermal conductive copper nanowire composites with ultralow loading: Toward applications as thermal interface materials,” in *ACS Applied Materials and Interfaces*, 2014, vol. 6, no. 9, pp. 6481–6486.
- [78] A. E. Aliev, M. H. Lima, E. M. Silverman, and R. H. Baughman, “Thermal conductivity of multi-walled carbon nanotube sheets: Radiation losses and quenching of phonon modes,” *Nanotechnology*, vol. 21, no. 3, 2010.
- [79] C. Mayousse, C. Celle, A. Carella, and J.-P. Simonato, “Synthesis and purification of long copper nanowires. Application to high performance flexible transparent electrodes with and without PEDOT:PSS,” *Nano Res.*, vol. 7, no. 3, pp. 315–324, 2014.
- [80] J. Song, J. Li, J. Xu, and H. Zeng, “Superstable transparent conductive Cu@Cu₄Ni nanowire elastomer composites against oxidation, bending, stretching, and twisting for flexible and stretchable optoelectronics,” *Nano Lett.*, vol. 14, no. 11, pp. 6298–6305, 2014.
- [81] H. Guo *et al.*, “Copper Nanowires as Fully Transparent Conductive Electrodes,” *Sci. Rep.*, vol. 3, Jul. 2013.
- [82] J. Chen *et al.*, “Solution-processed copper nanowire flexible transparent electrodes with PEDOT:PSS as binder, protector and oxide-layer scavenger for polymer solar cells,” *Nano Res.*, vol. 8, no. 3, pp. 1017–1025, 2015.
- [83] V. A. Korada, V. K. R. R, K. Ps, and S. P. Singh, “Copper Conductive Inks: Synthesis and its Utilization in Flexible Electronics,” *RSC Adv.*, vol. 5, pp. 63985–64030, 2015.
- [84] J. W. Borchert, I. E. Stewart, S. Ye, A. R. Rathmell, B. J. Wiley, and K. I. Winey, “Effects of length dispersity and film fabrication on the sheet resistance of copper nanowire transparent conductors,” *Nanoscale*, vol. 7, no. 34, pp. 14496–504, 2015.
- [85] G. a. Gelves, M. H. Al-Saleh, and U. Sundararaj, “Highly electrically conductive and high performance EMI shielding nanowire/polymer nanocomposites by miscible mixing and precipitation,” *J. Mater. Chem.*, vol. 21, no. 3, p. 829, 2011.
- [86] S. Ye, A. R. Rathmell, Z. Chen, I. E. Stewart, and B. J. Wiley, “Metal nanowire networks: The next generation of transparent conductors,” *Adv. Mater.*, vol. 26, no. 39, pp. 6670–6687, 2014.
- [87] M. T. Barako *et al.*, “Thermal Conduction in Vertically Aligned Copper Nanowire Arrays and Composites,” *ACS Appl. Mater. Interfaces*, vol. 7, no. 34, pp. 19251–19259, 2015.

- [88] S. Li, Y. Chen, L. Huang, and D. Pan, "Large-scale synthesis of well-dispersed copper nanowires in an electric pressure cooker and their application in transparent and conductive networks," *Inorg. Chem.*, vol. 53, no. 9, pp. 4440–4444, 2014.
- [89] Y. Tang, L. Yeo, Y. Chen, W. Yap, and W. Cheng, "Ultralow-density copper nanowire aerogel monoliths with tunable mechanical and electrical properties," *J. Mater. Chem. A*, vol. 1, no. 23, pp. 6723–6726, 2013.
- [90] Y. Tang, S. Gong, Y. Chen, L. W. Yap, and W. Cheng, "Manufacturable conducting rubber ambers and stretchable conductors from copper nanowire aerogel monoliths," *ACS Nano*, vol. 8, no. 6, pp. 5707–5714, 2014.
- [91] L. Hu, H. Wu, and Y. Cui, "Metal nanogrids, nanowires, and nanofibers for transparent electrodes," *MRS Bull.*, vol. 36, no. 10, pp. 760–765, Oct. 2011.
- [92] F. Cui *et al.*, "Synthesis of Ultrathin Copper Nanowires Using Tris(trimethylsilyl)silane for High-Performance and Low-Haze Transparent Conductors," *Nano Lett.*, vol. 15, no. 11, pp. 7610–7615, 2015.
- [93] C.-W. Nan, G. Liu, Y. Lin, and M. Li, "Interface effect on thermal conductivity of carbon nanotube composites," *Appl. Phys. Lett.*, vol. 85, no. 16, p. 3549, 2004.
- [94] F. Macedo and J. A. Ferreira, "Thermal contact resistance evaluation in polymer-based carbon fiber composites," in *Review of Scientific Instruments*, 2003, vol. 74, no. 1 II, pp. 828–830.
- [95] S. Shenogin, A. Bodapati, L. Xue, R. Ozisik, and P. Keblinski, "Effect of chemical functionalization on thermal transport of carbon nanotube composites," *Appl. Phys. Lett.*, vol. 85, no. 12, pp. 2229–2231, 2004.
- [96] M. B. Bryning, D. E. Milkie, M. F. Islam, J. M. Kikkawa, and A. G. Yodh, "Thermal conductivity and interfacial resistance in single-wall carbon nanotube epoxy composites," *Appl. Phys. Lett.*, vol. 87, no. 16, pp. 1–3, 2005.
- [97] Q. Z. Xue, "Model for the effective thermal conductivity of carbon nanotube composites," *Nanotechnology*, vol. 17, no. April, pp. 1655–1660, 2006.
- [98] G. Steinlesberger and M. Engelhardt, "Size-dependent resistivity of metallic wires in the mesoscopic range," *Phys. Rev. B*, vol. 66, no. 7, pp. 1–4, 2002.
- [99] W. Steinhögl, G. Schindler, G. Steinlesberger, M. Traving, and M. Engelhardt, "Comprehensive study of the resistivity of copper wires with lateral dimensions of 100 nm and smaller," *J. Appl. Phys.*, vol. 023706, pp. 1–8, 2005.
- [100] Z. Han and A. Fina, "Thermal conductivity of carbon nanotubes and their polymer nanocomposites: A review," *Prog. Polym. Sci.*, vol. 36, no. 7, pp. 914–944, 2011.
- [101] S. Benli, U. Yilmazer, F. Pekel, and S. Ozkar, "Effect of fillers on thermal and

- mechanical properties of polyurethane elastomer,” *J. Appl. Polym. Sci.*, vol. 68, no. 7, pp. 1057–1065, 1998.
- [102] A. Munari, J. Xu, E. Dalton, A. Mathewson, and K. M. Razeeb, “Metal nanowire-polymer nanocomposite as thermal interface material,” *Proc. - Electron. Components Technol. Conf.*, pp. 448–452, 2009.
- [103] M. J. Biercuk, M. C. Llaguno, M. Radosavljevic, J. K. Hyun, A. T. Johnson, and J. E. Fischer, “Carbon nanotube composites for thermal management,” *Appl. Phys. Lett.*, vol. 80, no. 15, pp. 2767–2769, 2002.
- [104] K. M. F. Shahil and A. A. Balandin, “Graphene-multilayer graphene nanocomposites as highly efficient thermal interface materials,” *Nano Lett.*, vol. 12, no. 2, pp. 861–867, 2012.
- [105] A. R. J. Hussain, A. A. Alahyari, S. A. Eastman, C. Thibaud-Erkey, S. Johnston, and M. J. Sobkowicz, “Review of polymers for heat exchanger applications: Factors concerning thermal conductivity,” *Appl. Therm. Eng.*, vol. 113, pp. 1118–1127, Feb. 2017.
- [106] C. Hongyu, Chen, V, V, Ginzburg, J, Yang, Y, Yang, W, Liu, Y, HuangL, Du, B, Chen, Hongyu, Chen, V, V, Ginzburg, J, Yang, Y, Yang, W, Liu, Y, HuangL, Du, B, “Thermal conductivity of polymer-based composites: Fundamentals and applications,” *Prog. Polym. Sci.*, vol. progress i, no. progress in press, pp. 1–45, 2016.
- [107] H. Zhu *et al.*, “Biodegradable transparent substrates for flexible organic-light-emitting diodes,” *Energy Environ. Sci.*, vol. 6, no. 7, p. 2105, 2013.
- [108] J. A. Diaz *et al.*, “Thermal conductivity in nanostructured films: From single cellulose nanocrystals to bulk films,” *Biomacromolecules*, vol. 15, no. 11, pp. 4096–4101, 2014.
- [109] H. C. Kim, S. Mun, H. U. Ko, L. Zhai, A. Kafy, and J. Kim, “Renewable smart materials,” *Smart Materials and Structures*, vol. 25, no. 7. 2016.
- [110] R. J. Moon, A. Martini, J. Nairn, J. Simonsen, and J. Youngblood, “Cellulose nanomaterials review: structure, properties and nanocomposites,” *Chem. Soc. Rev.*, vol. 40, no. 7, pp. 3941–3994, Jun. 2011.
- [111] P. Ball, “Material witness: In praise of wood,” *Nat. Mater.*, vol. 4, no. 7, p. 515, 2005.
- [112] D. Klemm, B. Heublein, H. P. Fink, and A. Bohn, “Cellulose: Fascinating biopolymer and sustainable raw material,” *Angewandte Chemie - International Edition*, vol. 44, no. 22. pp. 3358–3393, 2005.
- [113] J. H. Kim *et al.*, “Review of nanocellulose for sustainable future materials,”

International Journal of Precision Engineering and Manufacturing - Green Technology, vol. 2, no. 2. pp. 197–213, 2015.

- [114] A. C. OSullivan, “Cellulose: the structure slowly unravels,” *Cellulose*, vol. 4, no. 3, pp. 173–207, 1997.
- [115] M. a. Hubbe, O. J. Rojas, L. a. Lucia, and M. Sain, “Cellulosic Nanocomposites: a Review,” *BioResources*, vol. 3, no. 3, pp. 929–980, 2008.
- [116] R. A. Chowdhury, S. X. Peng, and J. Youngblood, “Improved order parameter (alignment) determination in cellulose nanocrystal (CNC) films by a simple optical birefringence method,” *Cellulose*, vol. 24, no. 5, pp. 1957–1970, 2017.
- [117] G. Siqueira, J. Bras, and A. Dufresne, “Cellulosic Bionanocomposites: A Review of Preparation, Properties and Applications,” *Polymers (Basel)*, vol. 2, no. 4, pp. 728–765, Dec. 2010.
- [118] J. C. Liu, D. J. Martin, R. J. Moon, and J. P. Youngblood, “Enhanced thermal stability of biomedical thermoplastic polyurethane with the addition of cellulose nanocrystals,” *J. Appl. Polym. Sci.*, vol. 132, no. 22, 2015.
- [119] S. X. Peng, R. J. Moon, and J. P. Youngblood, “Design and characterization of cellulose nanocrystal-enhanced epoxy hardeners,” *Green Mater.*, vol. 2, no. 4, pp. 193–205, 2014.
- [120] Y. Yoo and J. P. Youngblood, “Tung Oil Wood Finishes with Improved Weathering, Durability, and Scratch Performance by Addition of Cellulose Nanocrystals,” *ACS Appl. Mater. Interfaces*, vol. 9, no. 29, pp. 24936–24946, 2017.
- [121] Y. Zhou *et al.*, “Efficient recyclable organic solar cells on cellulose nanocrystal substrates with a conducting polymer top electrode deposited by film-transfer lamination,” *Org. Electron. physics, Mater. Appl.*, vol. 15, no. 3, pp. 661–666, 2014.
- [122] N. Lavoine, I. Desloges, A. Dufresne, and J. Bras, “Microfibrillated Cellulose - Its Barrier Properties and Applications in Cellulosic Materials: a review,” *Carbohydr Polym*, vol. 90, no. 2, pp. 735–764, 2012.
- [123] C. Chindawong and D. Johannsmann, “An anisotropic ink based on crystalline nanocellulose: Potential applications in security printing,” *J. Appl. Polym. Sci.*, vol. 131, no. 22, 2014.
- [124] Y. Yoo, C. Martinez, and J. P. Youngblood, “Sustained Dye Release Using Poly(urea–urethane)/Cellulose Nanocrystal Composite Microcapsules,” *Langmuir*, vol. 33, no. 6, pp. 1521–1532, Feb. 2017.
- [125] A. B. Reising, R. J. Moon, and J. P. Youngblood, “Effect of particle alignment on mechanical properties of neat cellulose nanocrystal films,” *J-FOR*, vol. 2, no. 6, pp. 32–41, 2012.

- [126] X. Yang and E. D. Cranston, "Chemically cross-linked cellulose nanocrystal aerogels with shape recovery and superabsorbent properties," *Chem. Mater.*, vol. 26, no. 20, pp. 6016–6025, 2014.
- [127] R. J. Moon, A. Martini, J. Nairn, J. Simonsen, and J. Youngblood, "Cellulose nanomaterials review: structure, properties and nanocomposites," *Chem Soc Rev*, vol. 40, no. 7, pp. 3941–3994, 2011.
- [128] V. Khoshkava and M. R. Kamal, "Effect of surface energy on dispersion and mechanical properties of polymer/nanocrystalline cellulose nanocomposites," *Biomacromolecules*, vol. 14, no. 9, pp. 3155–3163, 2013.
- [129] E. Chiellini, A. Corti, S. D'Antone, and R. Solaro, "Biodegradation of poly (vinyl alcohol) based materials," *Prog. Polym. Sci.*, vol. 28, no. 6, pp. 963–1014, 2003.
- [130] C. Z. Kibédi-Szabó *et al.*, "Biodegradation Behavior of Composite Films with Poly (Vinyl Alcohol) Matrix," *J. Polym. Environ.*, vol. 20, no. 2, pp. 422–430, 2011.
- [131] P. Alexy *et al.*, "Effect of melt processing on thermo-mechanical degradation of poly(vinyl alcohol)s," *Polym. Degrad. Stab.*, vol. 85, no. 2, pp. 823–830, 2004.
- [132] S. I. Song and B. C. Kim, "Characteristic rheological features of PVA solutions in water-containing solvents with different hydration states," *Polymer (Guildf.)*, vol. 45, no. 7, pp. 2381–2386, 2004.
- [133] S. S. Kim *et al.*, "Rheological properties of water solutions of syndiotactic poly(vinyl alcohol) of different molecular weights," *J. Appl. Polym. Sci.*, vol. 92, no. 3, pp. 1426–1431, 2004.
- [134] M. Roohani, Y. Habibi, N. M. Belgacem, G. Ebrahim, A. N. Karimi, and A. Dufresne, "Cellulose whiskers reinforced polyvinyl alcohol copolymers nanocomposites," *Eur. Polym. J.*, vol. 44, no. 8, pp. 2489–2498, 2008.
- [135] M. Flieger, M. Kantorová, A. Prell, T. Řezanka, and J. Votruba, "Biodegradable plastics from renewable sources," *Folia Microbiol. (Praha)*, vol. 48, no. 1, p. 27, 2003.
- [136] Z. Jahan, M. B. K. Niazi, and Ø. W. Gregersen, "Mechanical, thermal and swelling properties of cellulose nanocrystals/PVA nanocomposites membranes," *J. Ind. Eng. Chem.*, vol. 57, pp. 113–124, 2018.
- [137] L. Deng and M.-B. Hägg, "Swelling behavior and gas permeation performance of PVAm/PVA blend FSC membrane," *J. Memb. Sci.*, vol. 363, no. 1, pp. 295–301, 2010.
- [138] E. H. Qua, P. R. Hornsby, H. S. S. Sharma, G. Lyons, and R. D. McCall, "Preparation and characterization of poly (vinyl alcohol) nanocomposites made from cellulose nanofibers," *J. Appl. Polym. Sci.*, vol. 113, pp. 2283–2247, 2009.

- [139] A. J. Uddin, J. Araki, and Y. Gotoh, "Toward 'Strong' sreen nanocomposites: Polyvinyl alcohol reinforced with extremely oriented cellulose whiskers," *Biomacromolecules*, vol. 12, no. 3, pp. 617–624, 2011.
- [140] N. a Peppas and E. W. Merrill, "Poly(vinyl alcohol) hydrogels: Reinforcement of radiation-crosslinked networks by crystallization," *J. Polym. Sci. Polym. Chem. Ed.*, vol. 14, no. 2, pp. 441–457, 1976.
- [141] Y. Shimazaki *et al.*, "Excellent Thermal Conductivity of Transparent Cellulose Nanofiber/Epoxy Resin Nanocomposites," *Biomacromolecules*, vol. 8, no. 9, pp. 2976–2978, Sep. 2007.
- [142] E. Bahar *et al.*, "Thermal and mechanical properties of polypropylene nanocomposite materials reinforced with cellulose nano whiskers," *J. Appl. Polym. Sci.*, vol. 125, no. 4, pp. 2882–2889, 2012.
- [143] K. Uetani, T. Okada, and H. T. Oyama, "Crystallite size effect on thermal conductive properties of nonwoven nanocellulose sheets," *Biomacromolecules*, vol. 16, no. 7, pp. 2220–2227, 2015.
- [144] K. Uetani, T. Okada, and H. T. Oyama, "Thermally conductive and optically transparent flexible films with surface-exposed nanocellulose skeletons," *J. Mater. Chem. C*, vol. 4, no. 41, pp. 9697–9703, 2016.
- [145] K. Uetani, T. Okada, and H. T. Oyama, "In-Plane Anisotropic Thermally Conductive Nanopapers by Drawing Bacterial Cellulose Hydrogels," *ACS Macro Lett.*, vol. 6, no. 4, pp. 345–349, 2017.
- [146] H. G. Chae and S. Kumar, "Making Strong Fibers," *Science (80-.)*, vol. 319, no. 5865, p. 908 LP-909, Feb. 2008.
- [147] D. B. Mergenthaler, M. Pietralla, H. G. Kilian, and S. Roy, "Thermal Conductivity in Ultraoriented Polyethylene," *Macromolecules*, vol. 25, no. 13, pp. 3500–3502, 1992.
- [148] C. L. Choy, Y. W. Wong, G. W. Yang, and T. Kanamoto, "Elastic modulus and thermal conductivity of ultradrawn polyethylene," *J. Polym. Sci. Part B Polym. Phys.*, vol. 37, no. 23, pp. 3359–3367, 1999.
- [149] X. Wang, V. Ho, R. A. Segalman, and D. G. Cahill, "Thermal conductivity of high-modulus polymer fibers," *Macromolecules*, vol. 46, no. 12, pp. 4937–4943, 2013.
- [150] S. Iwamoto, W. Kai, A. Isogai, and T. Iwata, "Elastic modulus of single cellulose microfibrils from tunicate measured by atomic force microscopy," *Biomacromolecules*, vol. 10, pp. 2571–2576, 2009.
- [151] M. Henriksson and L. A. Berglund, "Structure and properties of cellulose nanocomposite films containing melamine formaldehyde," *J. Appl. Polym. Sci.*, vol.

- 106, no. 4, pp. 2817–2824, 2007.
- [152] S. Chen, G. Schueneman, R. B. Pipes, J. Youngblood, and R. J. Moon, “Effects of crystal orientation on cellulose nanocrystals-cellulose acetate nanocomposite fibers prepared by dry spinning,” *Biomacromolecules*, vol. 15, no. 10, pp. 3827–3835, 2014.
- [153] B. Wicklein *et al.*, “Thermally insulating and fire-retardant lightweight anisotropic foams based on nanocellulose and graphene oxide,” *Nat. Nanotechnol.*, vol. 10, no. 3, pp. 277–283, 2015.
- [154] S. Kalia *et al.*, “Cellulose-based bio- and nanocomposites: A review,” *International Journal of Polymer Science*, vol. 2011, 2011.
- [155] S. Shrestha, J. A. Diaz, S. Ghanbari, and J. P. Youngblood, “Hygroscopic Swelling Determination of Cellulose Nanocrystal (CNC) Films by Polarized Light Microscopy Digital Image Correlation,” *Biomacromolecules*, vol. 18, no. 5, pp. 1482–1490, 2017.
- [156] J. A. Diaz, X. Wu, A. Martini, J. P. Youngblood, and R. J. Moon, “Thermal expansion of self-organized and shear-oriented cellulose nanocrystal films,” *Biomacromolecules*, vol. 14, no. 8, pp. 2900–2908, 2013.
- [157] M. Nogi, S. Iwamoto, A. N. Nakagaito, and H. Yano, “Optically Transparent Nanofiber Paper,” *Adv. Mater.*, vol. 21, no. 16, pp. 1595–1598, 2009.
- [158] D. . Benford, T. . Powers, and S. . Moseley, “Thermal conductivity of Kapton tape,” *Cryogenics (Guildf.)*, vol. 39, no. 1, pp. 93–95, Jan. 1999.
- [159] J. P. F. Lagerwall *et al.*, “Cellulose nanocrystal-based materials: from liquid crystal self-assembly and glass formation to multifunctional thin films,” *NPG Asia Mater.*, vol. 6, no. 1, pp. e80–e80, Jan. 2014.
- [160] X. M. Dong, T. Kimura, J.-F. Revol, and D. G. Gray, “Effects of Ionic Strength on the Isotropic–Chiral Nematic Phase Transition of Suspensions of Cellulose Crystallites,” *Langmuir*, vol. 12, no. 8, pp. 2076–2082, Jan. 1996.
- [161] G.-H. Kim *et al.*, “High thermal conductivity in amorphous polymer blends by engineered interchain interactions,” *Nat. Mater.*, vol. 14, no. 3, pp. 295–300, Mar. 2015.
- [162] S. Y. Pak, H. M. Kim, S. Y. Kim, and J. R. Youn, “Synergistic improvement of thermal conductivity of thermoplastic composites with mixed boron nitride and multi-walled carbon nanotube fillers,” *Carbon N. Y.*, vol. 50, no. 13, pp. 4830–4838, Nov. 2012.
- [163] N. Burger, A. Laachachi, M. Ferriol, M. Lutz, V. Toniazzo, and D. Ruch, “Review of thermal conductivity in composites: Mechanisms, parameters and theory,”

Progress in Polymer Science, vol. 61. Pergamon, pp. 1–28, 01-Oct-2016.

- [164] Z. Han and A. Fina, “Thermal conductivity of carbon nanotubes and their polymer nanocomposites: A review,” *Prog. Polym. Sci.*, vol. 36, no. 7, pp. 914–944, Jul. 2011.
- [165] D. G. Cahill *et al.*, “Nanoscale thermal transport,” *J. Appl. Phys.*, vol. 93, no. 2, pp. 793–818, 2003.
- [166] C.-W. Nan and R. Birringer, “Determining the Kapitza resistance and the thermal conductivity of polycrystals: A simple model,” *Phys. Rev. B*, vol. 57, no. 14, pp. 8264–8268, Apr. 1998.
- [167] S. T. Huxtable *et al.*, “Interfacial heat flow in carbon nanotube suspensions,” *Nature Materials*, vol. 2, no. 11, pp. 731–734, 2003.
- [168] C. L. Choy, “Thermal conductivity of polymers,” *Polymer (Guildf.)*, vol. 18, no. 10, pp. 984–1004, Oct. 1977.
- [169] G. S. Cieloszyk, M. T. Cruz, and G. L. Salinger, “Thermal properties of dielectric solids below 4 K I—polycarbonate,” *Cryogenics (Guildf.)*, vol. 13, no. 12, pp. 718–721, Dec. 1973.
- [170] C. L. Choy and K. Young, “Thermal conductivity of semicrystalline polymers — a model,” *Polymer (Guildf.)*, vol. 18, no. 8, pp. 769–776, Aug. 1977.
- [171] C. . Choy, W. . Luk, and F. . Chen, “Thermal conductivity of highly oriented polyethylene,” *Polymer (Guildf.)*, vol. 19, no. 2, pp. 155–162, Feb. 1978.
- [172] C. L. Choy, F. C. Chen, and W. H. Luk, “Thermal conductivity of oriented crystalline polymers,” *J. Polym. Sci. Polym. Phys. Ed.*, vol. 18, no. 6, pp. 1187–1207, Jun. 1980.
- [173] R. J. Moon, A. Martini, J. Nairn, J. Simonsen, and J. Youngblood, *Cellulose nanomaterials review: structure, properties and nanocomposites*, vol. 40, no. 7. 2011.
- [174] K. E. Goodson and Y. S. Ju, “Heat Conduction in Novel Electronic Films,” *Annu. Rev. Mater. Sci.*, vol. 29, no. 1, pp. 261–293, 1999.
- [175] D. G. Cahill, K. Goodson, and A. Majumdar, “Thermometry and Thermal Transport in Micro/Nanoscale Solid-State Devices and Structures,” *J. Heat Transfer*, vol. 124, no. 2, p. 223, 2002.
- [176] P. Nath and K. L. Chopra, “Thermal conductivity of copper films,” *Thin Solid Films*, vol. 20, no. 1, pp. 53–62, 1974.
- [177] K. L. Chopra and P. Nath, “Thermal conductivity of ultrathin metal films in

- multilayer structures,” *J. Appl. Phys.*, vol. 45, no. 4, pp. 1923–1925, 1974.
- [178] C. E. Nebel, “Semiconductor materials: From gemstone to semiconductor,” *Nat. Mater.*, vol. 2, no. 7, pp. 431–432, 2003.
- [179] J. A. Carlisle, “Diamond films: Precious biosensors,” *Nature Materials*, vol. 3, no. 10, pp. 668–669, 2004.
- [180] J. Griffin and P. C. Ray, “Role of inert gas in the low-temperature nano-diamond chemical vapour deposition process,” *Nanotechnology*, vol. 17, no. 5, pp. 1225–1229, 2006.
- [181] A. A. Balandin, M. Shamsa, W. L. Liu, C. Casiraghi, and A. C. Ferrari, “Thermal conductivity of ultrathin tetrahedral amorphous carbon films,” *Appl. Phys. Lett.*, vol. 93, no. 4, 2008.
- [182] A. A. Balandin *et al.*, “Superior thermal conductivity of single-layer graphene,” *Nano Lett.*, vol. 8, no. 3, pp. 902–907, 2008.
- [183] S. Ghosh *et al.*, “Extremely high thermal conductivity of graphene: Prospects for thermal management applications in nanoelectronic circuits,” *Appl. Phys. Lett.*, vol. 92, no. 15, pp. 2008–2010, 2008.
- [184] S. Ghosh *et al.*, “Dimensional crossover of thermal transport in few-layer graphene,” *Nat. Mater.*, vol. 9, no. 7, pp. 555–558, 2010.
- [185] A. V. Sukhadolau, E. V. Ivakin, V. G. Ralchenko, A. V. Khomich, A. V. Vlasov, and A. F. Popovich, “Thermal conductivity of CVD diamond at elevated temperatures,” *Diam. Relat. Mater.*, vol. 14, no. 3–7, pp. 589–593, 2005.
- [186] J. E. Field, “The mechanical and strength properties of diamond,” *Reports on Progress in Physics*, vol. 75, no. 12, 2012.
- [187] L. Song *et al.*, “Large scale growth and characterization of atomic hexagonal boron nitride layers,” *Nano Lett.*, vol. 10, no. 8, pp. 3209–3215, 2010.
- [188] G. A. J. Amaratunga, “A dawn for carbon electronics?,” *Science*, vol. 297, no. 5587, pp. 1657–1658, 2002.
- [189] E. Kohn, A. Denisenko, M. Kubovic, T. Zimmermann, O. A. Williams, and D. M. Gruen, “A new diamond based heterostructure diode,” *Semicond. Sci. Technol.*, vol. 21, no. 4, 2006.
- [190] K. Yoshida, H. Morigami, “Thermal properties of diamond/copper composite material,” *Elsevier*, vol. 44, no. 2, pp. 303–308, 2004.
- [191] S. Bhattacharyya, “Mechanism of high n-type conduction in nitrogen-doped nanocrystalline diamond,” *Phys. Rev. B - Condens. Matter Mater. Phys.*, vol. 70, no.

12, 2004.

- [192] J. Isberg *et al.*, “High carrier mobility in single-crystal plasma-deposited diamond,” *Science* (80-.), vol. 297, no. 5587, pp. 1670–1672, 2002.
- [193] J. Asmussen and T. A. Grotjohn, *J. Asmussen, D. K. Reinhard (Eds.), Diamond Thin Films Handbook, Marcel Decker, NY., 2002.*
- [194] X. C. Tong, “Advanced Materials for Thermal Management of Electronic Packaging,” in *Advanced Materials for Thermal Management of Electronic Packaging*, vol. 30, 2011, pp. 1–58.
- [195] M. A. Angadi *et al.*, “Thermal transport and grain boundary conductance in ultrananocrystalline diamond thin films,” *J. Appl. Phys.*, vol. 99, no. 11, pp. 1–7, 2006.
- [196] M. Asheghi, M. N. Touzelbaev, K. E. Goodson, Y. K. Leung, and S. S. Wong, “Temperature-Dependent Thermal Conductivity of Single-Crystal Silicon Layers in SOI Substrates,” *J. Heat Transfer*, vol. 120, no. 1, p. 30, 1998.
- [197] S. Uma, A. D. McConnell, M. Asheghi, K. Kurabayashi, and K. E. Goodson, “Temperature-dependent thermal conductivity of undoped polycrystalline silicon layers,” *Int. J. Thermophys.*, vol. 22, no. 2, pp. 605–616, 2001.
- [198] H. J. Goldsmid, M. M. Kaila, and G. L. Paul, “Thermal conductivity of amorphous silicon,” *Phys. status solidi*, vol. 76, no. 1, pp. K31–K33, 1983.
- [199] M. A. Makeev and D. Srivastava, “Thermal properties of char obtained by pyrolysis: A molecular dynamics simulation study,” *Appl. Phys. Lett.*, vol. 95, no. 18, p. 181908, Nov. 2009.
- [200] M. Shamsa, W. L. Liu, A. A. Balandin, C. Casiraghi, W. I. Milne, and A. C. Ferrari, “Thermal conductivity of diamond-like carbon films,” *Appl. Phys. Lett.*, vol. 89, no. 16, p. 161921, Oct. 2006.
- [201] V. Goyal, S. Subrina, D. L. Nika, and A. A. Balandin, “Reduced thermal resistance of the silicon-synthetic diamond composite substrates at elevated temperatures,” *Appl. Phys. Lett.*, vol. 97, no. 3, p. 031904, Jul. 2010.
- [202] J. L. Tsai *et al.*, “Temperature-aware placement for SOCs,” *Proc. IEEE*, vol. 94, no. 8, pp. 1502–1517, 2006.
- [203] A. De Sio *et al.*, “Electro-optical response of a single-crystal diamond ultraviolet photoconductor in transverse configuration,” *Appl. Phys. Lett.*, vol. 86, no. 21, p. 213504, May 2005.
- [204] H. Masuda, K. Yasui, M. Watanabe, K. Nishio, T. N. Rao, and A. Fujishima, “Fabrication of Ordered Diamond/metal Nanocomposite Structures,” *Chem. Lett.*,

vol. 29, no. 10, pp. 1112–1113, Oct. 2000.

- [205] Y. Fu, H. Du, and J. Miao, “Patterning of diamond microstructures on Si substrate by bulk and surface micromachining,” *J. Mater. Process. Technol.*, vol. 132, no. 1–3, pp. 73–81, 2003.
- [206] S. Srinivasan, J. Hiller, B. Kabius, and O. Auciello, “Piezoelectric/ultrananocrystalline diamond heterostructures for high-performance multifunctional micro/nanoelectromechanical systems,” *Appl. Phys. Lett.*, vol. 90, no. 13, p. 134101, Mar. 2007.
- [207] F. Piazza, D. Grambole, D. Schneider, C. Casiraghi, A. C. Ferrari, and J. Robertson, “Protective diamond-like carbon coatings for future optical storage disks,” in *Diamond and Related Materials*, 2005, vol. 14, no. 3–7, pp. 994–999.
- [208] R. Abbaschian, H. Zhu, and C. Clarke, “High pressure-high temperature growth of diamond crystals using split sphere apparatus,” in *Diamond and Related Materials*, 2005, vol. 14, no. 11–12, pp. 1916–1919.
- [209] J. Laimer, H. Pauser, H. Stori, R. Haubner, and B. Lux, “Diamond growth in a direct-current low-pressure supersonic plasmajet,” *Diam. Relat. Mater.*, vol. 6, no. 2–4, pp. 406–410, 1997.
- [210] T. H. Kim *et al.*, “Printable, flexible, and stretchable forms of ultrananocrystalline diamond with applications in thermal management,” *Adv. Mater.*, vol. 20, no. 11, pp. 2171–2176, 2008.
- [211] D. G. Cahill and R. O. Pohl, “Thermal conductivity of amorphous solids above the plateau,” *Phys. Rev. B*, vol. 35, no. 8, pp. 4067–4073, 1987.
- [212] D. G. Cahill, “Thermal conductivity measurement from 30 to 750 K: The 3 omega method,” *Rev. Sci. Instrum.*, vol. 61, no. 2, pp. 802–808, 1990.
- [213] D. G. Cahill, M. Katiyar, and J. R. Abelson, “Thermal conductivity of a-Si:H thin films,” *Phys. Rev. B*, vol. 50, no. 9, pp. 6077–6081, 1994.
- [214] S. T. Huxtable, “Heat Transport in Superlattices and Nanowire Arrays,” *Ph. D. Thesis, Univ. California, Berkley*, pp. 1–165, 2002.
- [215] N. O. Birge and S. R. Nagel, “Wide-frequency specific heat spectrometer,” *Rev. Sci. Instrum.*, vol. 58, no. 8, pp. 1464–1470, 1987.
- [216] H. S. Carslaw and J. C. Jaeger, “Conduction of heat in solids.pdf,” *Oxford: Clarendon Press, 2nd. edit.* p. 100, 1959.
- [217] S.-M. Lee and D. G. Cahill, “Heat transport in thin dielectric films,” *J. Appl. Phys.*, vol. 81, no. 6, pp. 2590–2595, 1997.

- [218] A. Jaber, “Construction of a Thermal Conductivity Measurement Platform for Bulk and Thin Film Samples Based on the 3ω Technique,” *M.S. Thesis*, Arizona State Univ., pp. 1–63, 2014.
- [219] D. G. Cahill, “Thermal conductivity measurement from 30 to 750 K: the 3ω method,” *Rev. Sci. Instrum.*, vol. 61, no. 2, pp. 802–808, Feb. 1990.
- [220] S. T. Huxtable *et al.*, “Thermal conductivity of Si/SiGe and SiGe/SiGe superlattices,” *Appl. Phys. Lett.*, vol. 80, no. 10, pp. 1737–1739, Mar. 2002.
- [221] C. J. Glassbrenner and G. A. Slack, “Thermal Conductivity of Silicon and Germanium from 3°K to the Melting Point,” *Phys. Rev.*, vol. 134, no. 4A, pp. A1058–A1069, May 1964.
- [222] J. E. Graebner, M. E. Reiss, L. Seibles, T. M. Hartnett, R. P. Miller, and C. J. Robinson, “Phonon scattering in chemical-vapor-deposited diamond,” *Phys. Rev. B*, vol. 50, no. 6, pp. 3702–3713, Aug. 1994.
- [223] E. Wörner, C. Wild, W. Müller-Sebert, R. Locher, and P. Koidl, “Thermal conductivity of CVD diamond films: high-precision, temperature-resolved measurements,” *Diam. Relat. Mater.*, vol. 5, no. 6–8, pp. 688–692, May 1996.
- [224] L. Braginsky, N. Lukzen, V. Shklover, and H. Hofmann, “High-temperature phonon thermal conductivity of nanostructures,” *Phys. Rev. B*, vol. 66, no. 13, p. 134203, Oct. 2002.
- [225] M. A. Angadi *et al.*, “Thermal transport and grain boundary conductance in ultrananocrystalline diamond thin films,” *J. Appl. Phys.*, vol. 99, no. 11, p. 114301, Jun. 2006.
- [226] M. Shamsa, S. Ghosh, I. Calizo, V. Ralchenko, A. Popovich, and A. A. Balandin, “Thermal conductivity of nitrogenated ultrananocrystalline diamond films on silicon,” *J. Appl. Phys.*, vol. 103, no. 8, p. 083538, Apr. 2008.
- [227] V. Goyal, S. Subrina, D. L. Nika, and A. A. Balandin, “Reduced thermal resistance of the silicon-synthetic diamond composite substrates at elevated temperatures,” *Appl. Phys. Lett.*, vol. 97, no. 3, p. 031904, Jul. 2010.
- [228] B. L. Zink, R. Pietri, and F. Hellman, “Thermal conductivity and specific heat of thin-film amorphous silicon,” *Phys. Rev. Lett.*, vol. 96, no. 5, pp. 055902-1-055902-4, 2006.
- [229] A. Weathers and L. Shi, “Thermal Transport Measurement Techniques for Nanowires and Nanotubes,” *Annu. Rev. Heat Transf.*, vol. 16, pp. 101–134, 2013.
- [230] K. Schwab, E. Henriksen, J. Worlock, and M. Roukes, “Measurement of the quantum of thermal conductance,” *Nature*, vol. 404, pp. 974–977, 2000.

- [231] D. Li, Y. Wu, P. Kim, L. Shi, P. Yang, and A. Majumdar, "Thermal conductivity of individual silicon nanowires," *Appl. Phys. Lett.*, vol. 83, no. 14, pp. 2934–2936, Oct. 2003.
- [232] J. Zhou, C. Jin, J. H. Seol, X. Li, and L. Shi, "Thermoelectric properties of individual electrodeposited bismuth telluride nanowires," *Appl. Phys. Lett.*, vol. 87, no. 13, p. 133109, Sep. 2005.
- [233] C. Yu *et al.*, "Thermal Contact Resistance and Thermal Conductivity of a Carbon Nanofiber," *J. Heat Transfer*, vol. 128, no. 3, p. 234, Mar. 2006.
- [234] F. Zhou *et al.*, "Effect of growth base pressure on the thermoelectric properties of indium antimonide nanowires," *J. Phys. D: Appl. Phys.*, vol. 43, no. 2, p. 025406, Jan. 2010.
- [235] W. Cai *et al.*, "Thermal transport in suspended and supported monolayer graphene grown by chemical vapor deposition," *Nano Lett.*, vol. 10, no. 5, pp. 1645–1651, 2010.
- [236] A. Mavrokefalos, M. T. Pettes, F. Zhou, and L. Shi, "Four-probe measurements of the in-plane thermoelectric properties of nanofilms," *Rev. Sci. Instrum.*, vol. 78, no. 3, p. 034901, Mar. 2007.
- [237] F. Zhou, J. Szczech, M. T. Pettes, A. L. Moore, S. Jin, and L. Shi, "Determination of Transport Properties in Chromium Disilicide Nanowires via Combined Thermoelectric and Structural Characterizations," *Nano Lett.*, vol. 7, no. 6, pp. 1649–1654, Jun. 2007.
- [238] A. L. Moore, M. T. Pettes, F. Zhou, and L. Shi, "Thermal conductivity suppression in bismuth nanowires," *J. Appl. Phys.*, vol. 106, no. 3, p. 034310, Aug. 2009.
- [239] C. Faugeras, B. Faugeras, M. Orlita, M. Potemski, R. R. Nair, and A. K. Geim, "Thermal conductivity of graphene in corbino membrane geometry," *ACS Nano*, vol. 4, no. 4, pp. 1889–1892, 2010.
- [240] S. Chen *et al.*, "Raman Measurements of Thermal Transport in Suspended Monolayer Graphene of Variable Sizes in Vacuum and Gaseous Environments," *ACS Nano*, vol. 5, no. 1, pp. 321–328, Jan. 2011.
- [241] A. I. Boukai, Y. Bunimovich, J. Tahir-Kheli, J.-K. Yu, W. A. Goddard, and J. R. Heath, "Silicon nanowires as efficient thermoelectric materials," *Nature*, vol. 451, no. 7175, pp. 168–71, 2008.
- [242] J. H. Seol *et al.*, "Two-dimensional phonon transport in supported graphene," *Science*, vol. 328, no. 5975, pp. 213–6, Apr. 2010.
- [243] J.-H. Chen, C. Jang, S. Xiao, M. Ishigami, and M. S. Fuhrer, "Intrinsic and extrinsic performance limits of graphene devices on SiO₂," *Nat. Nanotechnol.*, vol. 3, no. 4,

pp. 206–209, Apr. 2008.

- [244] J. H. Seol, A. L. Moore, L. Shi, I. Jo, and Z. Yao, “Thermal Conductivity Measurement of Graphene Exfoliated on Silicon Dioxide,” *J. Heat Transfer*, vol. 133, no. February, p. 022403, 2011.
- [245] B. L. Zink and F. Hellman, “Specific heat and thermal conductivity of low-stress amorphous Si–N membranes,” *Solid State Commun.*, vol. 129, no. 3, pp. 199–204, Jan. 2004.
- [246] S. S. Verbridge, J. M. Parpia, R. B. Reichenbach, L. M. Bellan, and H. G. Craighead, “High quality factor resonance at room temperature with nanostrings under high tensile stress,” *J. Appl. Phys.*, vol. 99, no. 12, p. 124304, Jun. 2006.
- [247] A. Jain and K. E. Goodson, “Measurement of the Thermal Conductivity and Heat Capacity of Freestanding Shape Memory Thin Films Using the 3ω Method,” *J. Heat Transfer*, vol. 130, no. 10, p. 102402, Oct. 2008.
- [248] R. Sultan, A. D. Avery, G. Stiehl, and B. L. Zink, “Thermal conductivity of micromachined low-stress silicon-nitride beams from 77 to 325 K,” *J. Appl. Phys.*, vol. 105, no. 4, p. 043501, Feb. 2009.